Satellite Analysis of Radiation and Heat Fluxes during the Basel Urban Boundary Layer Experiment (BUBBLE)

Inauguraldissertation

zur Erlangung der Würde eines Doktors der Philosophie

vorgelegt der

Philosophischen-Naturwissenschaflichen Fakultät

der Universität Basel

von

Gergely Rigo

aus Basel/BS und Ungarn

Basel, 2006

Genehmigt von der Philosophisch-Naturwissenschaftlichen Fakultät auf Antrag von Prof. Dr. Eberhard Parlow, Basel und Prof. Dr. Wilfried Endlicher, Berlin

Basel, den 19. September 2006

Prof. Dr. Hans-Peter Hauri
Dekan

Contents

List of Figures

List of Tables

List of Symbols

Symbol	Description	Unit
a,b	Any variable	Var.
a	Absorption	%
c_p	Specific heat at constant pressure for moist air	J kg^{-1} K^{-1}
e	Vapour pressure	hPa
e_s	Saturated vapour pressure	hPa
Q_{SD}	Incoming short-wave radiation flux density	W m^{-2}
Q_{SU}	Outgoing short-wave radiation flux density	W m^{-2}
Q_S^*	Net short-wave radiation flux density	W m^{-2}
Q_{LD}	Incoming long-wave radiation flux density	W m^{-2}
Q_{LU}	Outgoing long-wave radiation flux density	W m^{-2}
Q_L^*	Net long-wave radiation flux density	W m^{-2}
L_υ	Latent heat of vaporization	J kg^{-1}
p	Air pressure	hPa
Q^*	Net all-wave radiation flux density	W m^{-2}
Q_E	Latent heat flux density	W m^{-2}
Q_F	Anthropogenic heat flux density	W m^{-2}
Q_H	Sensible heat flux density	W m^{-2}
r_H	Resistance to sensible heat transfer	
R	Correlation coefficient	
R^2	Coefficient of determination	
T_a	Air temperature	K
T_S	Acoustic temperature	K
T_s	Surface kinetic or radiant temperature	K
t	Time	s
u	Wind speed	m s^{-1}
z	Height above ground level	m
z_H	Mean building height	m

Symbol	Description	Unit
α	Shortwave (broadband) albedo	%
β	Bowen-Ratio	
ΔQ_S	Storage or ground heat flux density of a surface	W m^{-2}
ε	Long-wave (broadband) emissivity	%
λ	Wavelength	m
λ_C	Complete aspect ratio	m^2 m^{-2}
σ_B	Stefan-Boltzmann constant	W m^{-2} K^{-4}
Ψ_S	Sky-view factor	
ν	Frequency	Hz
θ	Virtual acoustic temperature	K
θ_T	Potential thermodynamic temperature	K
ρ_υ	Absolute humidity (density of water vapour)	Kg m^{-3}
ω	Vertical wind direction	°
ρ	Air density	Kg m^{-3}
ρ_c	Density of CO_2	Kg m^{-3}
γ^*	Psychrometric constant	Pa K^{-1}
$\overline{\omega' T_S'}$	Covariance of acoustic temperature and vertical wind	
$\overline{\omega' \rho_v'}$	Covariance of absolute humidity and vertical wind	

a	Scalar
a	Vector
$\bar{a}$	Temporal average
a´	Turbulent departure deviation from temporal average

List of Abbreviations

ASTER	Advanced Spaceborne Thermal Emission and Reflection Radiometer
ATBD	ASTER Algorithm Technical Basis Documents
AVHRR	Advanced Very High Resolution Radiometer
BUBBLE	Basel UrBan Boundary Layer Experiment
BRDF	Bidirectional Reflectance Distribution Function
CASPR	Cloud and Surface Parameter Retrieval
CAR	Complete Aspect Ratio
CET	Central European Time (UTC + 1h)
DEM	Digital Elevation Model
DCEM	Digital City Elevation Model
DN	Digital Number
DOY	Day of the Year
ETM+	Enhanced Thematic Mapper Plus
EVI	Enhanced Vegetation Index
FOV	Field of View
HRPT	High Resolution Picture Transmission
IFOV	Instantaneous Field of View
IOP	Intensive Operational Phase
IR	Infrared
IRT	Infrared Thermometer
LAI	Leaf Area Index
LST	Land Surface Temperature
LUC	Land Use Classification
LUMPS	Local-Scale Urban Meteorological Parametrization Scheme
LUT	Look-Up Table
MAD	Mean Absolute Difference
MAPD	Mean Absolute Percentage Difference
MISR	Multi-angle Imaging Spectroradiometer
MODIS	Moderate Resolution Imaging Spectrometer
MODTRAN	Moderate Resolution Transmittance Code
NASA	National Aeronautics and Space Administration
NEM	Normal Emissivity Method
NDVI	Normalized Difference Vegetation Index
NOAA	National Oceanic and Atmospheric Administration
OHM	Objective Hysteresis Model
POES	Polar Orbiting Environmental Satellite

RMSE	Root Mean Square Error
RTC	Radiative Transfer Code
SARAH	Satellite Analysis of Radiation And Heat fluxes
SAVI	Soil Adjusted Vegetation Index
SEBAL	Surface Energy Balance Algorithm for Land
SLC	Scan Line Corrector
SLK	Schweizerische Landes-Koordinaten (Swiss National Geographic Grid)
SMAC	Simplified Method for Atmospheric Correction
SUHI	Surface Urban Heat Island
SWIM	Short Wave Irradiance Model
SWT	Split Window Technique
TEB	Town Energy Balance
TES	Temperature-Emissivity Separation
TIR	Thermal Infrared
TOA	Top Of Atmosphere
TSTIM	Two Source Time Integrated Model
UHI	Urban Heat Island
UTC	Universal Time Coordinate
UTM	Universal Transverse Mercator
VI	Vegetation Index
WGS- 84	World Geodetic System 1984

Acknowledgements

First I would like to thank Prof. Dr. Eberhard Parlow who gave me the opportunity to write this Ph.D. thesis at the Institute of Meteorology, Climatology and Remote Sensing in a field in which I am tremendously interested. He also acted as my supervisor over the final four years and always had an open door for questions, discussions or ideas even when his schedule was very tight.

I would also like to thank Dr. Andreas Christen, Dr. Dave Oesch and Dipl.-Geogr. Corinne Frey for their fruitful participation in discussions on different aspects of the thesis, and for their invaluable creative input over the past years.

As for the computer hard- and software, Dipl.-Phys. Günter Bing was the person to ensure that everything went (and still goes…) well with no data loss, providing support covering every type of problem imaginable when working with digital data.

In such a small but fine institute, the working atmosphere was also always friendly, which I appreciated very much. For the moral support therefore many thanks to Dr. Mathias "Schreihals" Müller who shared a room with me for 3 years and tried – with some success – to infect me with the "mad scientist disease". Dipl.-Geogr. Irene "Frau L." Lehner was also always there to give advice when complications arose in my research. Dr. Roland Vogt answered questions about *in situ* instrumentation when they arose and our secretary Josette Pfefferly-Stocky provided excellent administrative support all the times.

The BUBBLE-project would not have been possible without the many contributions made by different institutes around the world in terms of manpower and *in situ* instrumentation. Many thanks are due to all of them.

Financial funding of this thesis was provided by the Swiss National Foundation (grants No. 2100-067964 and No. 200020-105299/1). Radisonde data were supplied by MeteoSwiss.

Last but not least, many thanks go to my parents and my brother, who always encouraged and supported me over this time to go my own way.

Zusammenfassung

Städtische Gebiete unterscheiden sich stark von ruralen Gebieten und modifizieren die Strahlungs- und Energiebilanz, weshalb Stadtklimatologie zu einer der wichtigsten Forschungsgebiete der Klimatologie gehört. Da jedoch urbane Gebiete im Vergleich zu den mehrheitlich homogenen ruralen Gebieten sehr heterogen sind, sind Untersuchungen mit Fernerkundungsdaten in Ermangelung vorhandener *in situ* Daten zur Validierung bis dato nicht im grossen Masse durchgeführt worden. Aus diesem Grunde wurden neben den sehr umfangreichen *in situ* Daten des Basel Urban Boundary Layer Experiment (BUBBLE) Fernerkundungsdaten von verschiedenen Satellitenplatformen (AVHRR, MODIS, ASTER, LANDSAT ETM+ und Quickbird) prozessiert, analysiert und mit *in situ* Daten validiert. Das BUBBLE Experiment war ein gemeinsames europäisches COST Projekt (Coopération Européenne dans la domaine de la recherche Scientifique et Technique, COST 715: Meteorology applied to urban pollution problems).

Zuerst wurden die Thermaldaten von AVHRR, MODIS, LANDSAT ETM+ und ASTER validiert inklusive einer Vergleichstudie von sechs Split-Window-Algorithmen für den AVHRR, wobei insgesamt eine hohe Genauigkeit von ± 5% zwischen Satellitendaten und *in situ* Daten festgestellt werden konnte.

Anschliessend wurde die Strahlungsbilanz (Q*) modelliert, wobei die kurzwellige Einstrahlung mit dem Short Wave Irradiance Model (SWIM) modelliert wurde und die Albedo aus den sichtbaren und nahen infraroten Spektralkanälen der jeweiligen Satelliten berechnet wurde. Die mittlere absolute Abweichung (MAD) zwischen gemessenen und modelliertem Q* betrug 26 Wm^{-2} ohne merkbare Unterschiede zwischen ruralen oder urbanen Flächen. Die räumliche Verteilung der Daten zeigt eine niedrigere Strahlungsbilanz über den urbanen Flächen im Vergleich zu den ruralen wie dies auch bei den *in situ* Daten der Fall ist. Für eine experimentelle höchstaufgelöste Modellierung wurden zusätzlich Daten von Quickbird zusammen mit einem Helikopterüberflug mit einer InfraTec Thermalkamera verwendet.

Nach der erfolgreichen Modellierung von Q* wurde der Speicher- oder Bodenwärmestrom ΔQ_S mit drei unterschiedlichen Ansätzen modelliert und mit den *in situ* Daten verglichen: a) Der Complete Aspect Ratio (CAR) Ansatz, b) der Normalized Difference Vegetation Index (NDVI) Ansatz und c) der Objective Hysteresis Model (OHM) Ansatz. Die MAD betrug hierbei 17 Wm^{-2} und die Standardabweichung ebenfalls 17 Wm^{-2}, wobei der OHM Ansatz am besten abschnitt.

Zuletzt wurden die turbulenten Wärmeflüsse Q_E und Q_H modelliert und zwar mit einem Bowen-Ratio/ NDVI Ansatz. Die MAD betrug 28 Wm^{-2} für Q_E bzw. 18 Wm^{-2} für Q_H.

Aufgrund der guten Ergebnisse aus den BUBBLE-Daten und um die Übertragbarkeit der Modelle auf andere Zeitpunkte zu testen, wurden mit einem zusätzlichen Datensatz von Satellitendaten aus dem Sommer 2003 dieselben Modellierungen und Validierungen durchgeführt. Die Resultate zeigen eine ähnliche Genauigkeit, was die Resultate aus 2002 stützte und die Anwendbarkeit des Modells für unterschiedliche Zeitpunkte bestätigte.

Mit dem in dieser Arbeit aufgezeigten Modell kann somit die Energie- und Strahlungsbilanz im räumlichen Kontext über ruralen und urbanen Flächen sehr gut dargestellt und mit hoher Genauigkeit modelliert werden. Dies ist für die weitere Erforschung des Stadtklimas und auch für Stadtplaner von grosser Wichtigkeit.

Abstract

Because urban areas show a different climate when compared to their surroundings and alter local radiation and energy balances they are an important topic in climatology. Urban areas are also highly heterogeneous areas when compared to rural ones, little research with satellite data has been conducted until now. It is the goal of this thesis to model and illustrate, with the use of remotely sensed data, urban alterations of the radiation and energy flux densities in the spatial domain. Besides very detailed field measurements of the structure and dynamics of the urban boundary layer with a large *in situ* data network from the Basel Urban Boundary Layer Experiment (BUBBLE), remote sensing data were analyzed and validated from several satellites. The BUBBLE experiment was a joint European research project under the umbrella of COST (Coopération Européenne dans la domaine de la recherche Scientifique et Technique, COST 715: Meteorology applied to urban pollution problems).

For this purpose data from AVHRR, MODIS, ASTER, LANDSAT ETM+ and Quickbird were acquired and processed. After each step of the modelling the results from the remotely sensed data were compared and validated with the *in situ* data.

The first step was the validation of the thermal infrared (TIR) satellite data and an accuracy assessment of six different Split-Window algorithms for the AVHRR. The results for the different sensors showed an average accuracy of less than ±5 % even in urban environments for the different sensors.

Afterwards the net all-wave radiation (Q*) was modelled with shortwave inputs derived from the Short Wave Irradiance Model (SWIM). The modelled broadband albedo was also derived from satellite data. The results of Q* showed a good mean absolute difference (MAD) of 26 Wm^{-2} over rural and urban surfaces. The spatial distribution of Q* also agreed fully with the *in situ* results showing a lower Q* for the urban areas than for the countryside. For a very high resolution modelling of Q* in the city an experimental approach with thermal imagery from a helicopter overflight together with data from Quickbird was used and showed the extent to which Q* in a city is influenced by the albedo of the vegetation.

From the available Q* the storage (or ground) heat flux ΔQ_S was modelled using three different models: the complete aspect ratio model (CAR), the Normalized Difference Vegetation Index (NDVI) and the Objective Hysteresis Model (OHM). The most useful results were achieved with the OHM, which was applied and validated with satellite data over an urban surface for the first time. The MAD was 17 Wm^{-2} with an RMSE of also of 17 Wm^{-2}.

After the successful modelling of the ground heat flux density, the latent Q_E and sensible Q_H heat flux densities were modelled with a combined Bowen-Ratio /NDVI approach resulting in a MAD of 28 Wm^{-2} and 18 Wm^{-2} respectively.

All the results of this thesis provided quite accurate representations of the distribution of the radiation and heat flux densities, as well as of the differences between rural and urban surfaces; therefore, the model was applied and validated using datasets acquired from 2003 for the same research area, showing similar results as for the BUBBLE campaign. This shows the possible transferability of the model to other times and dates.

With the model described in this thesis the radiation and energy flux densities can be modelled accurately in the spatial domain over urban (and rural) surfaces and used both for further urban climatology studies and for urban planning.

1. Introduction

As more than 50% of Earth's population live in urbanized areas and in countries with high average temperatures, billions suffer from the climatic impacts of urbanization – a fact acknowledged by many recent publications (see Arnfield, 2003 for an overview). Most urban meteorological measurements and models are based on *in situ* instrumentations or are drive-through measurements in different cities of the world.

Another field of urban climatology research has the primary goal of understanding and fighting climatic stress factors acting on urban populations who suffer increasingly from problems including air pollution and thermal stress due to the modifications, as described in Oke (1990), of the radiation and energy balance by urban areas.

Therefore urban climatology has become an increasingly important topic in the last decades; the often used Urban Heat Island (UHI) is the best known example of climate modification in urban environments (Kim, 1992, Oke, 1982).

The most important aspect of urban climatology that cannot be fully described using *in situ* measurements, however, is the spatial domain. Punctual measurements in an environment as heterogeneous as a city cannot show the spatial distribution of actual data; and drive-trough measurements can give only a rough overview. Remote sensing is one of the most useful and practical methods to fill this gap.

Previous applications of remote sensing data for urban climatology research have focussed mostly on the UHI –or, more accurately, SUHI (Surface Urban Heat Island) (Dusset & Gourmelon, 2003; Gallo et al., 1993; Munier & Burger, 2001; Nichol, 1998; Nichol & Wong, 2005) - in various climatic and geographic regions, but none have looked further into the radiation or energy balance. However advantageous remote sensing may be for this purposes, it is impossible to model and calculate radiation and heat flux densities with satellite remote sensing data without some *in situ* measurements for validation purposes.

Objective of this thesis

For urban climatology the radiation and heat fluxes are extremely important and are significantly different from their rural counterparts (Oke, 1990). For assessment of these parameters, it is crucial to try to model them in their specific spatial domains, rather than making estimates based on rural areas.

This leads to the questions which I hope to answer with this thesis and upon which my research concept is based:

- Is it possible to model the radiation and heat fluxes in an urban environment with the use of different types of remotely sensed data?
- What degree of accuracy is possible?
- What kind of *in situ* data is needed?
- Do different methods exist to assess the storage (or ground) heat flux density in an urban area, which is very difficult to measure even with *in situ* instrumentation?

As mentioned above, without available *in situ* data for validation, accuracy assessment, and input, reliable answers to these questions are virtually unattainable. Therefore this work took the advantage of the availability of data from the uniquely extensive *in situ* network of the Basel Urban Boundary Layer Experiment (BUBBLE) Intensive Operational Phase (IOP) and its nesting as "BUBBLE-SARAH" (**S**atellite **A**nalysis of **R**adiation **a**nd **H**eat Fluxes). With such a wealth of data available for

each step, modelled remotely sensed data were compared and validated with the *in situ* measurement to ensure that they were accurate enough for further processing. Therefore, the error margins were minimized throughout the process, from the longwave upward radiation on up to the modelling of the turbulent heat fluxes in the spatial domain.

After the first accuracy assessment during BUBBLE, a new question arose: can this model be also be used on data from other years, without the extensive BUBBLE network in place? To test this possibility, the model was also applied to data from 2003.

Because very high-resolution data have become available in recent years from satellites such as Quickbird and Ikonos another question was whether and how such data could also be used for the modelling of the radiation and energy balance.

The remotely sensed datasets for this thesis were recorded via numerous overpasses by

- the Advanced Very High Resolution Radiometers (AVHRR) from the National Oceanic and Atmospheric Administration (NOAA),
- the Moderate Resolution Imaging Spectrometer (MODIS)
- the LANDSAT ETM+ (Enhanced Thematic Mapper Plus)
- the Advanced Spaceborne Thermal Emission and Reflection Radiometer (ASTER)

Whereas the work of Christen (2005) addresses atmospheric turbulence in the urban roughness sublayer as well as its impact on diffusion and momentum, mass and energy exchange, this thesis's observations are made from a remote sensing point of view to model the radiation and heat flux densities in and around the City of Basel in the spatial domain.

Parts of this work were published in Rigo et al. (2006) and are submitted in Rigo & Parlow.

2. Research area

The research area is located in and around the City of Basel in north-western Switzerland. Basel was chosen because it is the location of the Basel Urban Boundary Layer Experiment (BUBBLE) project, and because it represents a typical medium-sized mid-European city. With a population of approximately 200'000 inhabitants, Basel itself is moderately flat, and has an average altitude of 260 m a.s.l.. Situated at the bend of the River Rhine (see Figure 2.1), which marks the beginning of the Upper Rhine Valley, it borders on France and Germany and is mainly surrounded by agricultural fields and forest area. To the northeast, the mountains of the Black Forest dominate the topography; to the south the mountains of the Swiss Jura limit the areas suitable for habitation.

Basel's inner core, on the south bank of the River Rhine, is a medieval city centre; whereas the surrounding neighbourhoods consist mainly of typical 5 to 6 storey mid-European residential blocks. Farther from the center, between the city and the countryside are predominantly two-storey houses with gardens. In the southern part of the city (above and to the right of the "Switzerland" label on the map below), and in the northwest, near the airport, industrial (mostly chemical) complexes have a strong presence.

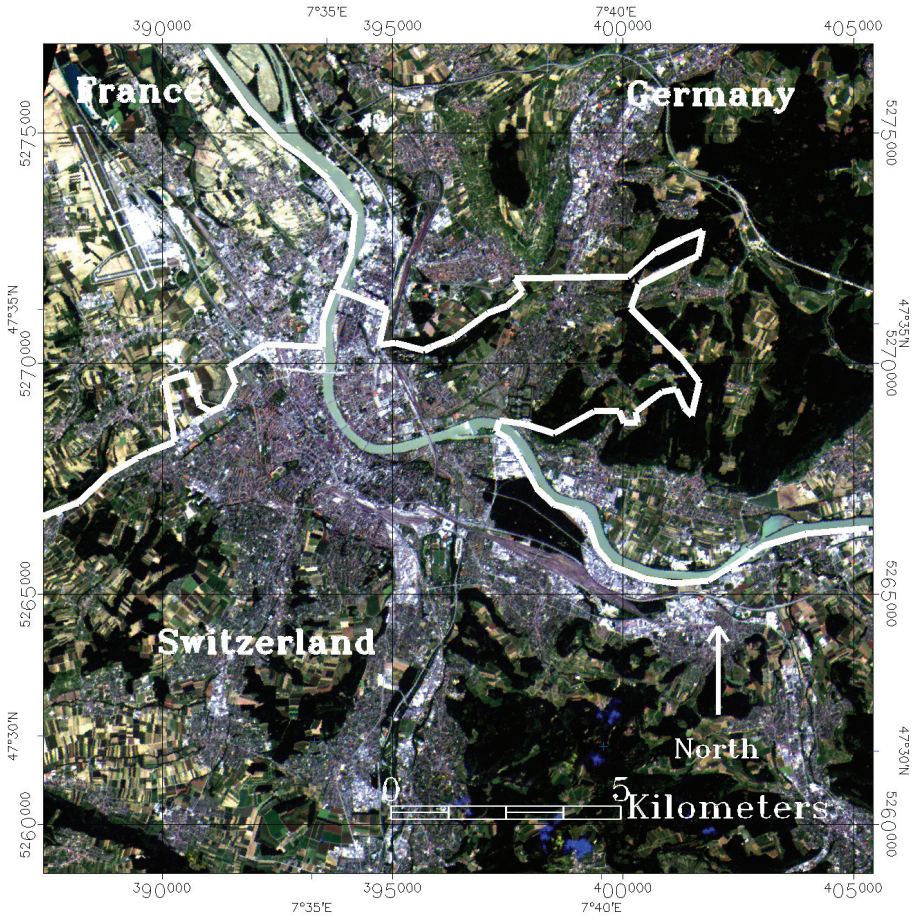

Fig. 2.1: LANDSAT ETM+-ASTER fused imagery from the 12.06.2001 of the City of Basel and surroundings (UTM Zone 32 North, WGS-84)

To aid in visualization of images showing results, coordinates and grids will generally be omitted. Due to the location and course of the River Rhine the geographic locations of all the figures can be recognized easily. Nevertheless, North directional arrows and scale bars will always be provided.

2.1 In situ sites

The experimental phase of BUBBLE started in summer 2001 and ended in summer 2002. Between June 10 and July 10, 2002, an intensive observation period (IOP) was carried out, which embedded many activities from international research groups. The overall framework and the experimental activities of BUBBLE are documented in Rotach et al. (2005).

The map in Figure 2.2 shows the topography and setting of all the BUBBLE experimental activities in the City of Basel. Site labels are coded according to surface characteristics (U: urban, S: suburban, R: rural). More specific descriptions can be found in Table 2.1 and in the Appendix A.

The nomenclature in Figure 2.2 is slightly different from that used in this work (e.g. "Ue1" denotes **u**rban **e**nergy balance site one). In this work only the energy balance sites are used, so the sites are named based on their locations alone (e.g. U1 = urban site one).

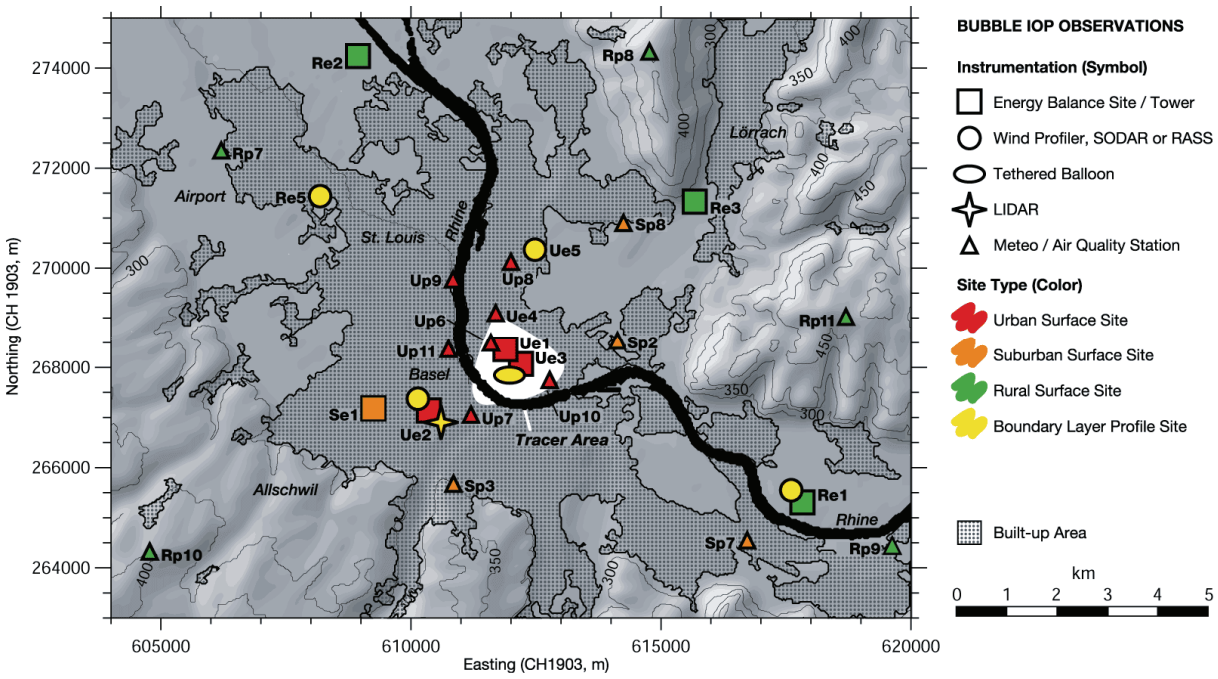

Fig. 2.2: Map of the BUBBLE area showing the locations of the measurement sites. The built-up area is shaded in grey and the coordinates match those of SLK, the Swiss national cartographic grid (official BUBBLE site location image).

The BUBBLE data set involves 30 experimental or permanent sites from the greater Basel area of which eight were equipped for complete coverage and measurement of radiation and heat flux densities.

Three experimental sites (Sperrstrasse (U1), Spalenring (U2) and Allschwil (S1)) were set up with towers supporting the profiles of ultrasonic anemometers, cup anemometers and temperature / humidity sensors, as well as radiation balance measurements well above the urban surface. The vertical profiles address the domain from street level up to approximately two times the mean building height z_h.

During the IOP, the three profile tower sites were extended by a network of four additional experimental sites (Messe (U3), Grenzach (R1), Lange Erlen (R2) and Village-Neuf (R3)) which resulted in eight radiation balance sites. Three of these were equipped with instruments at one level (U3, R1 and R2). These sites were installed in different land use areas, mainly in the rural region surrounding the city (Figure 2.2 and Table 2.1). Together with the profile towers, this network provided the basis for a detailed investigation of the urban modification of mean and turbulent properties, especially turbulent flux densities, under the same synoptic forcing. For this purpose seven of the eight radiation balance sites were equipped with the necessary instrumentation to work as surface energy balance sites (the site R4 was not equipped).

The extended analysis of the atmospheric turbulence and surface energy exchange from the micrometeorological data can be found in Christen (2005) and is not covered by this work, although this work is also based on the BUBBLE *in situ* measurement network for validation and calibration of the remotely sensed datasets.

In the present work, the three profile towers (U1, U2 and S1) and the additional energy balance sites (U3, R1, R2, and R3) are of primary interest. These sites are documented in Appendix A and a short summary of the sites' characteristics can also be found in Table 2.1.

For 2003 and until the BUBBLE-IOP all the data were acquired from the regular long-term measurement sites of the Institute of Meteorology, Climatology and Remote Sensing. This regular pre-BUBBLE network consisted of the sites R2, U2 and R4. After the BUBBLE-IOP the tower from U2 was moved to the Institute's new location at the Klingelbergstrasse site (see also Appendix A for more information about the sites).

A detailed description of *in situ* radiation and energy balance measurement instruments operated during BUBBLE, the field intercomparisons and calibrations and the resulting effects can be found in a technical report by Christen & Vogt (2005) and also in Christen & Vogt (2004). The most important facts for this work are denoted in the following subchapters. As long as not mentioned otherwise, all the *in situ* measurements used for validation and calibration were taken from each sites' highest point.

Tab. 2.1: Surface characteristics of the *in situ* measurement sites

Site	Sperrstrasse (U1)	Spalenring (U2)	Messe (U3)	Allschwil (S1)	Grenzach (R1)	Village-Neuf (R2)	Lange Erlen (R3)	Gempen (R4)
Land use	*Urban* Tower in and above street canyon, with mainly residential 3-4 storey buildings	*Urban* Tower above vegetated canyon with 3-5 storey buildings	*Urban* System over a parking lot on top of a large 26m -high building.	*Suburban* Tower in vegetated, backyard, residential single and row houses, 2-3 storey	*Rural* Tower over grassland	*Rural* System over agricultural land	*Rural* Profile tower and radiation measurements over grassland	*Rural* Tower over mixed rural land (half agricultural land and half grassland)
Height a.s.l.	255m	278m	255m	277m	265m	240m	275m	710m
UTM (Zone 32N, WGS-84)	394516 E 5269159 N	392962 E 5267966 N	394820 E 5268858 N	391854 E 5268028 N	400389 E 5265807 N	391684 E 5275087 N	398519 E 5272024 N	400056 E 5258649 N
Sky view factor	0.36	0.51	0.57	0.61	1	1	1	1
Average Building height z_H	14.6 m	12.5 m	18.8 m	7.5m	*Rural* System over agricultural land			
Level of sonics with z / z_H	2.17	2.39		2.11				
Roof Materials	45% tiles, 50% gravel, 5% corrugated iron	70% tiles, 30% gravel	100% concrete	95% tiles, 5% gravel				
Building Materials	Plaster, concrete, brick	Plaster, concrete	Concrete	Plaster, brick				

3. Theory

3.1 Remote Sensing

3.1.1 Short introduction to remote sensing

Remote sensing is the measurement of electromagnetic energy reflected from or emitted by a target from a vantage point that is distant from the target (Mather 1999).

This definition is in some ways too broad, as it would also include microscopy, geophysics and astronomy. Therefore it is better defined, for the purpose of this thesis, as "the information, taken by airborne or spaceborne sensors, recording details, pertaining to the surface of landmasses or oceans and the atmosphere above them" (Legg 1995). The sensors record the amounts of energy reflected or emitted by the Earth's surface. Earth observation includes not only the interpretation of the measurements, but also the establishment of the relationships between these measurements, the nature and distribution of phenomena at the Earth's surface or within the atmosphere.

Basically two different remote sensing systems exist. The broadly used passive systems are pure reception systems; recording only the naturally available radiation, which can be emitted, reflected or scattered on the surface of the Earth or in the atmosphere. Examples include the LANDSAT-platform, the AVHRR, the MODIS and also ASTER. Active systems send signals by themselves and subsequently receive the reflected signal, along with atmospheric influences. While passive systems mostly monitor reflected radiation in the UV, visible and infrared spectral ranges, the active systems produce waves in the microwave band (Richards & Jia, 1999).

3.1.2 Basic physical principles

Passive satellite sensors can measure electromagnetic radiation or radiant energy. While energy is defined as the capacity to do work and is expressed in Joules [J], the flux of energy is the rate of transfer of energy from one place to another and is measured in Watts [W]. The density of flux energy is dependent of the angle between the incoming radiation and the incident surface. Here the term of "radiant flux density" will be used to denote the magnitude of the radiant flux that is incident upon, or, is emitted by a surface unit area, expressed as Wm^{-2}. All radiant energy that comes from a single steradian on the Earth's surface can be addressed as radiance (Mather 1999).

Transported energy is dependent not only on the intensity of the waves but also on the wavelength. Electromagnetic radiation can be partitioned –based on wavelength- according to the divisions of an electromagnetic spectrum. This spectrum ranges from X-rays (the shortest waves of this spectrum) through visible light up to radio waves. In remote sensing, only a segment of this spectrum is used. This segment ranges from 0.3μm in the ultraviolet region up to about one metre for the microwave remote sensing (Legg 1995).

All matter whose temperature is above absolute zero (-273.15°C or 0 K) emits electromagnetic radiation. Therefore electromagnetic radiation originates from both the sun and from the Earth. The amount of emitted radiation depends on the temperature of the emitting body. The higher the temperature, the shorter the wavelength of maximum emission becomes and the greater is the amount of energy radiated. Planck's Law (eq. 3.1) describes the behaviour of a blackbody radiator –a hypothetical body that completely absorbs all wavelengths of thermal radiation incident on it– as follows.

$$B_\lambda(T_s) = \frac{c_1 \lambda^{-5}}{\pi\left(e^{c_2/\lambda T_s} - 1\right)} \qquad (3.1)$$

Where $c_1 = 3.74 * 10^{-16}$ Wm^2 and $c_2 = 1.45 * 10^{-2}$ m K.

The Stefan-Boltzmann Law (eq. 3.2) describes the total intensity of radiation emitted by the surface of a body at all wavelengths. Mathematically, this is the integration of Planck's Law where σ_B is the Stephan-Boltzmann constant.

$$E = \varepsilon \cdot \sigma_B \cdot T^4 \quad [Wm^{-2}] \qquad (3.2)$$

As previously mentioned, the wavelength of peak emission shortens when the temperature of a blackbody increases. This is the direct result of Wien's Law, which states, that, as the temperature of a body increases, more radiation in the shorter wavelengths will be emitted.

$$\lambda_{max} \cdot T_s = const. = 2898 \text{ [µm K]} \qquad (3.3)$$

With a temperature of 6000 K the sun emits radiation with an average wavelength of 0.47µm (λ_{max}= 0.47µm). The Earth (T_s = 290 K) is emitting at λ_{max}= 9.7µm (see Figure 3.1) Short-wave radiation is therefore (mostly) the sun's emitted radiation. The solar radiation has wavelengths between 0.003 and 3 µm. Long-wave or thermal infrared (TIR) radiation is terrestrial radiation, greater than 3 µm and is emitted by the Earth's surface.

$$\varepsilon(\lambda, T_s) = a(\lambda, T_s) \qquad (3.4)$$

The coefficients ε (emissivity) and *a* (absorption) range between 0 and 1. Regarding emissivity, ε < 1 denotes a grey body, and ε = 1 denotes a blackbody radiator. For the albedo, α=0 and α=1 denote, respectively, a very poor reflector and a perfect reflector. Normally there is no blackbody radiator in nature, therefore every surface on earth has an emissivity below 1 and is therefore effectively a grey body.

Kirchhoff's Law states, that at thermal equilibrium, the radiation emitted at any point on a thermal radiator and for any wavelength must be equal to the radiation absorbed.

According to Newton's principle of conservation of energy and Kirchhoff's law for any material the equation

$$\varepsilon(\lambda, T_s) + a(\lambda, T_s) + \tau(\lambda, T_s) = 1 \qquad (3.5)$$

is valid. Assuming the transmittance τ of surfaces to be zero,

$$\varepsilon(\lambda,T_s) + a(\lambda,T_s) = 1. \qquad (3.6)$$

As most of the radiation emitted by the sun is in the visible range, the high percentage of absorption in the infrared bands is irrelevant to the energy budget of the Earth's surface.

According to equations (3.4) and (3.5) assuming that the transmittance of surface materials is zero, in areas where the albedo is low, the absorption of the wavelengths must be high and vice versa.

As Figure 3.1 illustrates, Earth's atmosphere is in effect more or less translucent regarding radiation. The spectral recording channels of the satellites are usually in the respective atmospheric windows where transmittance through the atmosphere is high.

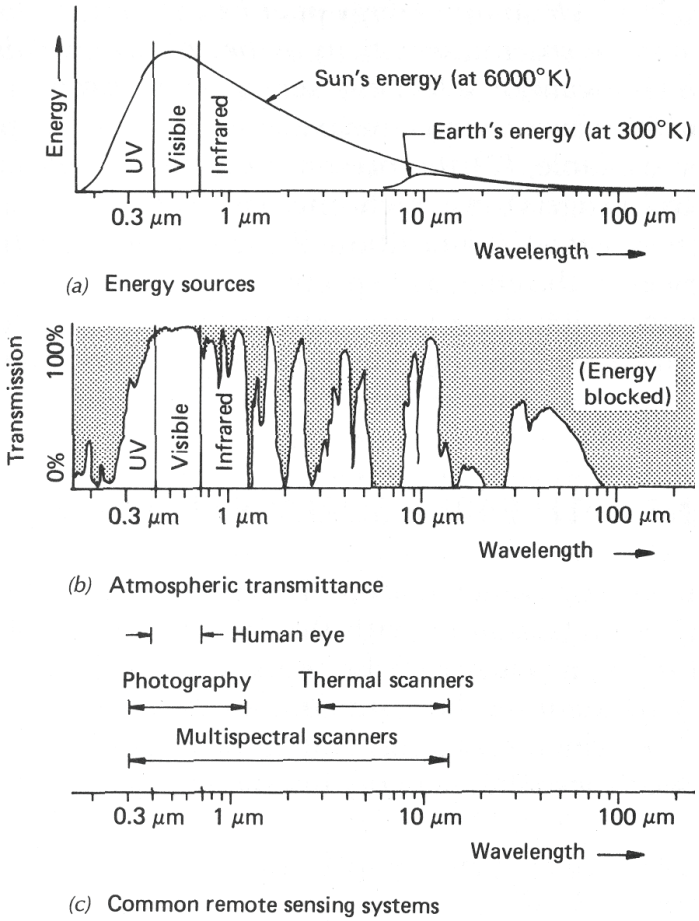

Fig. 3.1: a) Emission spectra of the sun and the Earth and their respective maximums according to Wien's Law; b) Atmospheric transmittance - wavelengths at which electro-magnetic radiation will penetrate the Earth's atmosphere; c) Wavelength of the sensing systems (note: wavelength scale is logarithmic) (after Lillesand & Kiefer, 1994).

All radiation that passes through the atmosphere is either diffused absorbed, reflected or scattered therein due to atmospheric gases (CO_2, H_2O, O_3 etc.). Since atmospheric conditions make 100% transmittance impossible, measurements at the top of the atmosphere (TOA) (i.e. the raw satellite data) need to be corrected for atmospheric influence. This makes an atmospheric correction for especially all thermal datasets necessary. As described in chapter 5.1, corrections were accomplished for the different satellite datasets by various methods.

3.2 Limitations of remotely sensed data

3.2.1 Viewing angle

The instantaneous field of view (IFOV) is constant for all the satellites used in this study. As a result the effective pixel size on the ground is larger at the extremities of the image than at the nadir. For small off-nadir viewing angles, this effect is negligible. For example for the LANDSAT ETM+ the image's border pixels are only 1.02 instead of 1.00 at the nadir (Richards & Xia, 1999). The same is true for ASTER. On the other hand, for AVHRR and MODIS this effect can be quite severe resulting in an effective pixel area of more than 70% greater than at the nadir. This effect also limited the useful AVHRR data for this project, because some images where the research area was at the border of the image were completely useless for further processing and validation. For the MODIS data the research area was very close to the nadir; therefore this error was not implicated into the datasets.

3.2.2 Pixel resolution and mixed pixel problem

When satellite data is interpreted, several types of resolution are discussed. Spectral resolution, temporal resolution and radiometric resolution refer respectively to the number of available bands, the time between the satellite overpasses and the number of bits available for the data. Another aspect is the spatial resolution of the sensor, which relates to the area covered by each pixel. In this work, the spatial resolution of the different satellite sensors ranges from 0.62 m, from the panchromatic Quickbird, up to 1.1 km, from the AVHRR's thermal IR system. With different pixel resolutions what each pixel actually "sees" is also different. There is no such thing as a "pure" pixel; every pixel is influenced by its neighbours, so the resulting record is always mixed, with the majority of the recorded radiation coming from each pixel's target area, but also some part is therefore coming from those of the surrounding pixels (Mather, 1999 and Richards & Xia, 1999).

This was one of the reasons, why the datasets from the top of the *in situ* measurement sites were used for the validation tasks. These covered approximately the same area with their field of view (FOV) as a satellite pixel would, meaning that each *in situ* site and its surrounding area matched the input area of approximately one remotely-sensed mixed pixel with 30 m spatial resolution.

3.2.3 Clouds and temporal coverage

One of the strongest limiting factors for passive remote sensing data are clouds, which make the data useless if one is interested in surface data and not in cloud studies. There is no possibility to correct this influence and therefore clouds must be masked out before further processing of the data which is also a difficult task due to the different kind of clouds; e.g. cirrus clouds or extremely translucent clouds are especially hard to detect but have a high impact especially on TIR images. Together with the clouds, the temporal coverage is another limiting factor for remote sensing data especially if the IOP period is limited. Many datasets were omitted due to cloud cover in this work; some scenes with partial cloud cover were used with caution.

3.2.4 Bidirectional reflexion distribution function

The bidirectional reflexion distribution function (BRDF) (Nicodemus et al., 1977) describes the ratio of reflected radiance exiting from a surface in a particular direction to the incoming irradiance incident on the surface from the incoming direction over a particular waveband. This means that remotely sensed land surface reflectance is dependent upon the changing sun and sensor viewing geometry which is itself governed by the BRDF. For remotely sensed data many BRDF models were developed

depending on wavelength and sensor. For the AVHRR and MODIS –which have a wide swath width and, as mentioned, different viewing angles at their borders from those at their nadirs– the BRDF function is especially necessary to calculate what a sensor really measures with each pixel. The BRDF is normally either implemented into or coupled with atmospheric correction processing.

3.2.5 Urban anisotropy

When working with very high resolution spaceborne or airborne remote sensing data over urban areas an important factor is the problem of urban anisotropy is an important factor (discussed in Soux et al. (2004) and Voogt & Oke (1998)). Urban anisotropy describes the fact that, even with very high resolution data the entire urban surface (consisting mainly of walls, streets and roofs) cannot be registered due to the viewing angles and canyon structures of a city. Some models are in development to solve this problem for idealized surfaces but have never been applied to specific real-world cases.

3.3 Meteorological parameters

3.3.1 Radiation flux densities

When considering the energy budget of the Earth's surface, there is one term of striking importance, namely, the net radiation. This is a measure of the amount of available energy on the Earth's surface and is governed by four components:

$$Q_{SU} + Q_{SD} - Q_{LU} + Q_{LD} = Q^* \quad (3.7)$$

With :
- Q^* net (all-wave) radiation
- Q_{SU} shortwave upward radiation
- Q_{SD} shortwave downward solar radiation
- Q_{LU} longwave upward terrestrial radiation
- Q_{LD} longwave downward radiation

The equation is sometimes rewritten as

$$Q^* = (1 - \alpha)\, Q_{SD} + Q_{LD} - \varepsilon\sigma_B T_s^4 \quad (3.8)$$

where α is the broadband albedo, defined as the absolute value of the ratio $\alpha = |Q_{SU}/Q_{SD}|$, ε is the long-wave broadband emissivity of the surface, σ_B is the Stefan-Boltzmann constant and T_s is the radiant surface temperature.

Generally all radiation directed towards the Earth's surface is interpreted using positive values, while outgoing radiation is represented using negative values. From a long-term global view, the net radiation of the Earth is zero (in thermal balance). Otherwise, the Earth would cool down or heat up steadily and significantly. For a single point, an area, or even a large region, the net radiation changes at regular intervals; daily and yearly, depending on the sun's position relative to that specific area (i.e. the time of the year).

Direct and reflected diffuse short-wave radiation are both positive during daytime and reach their peak at midday. At night both values are zero. For long-wave radiation, reflected and emitted, values stay almost steady throughout the day, the counter radiation (Q_{LU}) being slightly higher during daytime than at night (see Figure 3.2).

The net all wave radiation (Q^*) is positive from shortly after sunrise until shortly before sunset, peaking at midday. At night the net radiation is negative with the most negative value occurring shortly after sunset. The nightly negative values arise from the Earth continuing to emit long-wave radiation after incoming shortwave solar radiation has stopped. As night progresses, though, surface temperatures cool down and long-wave emission decreases; hence the pattern of rapid reversal of energy flow followed by stabilization.

The described daily pattern can be seen in Figure 3.2 (for July 8, 2002). There is a small decrease in Q_{SD} ca. 11:40 a.m. and ca. 6:50 p.m., when clouds shaded the measurement site. It is clear how strong an impact clouds have on the net all wave radiation. Note also the differences between rural (Figure 3.2 a)) and urban (Figure 3.2 b)) with the rural site having a higher Q_{SU} and a lower Q_{LU} when

compared to the urban one. The cloud cover (at about 5:00 p.m.) mostly affects the short wave compontents and the net all wave radiation Q* whereas the influence on longwave components is only slight.

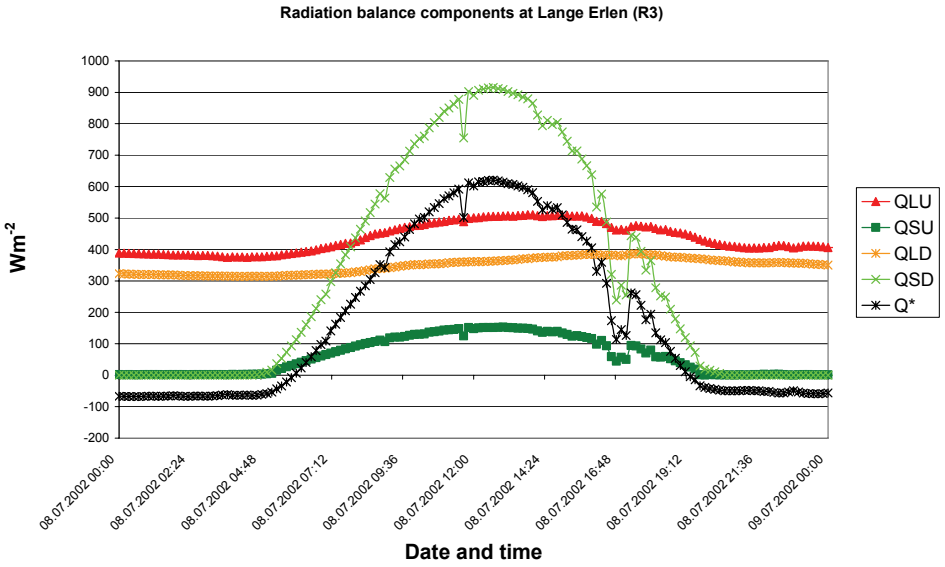

a)

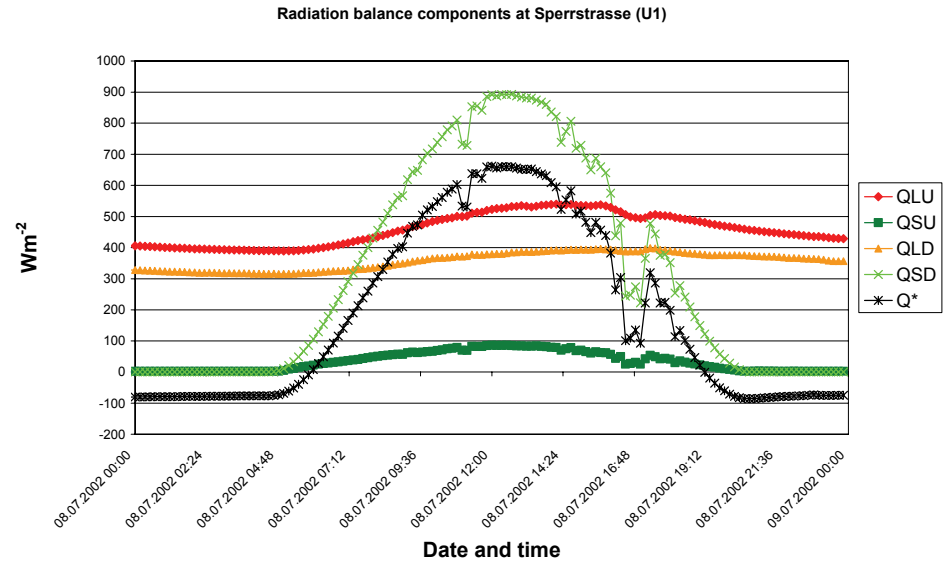

b)

Fig. 3.2: Radiation balance components for the 08.07.2002 at the a) Lange Erlen (R3) and b) Sperrstrasse (U1) sites. This figure shows a typical daily pattern of these components in summer. There is a sudden decrease ca. 4:45 p.m. when a cloud blocks the shortwave downward radiation. Time is given in CET.

Q_{SD} consists of direct and diffuse radiation and is influenced by the urban environment. According to Landsberg (1981) Q_{SD} is approximately 10% less in urban environments than in rural ones. This difference results from the higher concentration of aerosols above a city which inhibits direct radiation input but slightly increases the diffuse part of Q_{SD}. For the City of Basel, however, as reported by

Christen & Vogt (2004), this difference is virtually non-existent over the average period of the IOP and only a minimal difference can be found between Figure 3.2 a) and b).

The albedo α is influenced by the urban structure and is responsible for the influence of urban canopy configuration on the net radiation Q*. Kondo et al. (2001) found in their model that the albedo α decreases as building height increases and building height distribution uniformity decreases. This point was also first noted by Aida (1982).

In rural environments (around 20% for R2) the albedo is usually higher than in urban ones (around 11% for U2) therefore resulting in a lower shortwave net radiation Q_S* (Q_S* = Q_{SD} – Q_{SU}) in rural environments. The larger shortwave input Q_S* of the urban surfaces due to the lower albedo is mostly offset by larger longwave net radiation Q_L*(Q_L* = Q_{LD} – Q_{LU}) loss. The longwave net radiation Q_L*, on the other hand, is higher in an urban environment due to the surface properties of urban structure and canyons.

Generally all these factors result in a slightly lower net radiation over an urban surface compared to a rural one. According to Christen (2005), however this difference is almost zero when aggregated over a longer period in the City of Basel.

These observations are valid when data from the *in situ* measurements was analyzed over a longer period (for details see Christen & Vogt (2004)). Actual daily values can differ according to the day of year (DOY) and therefore seasonal change of the albedo over rural surfaces for example. Of course the transmissivity of the urban atmosphere due to water vapour and aerosols also influences the radiation balance components.

3.3.2 Heat flux densities

The energy of the net all wave radiation is distributed to other heat (or energy) flux densities. These heat flux densities have to fill the gap when the radiation balance is negative and are recorded as the sensible heat flux density (Q_H), the latent heat flux density (Q_E) and the ground (or storage) heat flux density (ΔQ_S) (sometimes noted simply as Q_S). In urban areas an anthropogenic heat flux density (Q_F) is also occasionally added. The left part of equation 3.9 corresponds to the net all wave radiation; the right side gives the heat flux densities.

$$Q^* = \Delta Q_S + Q_E + Q_H + (Q_F) \tag{3.9}$$

With

$$Q_H = \frac{\rho c_p}{r_H}(T_a - T_s) = \overline{\rho} c_p \left(\overline{\omega' T_S'}\right)_0 \tag{3.10}$$

and

$$Q_E = \frac{\rho c_p}{\gamma^* r_H}(e_{s(T_s)} - e) = L_\upsilon \left(\overline{\omega' \rho_v'}\right)_0 \tag{3.11}$$

where γ* is the psychrometer constant, which is a function of the barometric pressure and is not actually a constant. The surface temperature T_s must not be confused with the acoustic temperature T_S or the air temperature T_a.

The first parts of equations 3.10 and 3.11 describe how the heat flux densities can be calculated with a bulk transfer assumption. The second parts describe how they can be calculated with *in situ*

measurements from three-dimensional ultrasonic-anemometer-thermometers (also called Sonics) using the eddy-covariance method (see also Christen & Vogt, 2004; Oke, 1990).

The heat flux densities are dependent on the surface material, the structure of the material and density of vegetation. The way the available energy in these heat flux densities is distributed has a large influence on the climate of an area. As a general rule, for the purpose of this work, all radiation and heat flux densities directed towards the Earth's surface are noted positive and all directed away from the Earth's surface are noted negative.

To show the daily distribution of the heat flux densities and the net radiation in urban, suburban and rural areas a graph for each site is presented in Figure 3.3. The data are from July 8, 2002, during the BUBBLE-IOP.

Whereas a) is an urban site with very high ΔQ_S and also high Q_H values during the day, b) is a suburban site where all three heat flux densities are of almost equal size during the day, with a slightly higher ΔQ_S at night. The last of the graphs, c), shows the values for a rural site with Q_E being the dominant flux density during the day and ΔQ_S and Q_H showing much lower values. The latent heat flux density Q_E is also not equal to zero at the urban site even though there is only impervious surface.

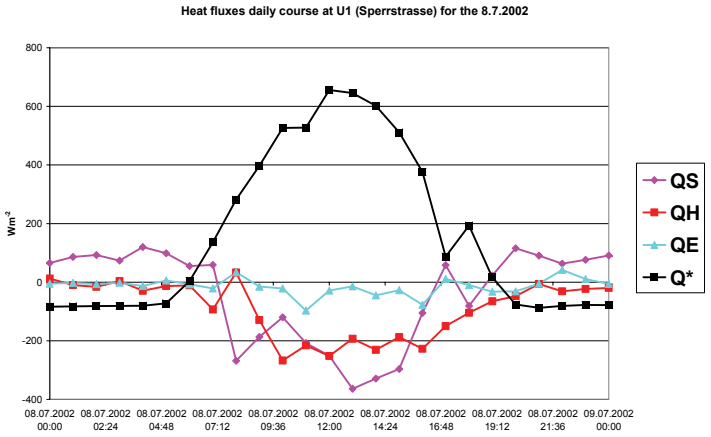

a) Site U1

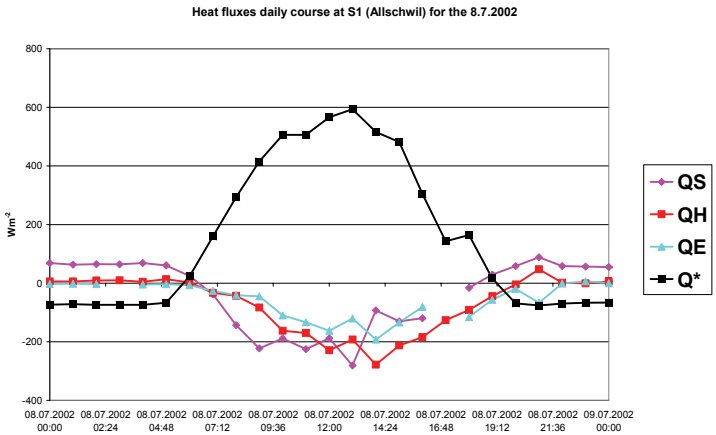

b) Site S1

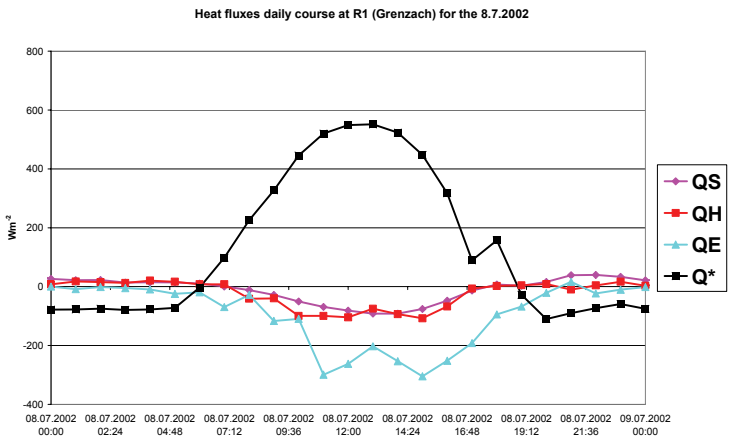

c) Site R1

Fig. 3.3: Heat flux densities for July 8, 2002 for the U1, S1 and R1 sites of the BUBBLE-IOP

For the measurement and modelling of turbulent heat fluxes a wide variety of models are available. One of the most commonly used is the two source energy balance model of Norman et al. (1995), a modified version of which was used by Kustas et al. (2003), Kustas et al. (2004) and French et al. (2005) for rural areas. A similar model was developed by Anderson et al. (1997) using the Leaf Area Index (LAI) for vegetation assessment, whereas Jiang & Islam (2003) used the NDVI. For the validation of AVHRR derived heat flux densities Gao et al. (1998) used also *in situ* datasets. The common factor of all these publications is the fact that they focus mainly on homogenous rural areas. On the other hand, evapotranspiration in urban areas with impervious surfaces can be almost negligible. Therefore some of the models mentioned that apply vegetation indices, evapotranspiration or height of vegetation are not suited for urban environments. Because of the heterogeneity of the urban surface and the very low evapotranspiration in urban areas, another approach was used in this paper. As with various other approaches, surface parameters such as soil humidity, wind speed and air temperature were not considered, due to the urban structure (and therefore the considerable modification and spatial changes it has on these factors) as well as the difficulties involved in measuring soil humidity and other vegetation specific parameters in an urban environment.

According to the model developed by Zhan et al. (1996), the differences for the sensible heat flux density are sensitive to errors in air and surface temperatures. They showed, for example, that a 10% error in surface temperature can result in an error of over 50% in predicted heat flux density. If we assume that our accuracy, according to Rigo et al. (2006), is in the range of 3% to 4%, and applying the approach of Zhan et al. (1996), the errors in sensible heat flux density can be expected to range from 20 Wm^{-2} to 40 Wm^{-2}. As mentioned by Schwiebus et al. (2005) for their approach, relative humidity and wind speed show an inaccuracy of about 40 Wm^{-2} for the latent heat flux density. This shows that uncertainties in input parameters can change the results considerably –depending, of course, on the model and its sensitivity. The advantage of Eddy-covariance measurement and modelling of the heat flux densities with sonic anemometers is described by Twine et al. (2000). They report an uncertainty of 10% for their measurements over a grassland site.

Approaches for local scale urban area modelling of heat flux densities were also conducted, but without remote sensing data. The Town Energy Balance (TEB) model of Mestayer et al. (2005) was applied during the ESCOMPTE experiment in Marseille to model the daily course of the turbulent heat flux densities. Another local urban model is the LUMPS, which was used by Grimmond & Oke (2002).

3.4 Urban climatology and remote sensing

The fact that urban climates differs from those of surrounding areas was first realized by Luke Howard in 1820. Since then many different authors have conducted extensive research regarding the various aspects of urban climate. Arnfield (2003) provides an excellent overview of this topic.

Since Howard's discovery, researchers have developed the concept of the urban heat island (UHI), which involves the phenomenon that, after sunset, urban areas show higher air temperatures than their rural surroundings. The normal UHI-index shows an air temperature T_a difference between rural and urban sites of approximately 2-4 K for European cities. For US cities the UHI-index can be even higher. This sensation of the UHI is also dependent of the climatic zone in which the city lies and is, e.g., more welcome in an otherwise cool climate than in a generally hot environment. The expression "urban heat island" has to be applied with great care, though, because it is time dependent. During daylight hours the air temperature in the city itself can be cooler than outside of the city. Even through the seasons the temperature differences vary (see Figure 3.4 below) and during the day the city itself can even become an urban cool island (UCI).

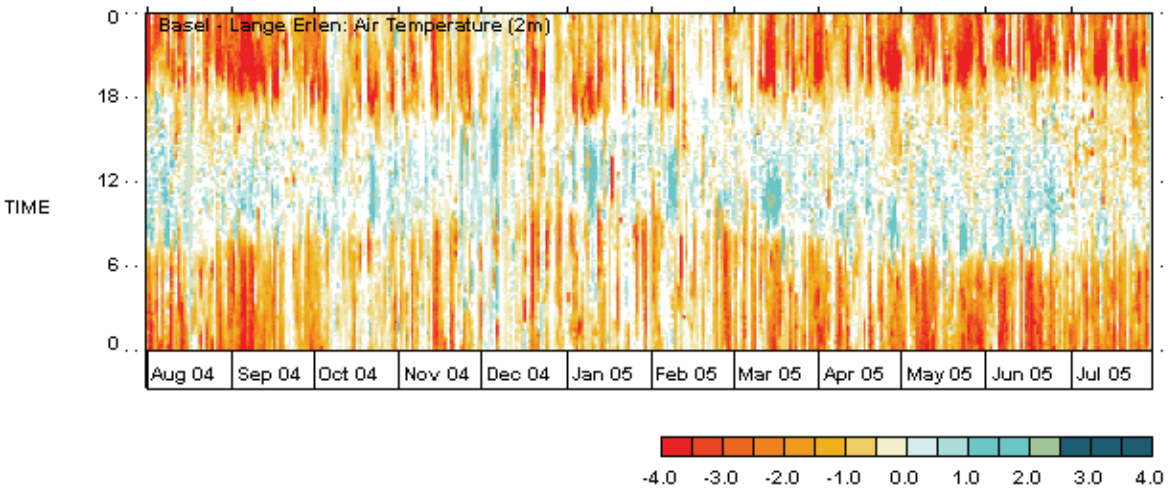

Fig. 3.4: Temperature differences between the sites Klingelbergstrasse (urban) and Lange Erlen (rural) sites for one year. The blue colour denotes lower air temperatures in the city, whereas the red colour stands for higher air temperature.

It is clear that impervious surfaces modify the climate in urban environments, but although punctual measurements of the surface temperature with drive-through transects are possible, these spot measurement still do not provide the entire spatial surface temperature T_s distribution in a city. The higher surface temperature in a city is called the surface urban heat island (SUHI) for a clearer distinction (see Figure 3.5). For an extended overview of the remote sensing of urban climates see Voogt & Oke (2003).

Figure 3.5 below shows the longwave upward radiation of the City of Basel from the LANDSAT ETM+ image of July 8, 2002 at 10:00 UTC with a clearly distinguishable SUHI. The surface temperature T_s was converted into radiation flux densities [W/m^2] using the law of Stefan-Boltzmann (eq. 3.2) for a better comparison with the *in situ* measured longwave emission data.

The UHI and the SUHI therefore are not the same; and even if there is a SUHI, this does not mean that there also has to be a UHI at the same time. The SUHI can be measured by thermal infrared remote

sensing, whereas the UHI cannot be seen in a spatial context: it is derived from the difference in air temperature (T_a) between urban and rural stations. Only some drive-through measurements can give an overview of the temperature profile of a small area. As can be seen in Figure 3.4 an UHI is generally present after sunset in the City of Basel, whereas a SUHI can be present at all times but with varying intensity. In the northwest and southeast respectively, the airport and the industrial areas are clearly visible with very high Q_{LU} values; while the River Rhine shows comparatively low values as it flows through the city. After the river, the forest areas show the lowest values.

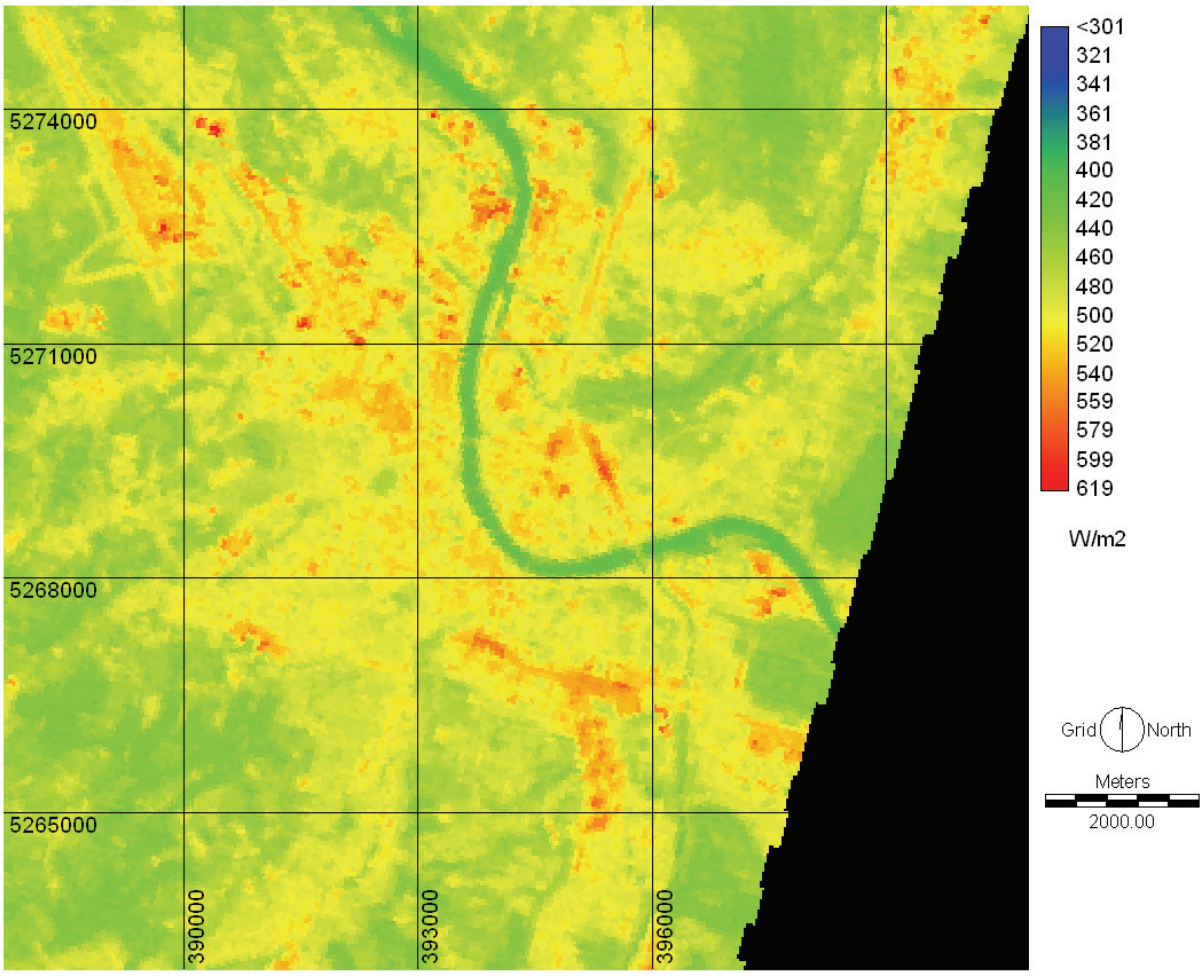

Fig. 3.5: LANDSAT ETM+ image (in Wm^{-2}) showing the longwave upward radiation July 8, 2002 at 10h UTC

One of the earliest studies to use thermal infrared remotely sensed images and monitoring of urban areas was conducted by Price (1980). As the technical development of satellite remote sensing and also of computing power and hardware have improved in the last three decades, though, more and more research has been conducted on the topic (Munier & Burger, 20001; Nichol, 1998 or Parlow, 1999). Although UHI and SUHI are not directly connected, they are still indirectly connected through the radiation and energy balance equations (eq 3.7 and eq. 3.9). The energy available from the net radiation (of which the long wave upward Q_{LU} radiation is also a part) is distributed to the heat flux densities according to equation 3.9. Therefore, part of the available energy also goes into the sensible heat flux density, which is responsible for the air temperature and therefore for the UHI after sunset.

The urban energy and radiation balance is clearly different from that of rural areas (Oke, 1990); therefore most models or approaches valid for rural areas cannot be easily applied to urban environments. If they are, they have to be validated with available *in situ* data. Many validations and modellings of net radiation and heat flux densities have been conducted over homogeneous rural surfaces by Kustas et al. (2004), Kustas et al. (2003), Ma et al. (2003), Norman et al. (1995), Santanello & Friedl (2003) and Zhan et al. (1996). Over urban areas, however, these models were not used or were not validated, due to the heterogeneity of the urban surface and *in situ* data availability. Also, some other restrictions limit the usability of these models compared to rural areas, e.g., there is no vegetation canopy height in an urban area. All the effects urban areas have on climate have an impact on the inhabitants of these areas. Therefore, modelling the spatial distribution of radiation and heat flux densities in the spatial domain is a matter of considerable importance.

4. Data

4.1 Radiation measurements

The Kipp & Zonen CNR 1 Pyranometers operated at the energy balance sites were intercompared side-by-side during a field intercomparison in July 2002 in Southern Italy, just after the BUBBLE experiment ended. There, four of the five CNR 1 used in this work were compared to a Kipp & Zonen CM21 (Pyranometer) and an Eppley PIR (Pyrgeometer), which had both been recently calibrated by the World Radiation Centre (WRC) in Davos, Switzerland. The calibration factors derived from this week long intercomparison confirmed that shortwave downward radiation Q_{SD} measured with a CNR 1 is generally underestimated by 2%. This discrepancy can be attributed to instrumental problems, since it was observed systematically and significantly with all four instruments involved.

Longwave downward radiation Q_{LD} measured by CNR 1 instruments show a small, systematic dependence on Q_{SD} (pers. comm. R. Vogt). Hence, an additional f_k factor in the range of -0.02, introduced to correct the shortwave sensitivity of the long-wave sensor was determined for each instrument individually.

The upward-facing instruments were modified with three dome thermistors separated by 120° and were corrected according to Philipona et al. (1995). The downward facing instruments had only 1 dome thermistor.

The radiation data was necessary for the validation and calibration of the thermal IR datasets, as well as of the net all wave radiation, which was also used as an accurate basis for the modelling of the storage / ground heat flux densities.

All of the eight sites measured all radiation flux densities (longwave, shortwave, up and down) and the net radiation. The data were measured at approximately two times z_h at the built-up sites (except at U3 where it was measured 2 m above the concrete surface) and 2 m above ground at the rural sites. Periods with dew on the sensor – observed uniquely at the rural sites – were detected using the differences between dew point and case temperature, then masked out by visual inspection. The resulting missing data were linearly interpolated for gaps shorter than 2 h. Gaps with a longer duration were homogenized with the nearest site of similar land use. The data for validation and comparison were available as 10-minute averages.

4.2 Storage/ Ground heat flux density measurements

At the rural sites (except R4, which was not equipped), the ground heat flux density was measured directly by means of four soil thermistors and three heat flux plates inserted at a depth of between 3 and 5 cm. It was corrected for flux density divergence in the soil layer above the plates using measured soil temperatures. The average daily value of the ground heat flux density for rural areas is approx. -60 Wm^{-2}, which corresponds to 10 -15% of the net radiation (Christen & Vogt 2004). Heat flux plates are prone to measurement errors which are associated with various problems such as poor plate contact with the substrate. Twine et al. (2000) note a probable error of 15% in soil heat flux measurements with heat flux plates, even with careful calibration. Instrument accuracy may also cause an error of up to 20% according to Weber (2006) who made some research with heat flux plates in a heterogeneous urban ballast layer. Spatial variability of ground heat flux density in rural environments is low.

The ΔQ_S (or simply Q_S) of an urban surface incorporates all storage into artificial surfaces (streets, buildings), into urban vegetation and into the ground (Grimmond & Oke 1999). Measuring the ground heat flux densities of urban surfaces is even more difficult than for those of rural areas (Weber 2006). As discussed by Weber (2006) for urban and Twine et al. (2000) for rural environments, ground heat flux density is mostly estimated as residuum from eddy-covariance measurements, because the use of heat flux plates in urban environment is still at an experimental stage. Therefore the ground heat flux density for the urban sites was determined as a residual factor for the closing of the energy balance (equation 3.9). The errors for different methods of measuring ground heat flux density are described by Weber (2006), who found relative deviations of up to 31% for heat flux plate measurements and 38% for the residual term from the eddy-covariance method when he made measurements in a heterogeneous urban ballast layer.

Most energy balance measurements over natural and agricultural surfaces that directly measure all flux densities show that the balance in eq. 3.7 is not zero. The gap remaining in the closure is approximately 20% of Q* (Oncley et al. 2002; Wilson et al. 2002). For the R1 and R2 measurement sites the average daytime closure gap was 17% and 18% percent respectively; during the nighttime it reached 30%. It is obvious, that whenever ΔQ_S is determined as a residual term from the eddy-covariance method (sites U1, U2, S1) there is no closure gap by definition. Therefore any ΔQ_S calculated as a residual term must be interpreted as an upper limit.

Due to limited data availability and difficulties with the ground heat flux density measurements in urban environments(see also Weber, 2006), hourly values for the respective satellite overpass times for all clear-sky days during the IOP were averaged for the comparison with the modelled data (see Figure 4.1). Larger gaps and obviously wrong data were masked out by visual inspection

It is clear, that for the R1 rural site (Figure 4.1 c)) the differences between the clear-sky days average and the values from July 8, 2002 are quite low. This is also due to the low daily dynamic range of the ground heat flux density in rural environments, as well as of the rather low values of the flux densities themselves.

As for S1 and U2 the values show much higher differences. The course of the ground heat flux density is far more representative at the averages than the daily values, which makes the average values more realistic – especially at U2 – where no useful data were available in the morning hours due to instrument errors.

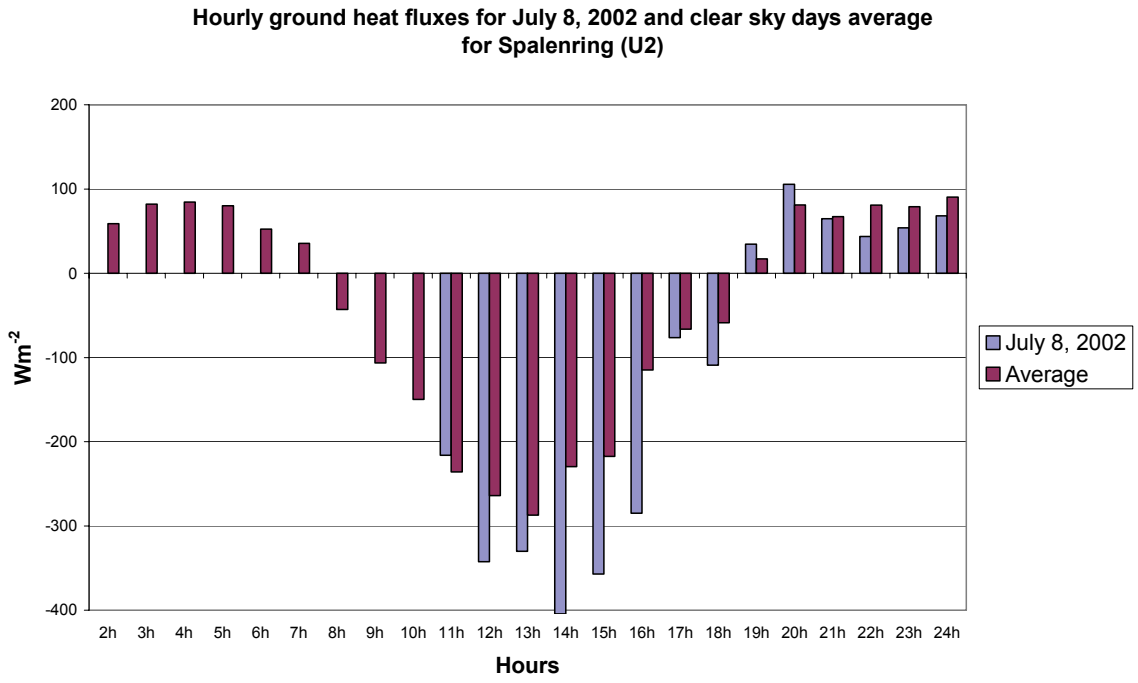

a) Urban U2

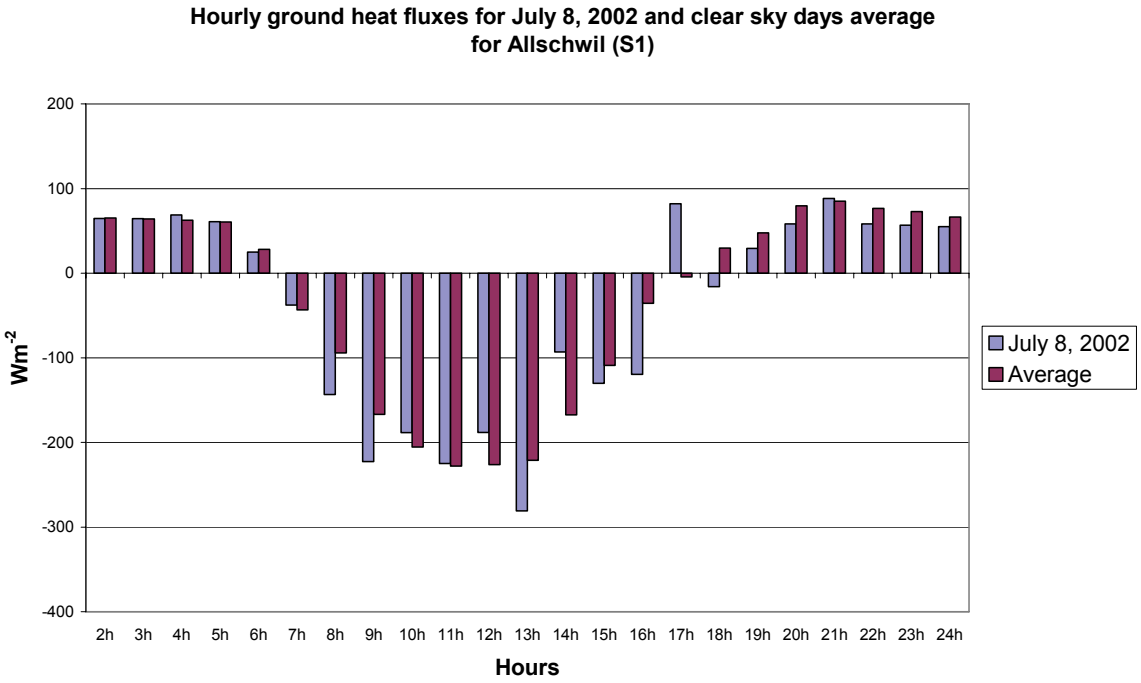

b) Suburban S1

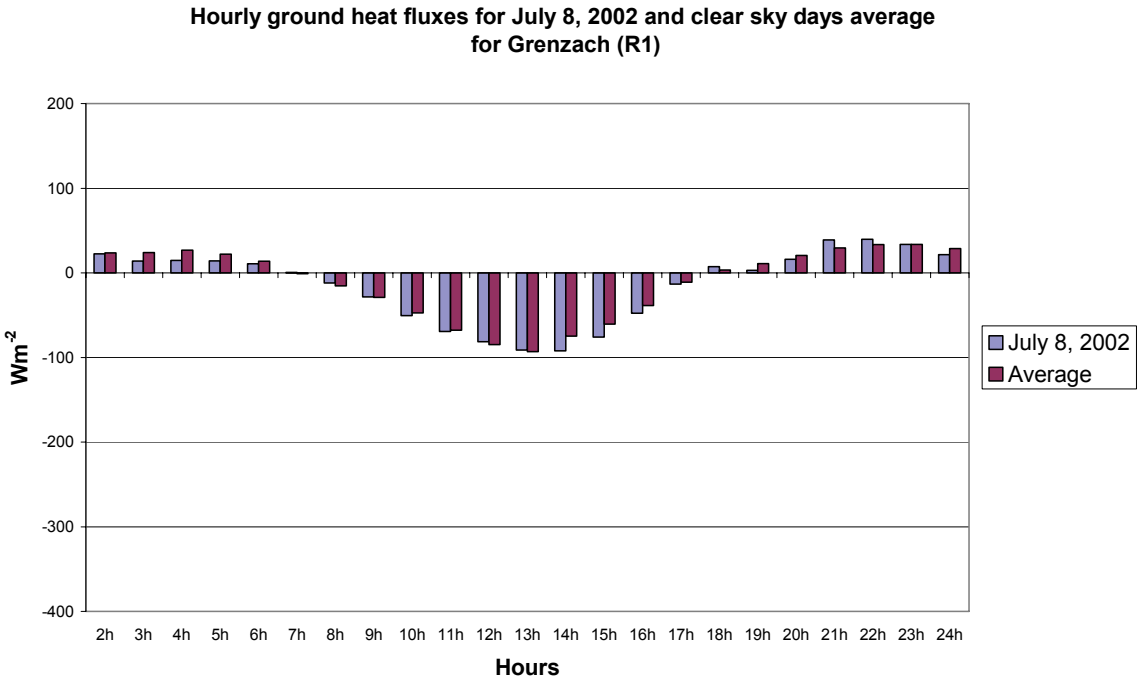

c) Rural R1

Fig. 4.1: Daily course of ground heat flux density at three sites a) U2, b) S1 and c) R1 from July 8, 2002 compared to the average clear sky values during the BUBBLE IOP.

4.3 Turbulent heat flux densities measurements

Sensible heat flux density Q_H and latent heat flux density Q_E were directly derived from eddy correlation measurements using three-dimensional ultrasonic anemometer-thermometers combined with humidity fluctuation measurements. The data were calculated as described by eq. 3.10 and 3.11. Q_H and Q_E were calculated from block averages of 20 Hz raw data averaged over one hour. All instruments were checked and outputs compared in the wind tunnel (except the instrument at U3). Q_H was calculated from the covariance of acoustic temperature and vertical wind $\overline{\omega' T_S'}$, which was corrected for crosswind either internally by the sensor electronics or during post processing and for special loss (Moore, 1986).

Additionally, Q_H is corrected for humidity effects (Schotanus et al., 1983). This humidity correction reduces the magnitude of the raw $\overline{\omega' T_S'}$ by 3% at the urban sites and by 13% at the rural sites, because the rural sites have higher evapotranspiration.

Q_E was calculated from the covariance of absolute humidity and vertical wind $\overline{\omega' \rho_v'}$ including a correction for O_2 sensivity (Tanner et al., 1993) and a small vertical wind component (WPL-correction, (Webb et al., 1980)). Furthermore, a spectral correction was calculated taking into account sensor separation (Moore, 1986).

The eddy-covariance data used for this calculation were collected at the highest point of the urban and suburban sites – approximately 30 m for U1 and U2, 10 m for S1, and 2 m for U3. This is the height above the entire surrounding roof level, and was chosen with the intention of covering the surrounding area as similarly as possible to the FOV of a remotely sensed pixel, since the satellite, due to its limited spatial resolution, cannot see into the urban canyon. The turbulent flux densities were only measured at U1, U2, U3, S1 and R3, thus reducing the number of sites available for validation to five. The datasets were aggregated to one-hour averages. Due to the general difficulties presented by turbulent flux measurements, the data were also averaged from the same clear sky days as they were for the ground heat flux density. Gaps and obviously wrong data were masked out and removed from the dataset after visual inspection.

4.4 Remote sensing data

Of the numerous satellites orbiting Earth, the focus of this work is on those with sensors either in the thermal infrared wavelength or in the visible and near infrared bands of the spectrum. Generally for all satellites working with optical (passive) sensors, data usability is strongly influenced by clouds, especially in the thermal infrared spectrum. Because many of the recorded scenes were completely unusable due to cloud contamination, then, in addition to the above-mentioned viewing angle problems, the theoretical number of available datasets collected by the satellites mentioned is far greater than the number finally used for this work (see Appendix B). An overview of the used satellite sensors and number of scenes used can be found in Table 4.1.

Nevertheless, for these datasets, a multitemporal coverage of the BUBBLE-site and the city of Basel was possible for several days with many overpasses at different times of day. The scenes were all georeferenced to UTM Zone 32N, WGS-84. For detailed information about the data, pre-processing and processing, see Chapter 5.

The transformations between the pixel resolutions were all executed using the nearest neighbour method to assure as accurate data as possible. This process makes the images less smooth to view but conserves the maximum amount of information. After the atmospheric correction, all data (except that from the Quickbird and VarioCam) were transformed to 30m spatial resolution.

a) LANDSAT ETM+

The LANDSAT platform has one of the longest recording histories of any satellite. The latest of the series, LANDSAT ETM+ (Enhanced Thematic Mapper plus), offers an unmatched 60 m resolution in the thermal-IR band, making it the satellite with the highest resolution used for this work. In the visible and near infrared ranges, it offers 30 m resolution with a total of 6 channels and has additionally one panchromatic channel with 15 m resolution. Unfortunately, the satellite failed partially in May 2003, rendering its thermal infrared products (called SLC-off) useless. The repetition rate of the satellite is 16 days.

b) AVHRR

The Advanced Very High Resolution Radiometer (AVHRR) on different NOAA Polar Orbiting Environmental Satellite (POES) platforms (12, 14, 15, 16 and 17) (therefore called AVHRR-12, 14 and so on) has an even longer record, starting from 1978. It offers two thermal channels and three in the visible and near infrared ranges. Beginning with model AVHRR-15, the instrument was expanded to include a sixth band in the near infrared range. It offers a spatial resolution of 1.1km in all channels; due to this wide swath it covers the research area with two overpasses every 24h.

c) MODIS

The Moderate Resolution Imaging Spectrometer (MODIS) sensors on board TERRA and AQUA are among the newest medium resolution sensors, covering the Earth in a sun-synchronous orbit. It offers 36 bands, covering wavelengths from the visible (250m resolution) across the near infrared (500 m resolution) to the thermal infrared (1000m resolution). Their two satellites, TERRA and AQUA, are sisters, launched in two consecutive years. The BUBBLE-IOP was only covered with data from MODIS/ TERRA, so no distinction was made in the text. For the 2003 data, the two MODIS sensors are distinguished regarding their respective platforms. MODIS is similar to the AVHRR and offers a

daily coverage of two scenes of the research area (one night, one day). With both TERRA and AQUA active the number of theoretically available MODIS scenes was four per day in 2003.

d) ASTER

The Advanced Spaceborne Thermal Emission and Reflection Radiometer (ASTER) is one of the latest high resolution satellites. ASTER is aboard TERRA, sharing its satellite platform with MODIS. It has 14 channels and offers a spatial resolution of 15 m in the visible and near-IR bands, 30 m in the mid-IR band and 90 m in the thermal-IR band. The normal repetition rate is the same as LANDSAT ETM+, with a revisit every 16 days.

ASTER offers the unique possibility to check the model made using datasets from 2003 and also to evaluate how datasets from ASTER can be used to substitute for the LANDSAT ETM+. Because ASTER does not record continuously, like LANDSAT ETM+, but mostly on request, no data were available from 2002 covering the BUBBLE-IOP. Nevertheless, all available overpasses from 2000 to 2005 with low cloud coverage percentage (below 20%) covering the research area were acquired and processed, and the longwave upward radiation was validated with *in situ* data. Further processing of the ASTER datasets was only conducted with the data from 2003.

e) Quickbird

As very high resolution dataset a Quickbird image was acquired on February 4, 2002 at 10:31 UTC while the BUBBLE campaign was running but was not yet in the IOP phase. Due to the financial and temporal restrictions of Quickbird data this was the best dataset available, with an excellent quality rating. Because it recorded only 6° off nadir, its image distortion was minimal. The spatial resolution of the data is therefore 0.63m per pixel for the panchromatic and 2.48 m per pixel for the multispectral data. The Sperrstrasse (U1) area is shown in RGB and panchromatic images in Figure 4.2 to illustrate the resolution of the data.

Considering the very high resolution of the images, the scene was specially georeferenced by D. Raaflaub with a differential Trimble® GPS to UTM Zone 32N, WGS-84 for highest accuracy. Both multispectral and panchromatic images were available; the panchromatic image was used for the geocoding of the VarioCam datasets. Because the data were used only for albedo (panchromatic image), NDVI and the calculation of a land use classification map, no atmospheric correction was applied to the dataset.

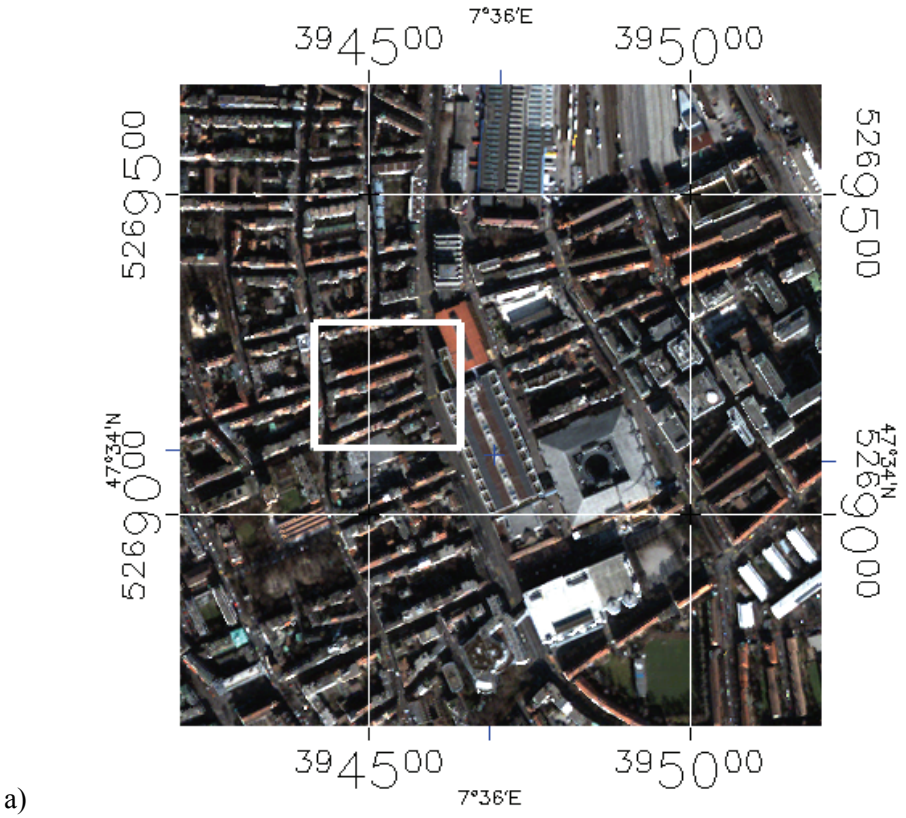

a)

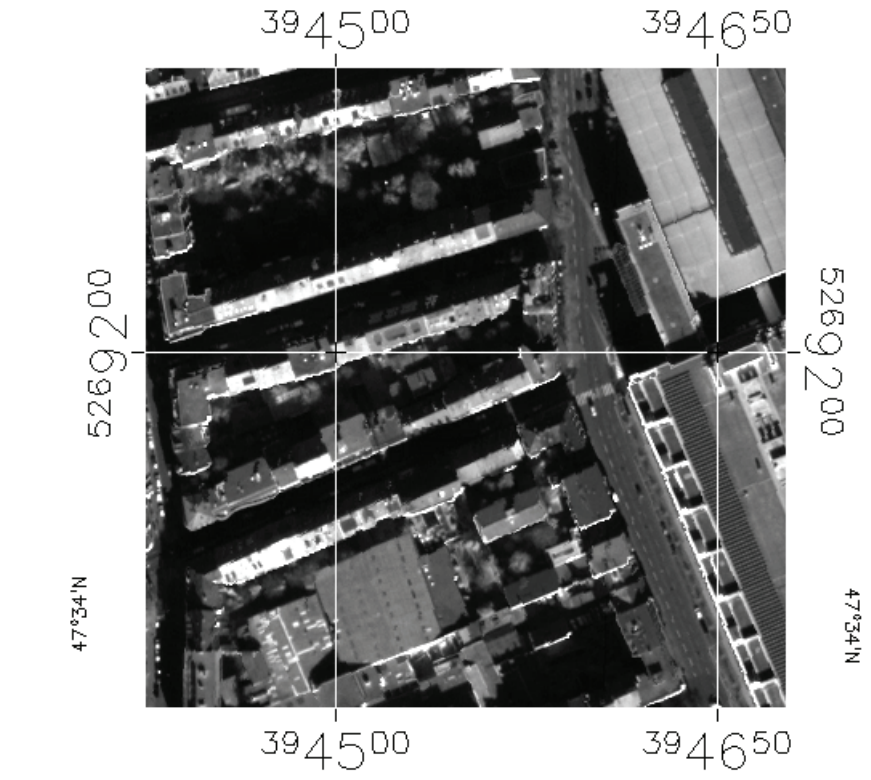

b)

Fig. 4.2: Quickbird images from the Sperrstrasse areas a) RGB and b) Panchromatic, with 2.48 m and 0.63 m spatial resolution respectively. The images are georeferenced to UTM Zone 32 North, WGS-84 and north oriented. The panchromatic image (b)) is represented in a) as a white box. Quickbird data was acquired from DigitalGlobe.

Tab. 4.1: The satellites and their basic parameters

Satellite	LANDSAT ETM+	MODIS Aqua	MODIS Terra	AVHRR 12	AVHRR 14	AVHRR 15	AVHRR 16	AVHRR 17	Quickbird	ASTER
Temporal Coverage	16 Days	Daily twice	Daily twice	Daily	Daily	Daily	Daily	Daily	On demand	16 days /on demand
No. of Spectral Bands	7 + 1 panchromatic	36	36	5	5	6	6	6	3 + 1 panchromatic	14 + 1 stereo
Thermal Bands	1 high + 1 low	2	2	2	2	2	2	2	None	5
Spatial Resolution	15m, 30m, 60m	250m, 500m, 0.93km	250m, 500m, 0.93km	1.1 km	1.1k m	1.1 km	1.1 km	1.1 km	0.63m, 2.53 m	15m, 30m, 90m
Radiometric Resolution	All bands 8 bit	All bands 12 bit	All bands 12 bit	All bands 10 bit	All bands 10 bit	All bands 10 bit	All bands 10 bit	All bands 10 bit	All bands 11 bit	VNIR and SWIR 8 bit, TIR 12 bit
Altitude	705 km	705 km	705 km	833 km	833 km	833 km	833 km	833 km	450 km	705 km
No. of scenes during BUBBLE	1	none	13	none	5	4	7	none	none	none
No. of scenes outside of the BUBBLE- IOP	1	7	6	4	7	8	2	5	1	6
Operational since	1999	2002	2000	1991	1994	1998	2000	2002	2000	2000

4.5 VarioCam data

On July 16, 2004, we had the opportunity to make a flight over the city of Basel with a thermal infrared camera aboard a helicopter which was unfortunately not possible during the BUBBLE campaign itself. On board the helicopter was a VarioCam head, made by InfraTec. The images were taken in an east-west and west-east overflight path. Unfortunately the thermal infrared camera was not yet available during the BUBBLE campaign. The resolution of the VarioCam is 320 x 240 pixels per scene. More information can be found in Table 4.2 below

Tab. 4.2: Technical specificaions of the VarioCAM head (www.infraTec.de)

Technical data VarioCam	
Spectral range	8-13 µm
Sensor (Pixel)	Focal Plane Array (320 x 240)
Detector	Microbolometer, uncooled
Temperature range	-40…1.200 °C, optional > 2.000 °C
Accuracy	±2 K, ±2 %
Temperature resolution @ 30°C	< 0.1 K
IR-Image frequency	50 Hz
Normal lense (Field of view)	25 mm (32 x 25)°

The data were mosaicked by S. Raaflaub to form a thermal image of the city of Basel with a 30-minute overpass time between 10:45 and 11:15 (UTC). Approximately 400 individual pictures were georeferenced and merged together. The original resolution of the images was between 1 m and 1.5 m per pixel (average overflight altitude was between 400 to 500 m). The images have been resampled to a 0.63 m resolution based on a Quickbird panchromatic image to fit the 1 m digital city elevation model (DCEM) (see Figure 4.3). With this high-resolution dataset a very detailed image of the SUHI was obtained.

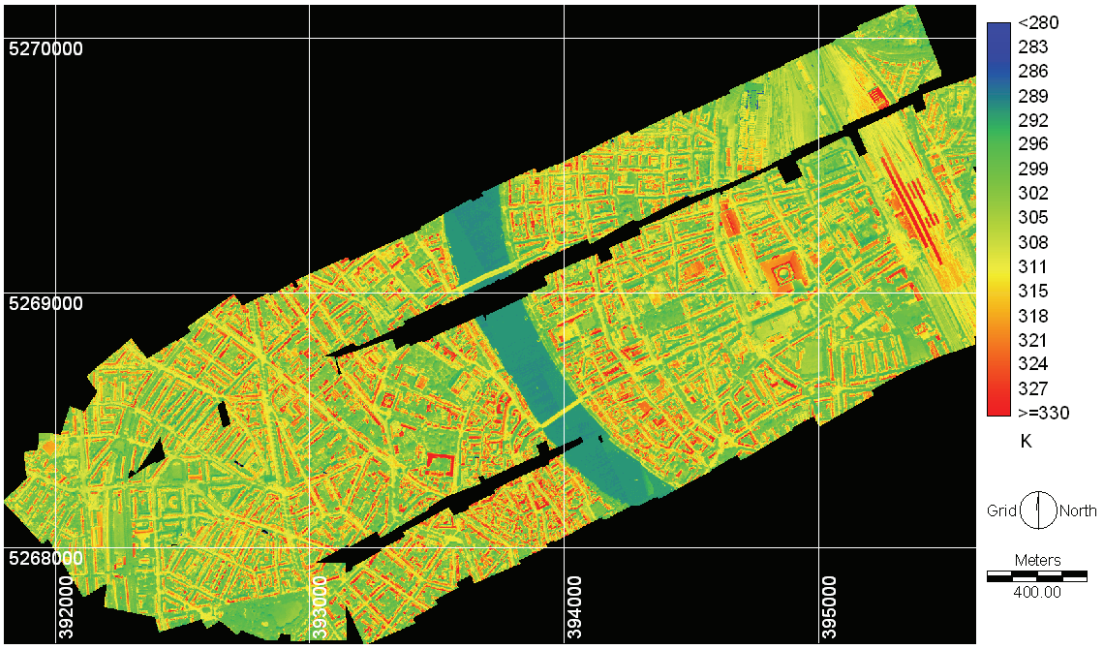

Fig. 4.3: The VarioCam data mosaic of the city from July 16, 2004

4.6 Additional data

In addition to the data mentioned above all the meteorological parameters, including air temperature, barometric pressure, humidity, precipitation, etc. were measured at each of the sites. At the sites with a tower, these parameters were also often measured at various heights. For an optimal atmospheric profile for the correction of the LANDSAT ETM+ dataset, radiosonde measurements from MeteoSwiss were also acquired. In the Sperrstrasse-canyon, a broad set of infrared radiation thermometers (IRT) were additionally placed, facing walls, floor (Everest infrared thermometer 4000A) and roofs (Heimann infrared thermometer KT-15) during the IOP (see also Doerksen, 2004) along with a manually operated AGEMA thermovision 900 SW-TE facing the north wall of the canyon, which was only used at specific times.

For the modelling of solar irradiation a digital elevation model (DEM) of 25m pixel resolution was acquired form Swisstopo.

From the "Grundbuch- und Vermessungsamt Basel-Stadt" a digital city elevation model (DCEM) (see Figure 4.4) with 1m pixel resolution was provided for the high resolution modelling of the solar irradiation. This dataset was further used for the calculation of the sky view factor and the complete aspect ratio, which was necessary to calculate the storage heat flux density.

As illustrated in Figure 4.4, the buildings are quite similar in height, few of them rising significantly above the average of 18m. As exceptions, the buildings of the Messe (Exhibition) in the eastern part are considerably higher than their surrounding area, as can be noted for the mediaeval part of the city, in the centre of Figure 4.4, extending to the southern bank of the River Rhine. In contrast, the residential buildings in the south-western area have a lower average height.

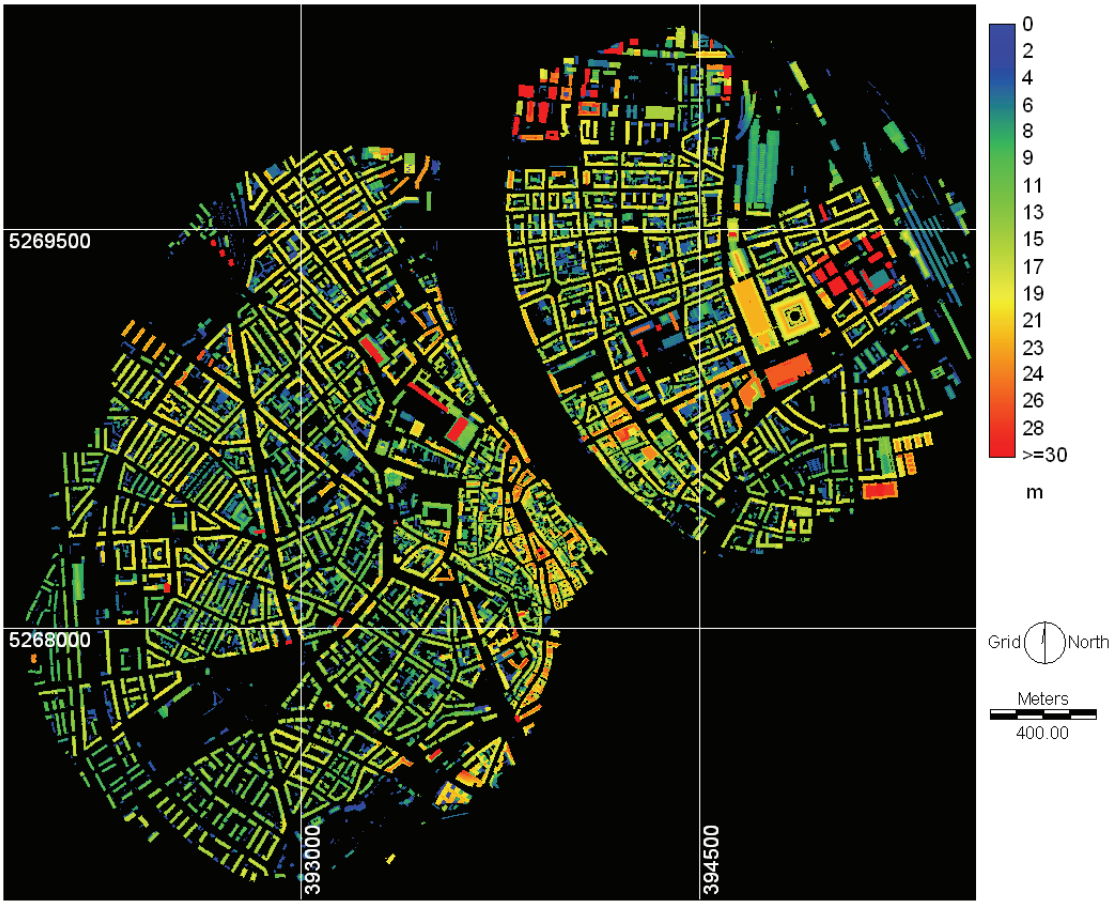

Fig. 4.4: The DCEM of the downtown area of Basel with the heights of the buildings in meters.

5. Methods

5.1 Remote sensing data (pre-) processing

5.1.1 AVHRR-Data

A total of 42 AVHRR scenes from different days with fair weather conditions during the BUBBLE IOP (16 scenes) and from 2003 (26 scenes) (see Appendix B) were acquired from the University of Berne, Switzerland. The high-resolution picture transmission (HRPT) data are ingested by a receiving station located in Berne (46°55' 42"N / 7°28' 41"E). The AVHRR-data were processed by D.Oesch from the University of Berne. A short description of the processing method is given below, with further information available in Oesch (2005).

The use of NDVI for emissivity estimation required an accurate pre-processing of AVHRR channels 1 and 2, according to the NOAA KLM User's Guide (Goodrum et al., 1998). The radiative transfer code used for atmospheric correction of the top of the atmosphere reflectance was the updated SMAC (Rahman & Dedieu, 1994) algorithm. The data were cloud screened using the Cloud and Surface Parameter Retrieval (CASPR) (Key, 2002). For the visible channels, terrain normalization and Bidirectional Reflectance Distribution Function (BRDF) correction (according to Wu et al. (1995)) were applied to the images. The resulting datasets are subset to the WGS84 ellipsoid latitude - longitude grid. Atmospheric effects were corrected using an appropriate Split - Window Technique (SWT) algorithm. Most SWT's currently in use are heavily dependent on emissivity, which ranges between 0 and 1 (water). Vegetation usually produces values between 0.97 and 0.98, whereas those of bare soil are often lower than 0.95. An inaccuracy of 1% in emissivity estimation can cause an error of up to 0.78 K in LST (van de Griend and Owe, 1993). Therefore, the used actual emissivity values were derived from the atmospherically and BRDF corrected NDVI, as described by Valor and Caselles (1996). A detailed discussion about the importance and difficulties with the emissivity ε for remotely sensed data can be found in Dash et al. (2002). The result is an approximation that relates emissivity values to the NDVI of a given surface and explains the experimental behaviour observed by Van de Griend and Owe (1993): It was found that thermal emissivity correlated strongly with NDVI after logarithmic transformation.

Tab. 5.1: Split window equations used in intercomparison (T4 and T5 are the brightness temperature values of AVHRR channels 4 and 5 and ε4 and ε5 are their respective emissivities)

Authors	Split-window equations
Price, 1984 (for AVHRR 7)	$[T_4 + 3.33\ (T_4 - T_5)\ ]\ [(5.5 - \varepsilon_4) / 4.5] + 0.75\ T_5\ (\varepsilon_4 - \varepsilon_5)$
Becker & Li, 1990 (for AVHRR 9)	$1.274\ [3.63 + 2.068\ ((1-\varepsilon) / \varepsilon) + 18.924\ ((\varepsilon_4 - \varepsilon_5) / \varepsilon^2)]\ T_4 + [-2.63 - 1.912\ ((1-\varepsilon) / \varepsilon) - 19.406\ ((\varepsilon_4 - \varepsilon_5) / \varepsilon^2)]\ T_5$
Prata & Platt, 1991 (for AVHRR 11)	$[3.45\ (T_4 - T_0) / \varepsilon_4\ ] - [2.45(\ T_5 - T_0) / \varepsilon_5\ ] + 40\ [(1 - \varepsilon_4\ ) / (\varepsilon_4\ )] + T_0$
Ulivieri et al., 1992 (for AVHRR 7)	$T_4 + 1.8\ (T_4 - T_5) + 48\ (1 - \varepsilon) - 75\ (\varepsilon_4 - \varepsilon_5)$
Sobrino et al., 1993 (for AVHRR 11)	$T_4 + 1.06\ (T_4 - T_5) + 0.46\ (T_4 - T_5)^2 + 53\ (1 - \varepsilon_4) - 53\ (\varepsilon_4 - \varepsilon_5)$
Sobrino et al., 1994 (for AVHRR 11)	$T_4 + 2.76\ (T_4 - T_5) + 38.6\ (1 - \varepsilon) - 96\ (\varepsilon_4 - \varepsilon_5)$

The data were then processed with the following six SWT-algorithms (see Table 5.1) to determine which was best suited to urban surfaces. As described by Czajkowski et al. (1998), one has to keep in mind that most of the LST algorithms are only valid for a specific satellite and/or a specific set of surface or geographical conditions. The variations of the sensor filter functions were not taken into account in this study, so a somewhat higher error has to be expected for some of the SWT algorithms.

For example, for the equation of Becker & Li (1990), designed for use with data from the AVHRR instrument on NOAA 9, Czajkowski et al. (1998) found errors up to 2.3 K if it was applied to other AVHRR sensors.

5.1.2 MODIS Data

A total of 26 MODIS scenes were acquired during the BUBBLE-IOP – 13 in 2002 and 13 more in 2003 – via the Earth Observing System Data Gateway of the NASA Land Processes Distributed Active Archive Center (LP DAAC). They were then reprojected, using the "MODIS reprojection tool" (MRT), to UTM Zone 32N and ellipsoid WGS-84 (see also http://lpdaac.usgs.gov/datatools.asp for further information).

The datasets used for the retrieval of the longwave upward radiation values are MOD11A1 (TERRA) and MYD11A1 (AQUA), which are classified as "MODIS/Terra Land Surface Temperature/Emissivity Daily L3 Global 1 km ISIN Grid" level 2 products.

The MODIS Land Surface Temperature and Emissivity (LST/E) products provide per-pixel temperature and emissivity values. Temperatures are extracted in degrees Kelvin with a view-angle dependent algorithm applied to direct observations. The view angle information is included in each LST/E product. Emissivities are estimates derived by applying algorithm output to land cover database information. The LST/E algorithms use MODIS data as input, including geolocation, radiance, cloud masking, atmospheric temperature, water vapor, snow, and land cover. Results on LST by Petitcolin & Vermote (2002) and Wan et al. (2002) show that MODIS data have an accuracy of approximately 1 K when compared to ground based measurements in homogeneous rural regions with known emissivity (see also Wan & Li, 1997). Due to this preprocessing and because all MODIS data are cloud screened, the longwave surface radiation flux density can easily be calculated using Stefan-Boltzmann's law, as shown in eq.3.2.

For the assessment of the NDVI also, the MOD13A2 (TERRA) and MYD13A2 (AQUA) datasets, designated as "Vegetation indices 16-Day L3 Global 1km" were acquired from the source noted above. As input, this MODIS product uses MODIS surface reflectances, corrected for molecular scattering, ozone absorption, and aerosols, and adjusted for nadir and standard sun angles using BRDF models. Two vegetation index (VI) algorithms are produced globally for land. One is the standard normalized difference vegetation index (NDVI), also known as the "continuity index" to the existing NOAA-AVHRR derived NDVI. The other is an "enhanced" vegetation index (EVI) with improved sensitivity into high biomass regions. The gridded vegetation indices will include quality assurance flags with statistical data indicating the quality of the VI product and input data.

All the MODIS datasets used were validated products of version V003.

.

5.1.3 LANDSAT ETM+ Data

A LANDSAT ETM+ image from July 8, 2002 was acquired and georeferenced to UTM WGS-84 with an RMSE of less than 1 pixel. The time of satellite overpass was 10:11 UTC. The radiance and surface temperature were calculated using the following equations:

To obtain the spectral radiance L [W/m^2 sr µm] from the digital data DN

$$L = gain * DN + offset \qquad (5.1)$$

where gain [W/m^2 sr µm] and offset [W/m^2 sr µm] are calibration values, which can be obtained from the data header.

The radiation temperature at the sensor (T [K]) can be calculated using the following equation (Schott & Volchok (1985):

$$T = \frac{K2}{\ln(\frac{K1}{L} + 1)} \qquad (5.2)$$

where K1 and K2 are pre-flight calibration constants

K1 = 666.093 W/m^2 sr µm

K2 = 1282.7108 K

Afterwards the data were corrected for atmospheric influences with the WINDOW-model which is based on Price (1983) with a radiosonde atmospheric profile available from Payerne/Switzerland (MeteoSwiss©) and a digital elevation model of 25 m resolution as model input. After the atmospheric correction we obtained the surface radiant temperature T_s. The emissivity values for the WINDOW-model were given through a maximum likelihood land use classification (see Dash et al., 2002; Snyder et al., 1998) for which average values from literature were applied (Oke, 1987; Snyder et al., 1998; Valor & Caselles, 1996) (see also Figure 5.9). A detailed discussion about the importance and difficulties with the emissivity ε for remotely sensed data from different sensors can be found in Dash et al. (2002).

5.1.4 ASTER Data

For the ASTER data, the following on-demand datasets were acquired through the Earth Observing System Data Gateway of the NASA Land Processes Distributed Active Archive Center (LP DAAC). Due to the fact that ASTER only became operational in 2000, few publications have yet focused on urban climate or land surface temperature (LST) retrieval or urban applications (French et al., 2005; Jacob et al., 2004; Kato & Yamaguchi, 2005; Liang, 2001). All of the ASTER data feature quality flags for each pixel and are already atmospheric corrected using the methods described below. For more detailed information about the processing of ASTER data, the ASTER Algorithm Technical Basis Document (ATBD) can be obtained from the Japanese ASTER homepage

(http://www.science.aster.ersdac.or.jp/en/documnts/atbd.html). The following ASTER datasets were obtained and used:

a) AST-05 ASTER On-Demand L2 surface emissivity

This ASTER product is atmospherically corrected. The surface-leaving radiance is of known accuracy and valid only for clear-sky scenes (cloud-free pixels).

The algorithm to correct atmospheric effects involves two elements: 1) It uses a radiative transfer model capable of estimating the magnitude of atmospheric emission, absorption, and scattering. This uses the MODTRAN radiative transfer model, which calculates atmospheric transmittance and radiance for frequencies from 0 to 50,000 cm^{-1} at moderate spectral resolution. 2) It identifies and incorporates all the necessary atmospheric parameters applicable to the location and time for which the measurements require correction. These include temperature, water vapor, elevation, ozone, and aerosols.

b) AST-07 ASTER On-Demand L2 surface reflectance VNIR

For the calculation of the NDVI the ASTER On-Demand L2 Surface Reflectance (VNIR) was obtained. This is a higher-level product that contains atmospherically corrected visible and near-infra red data. It is generated using the three VNIR bands (between 0.52 and 0.86 μm) from an ASTER Level-1B image. Atmospheric correction involves deriving a relationship between the surface radiance/reflectance and the top of the atmosphere (TOA) radiance from information on the scattering and absorption characteristics of the atmosphere. Once this relationship is established, it is used to convert ASTER VNIR's original radiance values to atmospherically corrected surface radiance and reflectance values. The atmospheric correction algorithm for VNIR is based on a Look-Up Table (LUT) approach that uses results from a Gauss-Seidel iteration of the Radiative Transfer Code (RTC). The algorithm is based on the relationship between the angular distribution of radiance, scattering and absorption in the atmosphere, and the surface properties. The RTC used to generate the LUT for the atmospheric correction is based on:

- solar zenith angle,
- satellite view angle,
- relative azimuth angle between the satellite and sun,
- molecular scattering optical depth,
- aerosol scattering optical depth,
- aerosol scatter albedo,
- aerosol size distribution parameter, and
- surface reflectance.

The size distributions for aerosol are based on either a Junge size distribution or the set of aerosol types used in the atmospheric correction of Multi-angle Imaging Spectroradiometer (MISR) data. The initial versions of the algorithm rely on external climatological sources for information on atmospheric absorption and scattering parameters. In due course, this information is likely to come from other Terra sensors such as MISR and the MODIS. A digital elevation model provides the slope and elevation information for accurate modelling of surface reflectance.

c) AST-08 ASTER On-Demand L2 kinetic surface temperature

This ASTER product is derived using the same algorithm as the surface emissivity product. Surface kinetic temperature is determined by applying Planck's Law, using the emissivity values from the Temperature-Emissivity Separation (TES) algorithm, which uses atmospherically corrected ASTER Surface Radiance (TIR) data (see Gillespie et al., 1998; Payan & Royer, 2004). The TES algorithm first estimates emissivities in the TIR channels using the Normalized Emissivity Method (NEM). These estimates are used in combination with Kirchoff's Law to account for the land-leaving TIR radiance that is due to sky irradiance. That figure is subtracted from TIR radiance iteratively to estimate the emitted radiance, from which temperature is calculated using the NEM module.

All the six available ASTER overpasses covering the research area (from 2000 to 2005, see Appendix B) were manually geocoded to the relevant coordinate system (UTM Zone 32N, WGS-84).

The calculation of the broadband albedo α was done with the formula provided by Liang (2004), Liang et al. (2003) and Liang (2001) with the AST-07 datasets (see Figure 5.2)

$$\alpha = 0.484*b_1 + 0.335*b_3 - 0.324*b_5 + 0.551*b_6 + 0.305*b_8 - 0.367*b_9 \qquad (5.3)$$

where $b_{1,3,5,8,9}$ are the respective ASTER bands.

For the calculation of the longwave upward radiation, eq. 3.1 was used, together with AST-08 data and the broadband emissivity value, which was calculated from the AST-05 product using the following formula (Gieske et al. 2003; Ogawa et al. 2002; Zhou et al. 2003)

$$\varepsilon = 0.035 * b_{10} + 0.072 * b_{11} + 0.118 * b_{12} + 0.381 * b_{14} + 0.380 \qquad (5.4)$$

where $b_{10,11,12,14}$ are the respective ASTER-bands.

After the validation of the datasets, the further research in this paper focuses mainly on an ASTER-overpass August 5, 2003. The other five scenes covering the City of Basel between 2000 and 2005 were analysed only for validation of the longwave upward radiation.

5.2 The Normalized Difference Vegetation Index (NDVI)

As a basic for vegetation assessment, the **N**ormalize **D**ifference **V**egetation **I**ndex (NDVI) was first developed by Tucker (1979) and is commonly used with remote sensing data (e.g. Stefanov & Netzband, 2005; Steven et al., 2003; Wilson et al. 2003). The NDVI takes advantage of the higher reflectance of chlorophyll in the leaves of plants in the near-IR (around 800nm) range, compared with land without vegetation cover. This abrupt change in reflectance is also called the "red edge". The NDVI is a dimensionless unit ranging theoretically between -1 and +1 and can be calculated using the following equation:

$$NDVI = \frac{IR - R}{IR + R} \qquad (5.5)$$

IR is the respective near infrared and R the respective red band of the specific satellite.

High values (above 0.3) indicate much vegetation, whereas values between 0.1 and 0.3 indicate partly vegetation cover or unhealthy plants. Values below 0.1, including negative values, indicate impervious surfaces without vegetation. The lowest values can be always found over water areas (see Figure 5.1).

Several vegetation indices have become available these days including the Leaf Area Index (LAI) (see Chen et al., 1997) which is mostly used on forest or agricultural areas and is therefore not very suited for urban areas. Another one is the Soil Adjusted Vegetation Index (SAVI) (Huete, 1988) which takes the surface soil parameters more into account. The NDVI was found finally the most commonly used without further parameters needed and has the longest history of use, and was therefore considered the moist suitable for this project. Also the NDVI is the most commonly used vegetation index in urban areas as well for different purposes (Lo & Faber, 1997; Nichol & Wong, 2005; Stow & Chen, 2002; Small, 2001; Zha et al., 2003)

The NDVI values of different satellite sensors are very similar according to Gallo et al. (2005) and Steven et al. (2003). It has been also shown many times that there is a strong correlation between surface radiant temperature and the NDVI in satellite or airborne images (Boegh et al., 1998; Gallo & Owen, 1999; Quattrochi & Ridd, 1998; Rigo, 2001; Weng et al., 2004) especially over rural areas. Because the NDVI changes during the seasons as the vegetation does (see Rigo, 2001) it is necessary to obtain actual NDVI data from the different satellite sensors. The NDVI also allows the possibility of using the AVHRR to estimate the emissivity of different surfaces (Valor & Caselles, 1996) which is also an important input parameter for the calculation of the surface temperature and longwave upward radiation.

The NDVI was necessary for the modelling of the ground (or storage) heat flux density and for the calculation of the Bowen-Ratio (see chapter 5.5.2 and 5.6 respectively). An example of the NDVI distribution in the research area is shown in Figure 5.1 where there is a clear distinction between rural (green), suburban (yellow) and urban (brown) surfaces.

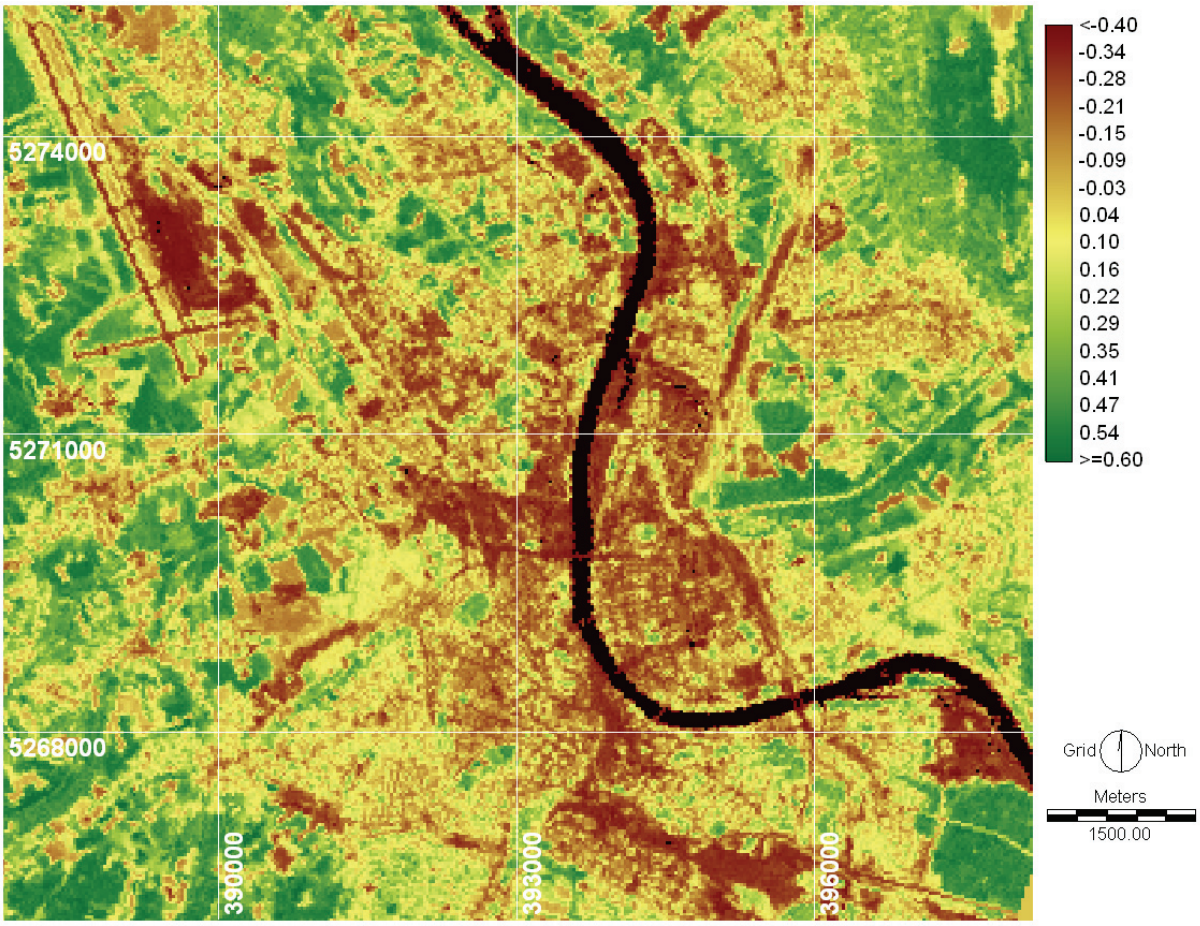

Fig. 5.1: NDVI from the LANDSAT EMT+ scene from July 8, 2002

5.3 The short wave irradiance model (SWIM)

For the modelling of the net radiation Q* the shortwave downward radiation Q_{SD} value is necessary. This was calculated using the Shortwave Irradiance Model (SWIM) (Parlow, 1996b) for the time of the satellite overpasses with a digital elevation model (DEM) providing input parameters for height, slope and aspect. The necessary percentage values for diffuse and direct net radiation were obtained from *in situ* measurements. One further input parameter needed is the geolocation of the scene according to the UTM grid. Figure 5.2 provides an example of a SWIM model of shortwave downward radiation. This shows the influence of the topography on Q_{SD} and also the placement of the topographic features in the research area.

The 25 m DEM was used with SWIM for the modelling of Q_{SD} and was aggregated to a 30 m value using a nearest neighbour method to suit the resolution of the satellite data. In Figure 5.2 it shows an average value of 830 Wm^{-2} for flat areas, which corresponds well with Figure 3.2.

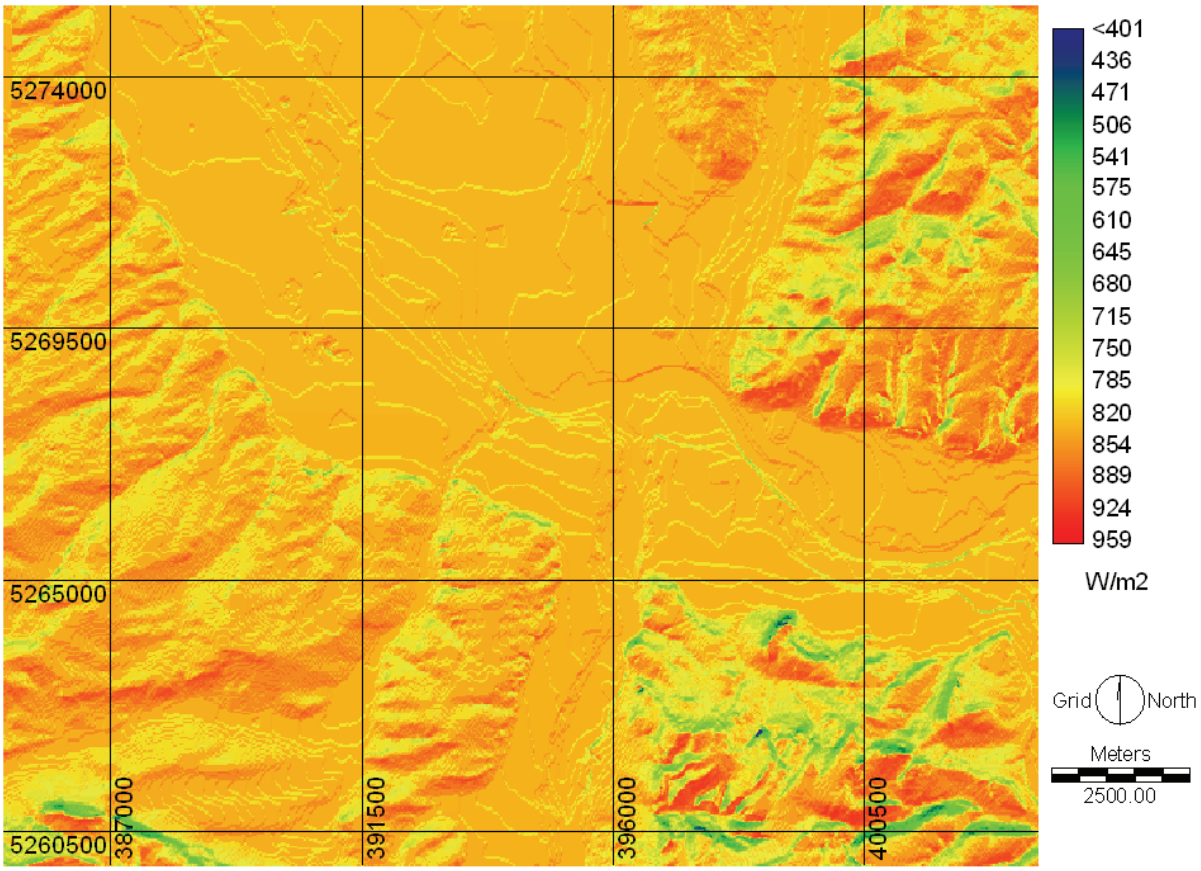

Fig. 5.2: SWIM modelled Q_{SD} (in Wm^{-2}) for July 8, 2002 at 11 a.m. CET with UTM-Grid

SWIM also offers the possibility to calculate a horizon limitation from a DEM. It takes the nearest pixel in each direction from every point, according to the number of segments (e.g., every 10 degrees), which inhibits it line of sight. SWIM was used to simulate the shadowing effects of the buildings with the digital city elevation model (DCEM).

The calculation of the incoming Q_{SD} aggregated over an entire day is also possible with SWIM: July 8, 2002, the model showed an average result of 23.6 MJ m^{-2} day^{-1}. Measurements during the whole IOP report an average daily value between 22.6 and 22.9 MJ m^{-2} day^{-1}, which make the SWIM estimate for a clear sky day quite accurate.

5.4 Modelling the net radiation Q*

5.4.1 Satellite data Q*

Modelling of the heat flux densities requires the input parameter of the net all wave radiation.

The processing flowchart of the modelling of the net all wave radiation Q* value is shown in Figure 5.3 below. As basis datasets, the radiosonde measurements, the visible and near infrared data (VIS/NIR), a digital elevation model (DEM) and the thermal infrared datasets were used.

The computation of net radiation was performed in single steps. First, the solar irradiance (Q_{SD}) (shortwave downward radiation) was modelled with SWIM, using a digital elevation model (DEM) as input data. Model runs were computed for all dates and time slots of satellite overpasses.

The longwave upward radiation (Q_{LU}) was calculated from the thermal infrared channels of the various satellite platforms used, after correcting for atmospheric influences.

The broadband albedo α, which allows the calculation of the shortwave upward radiation (Q_{SU}), was derived using a linear regression between *in situ* measurements and a synthetic panchromatic channel computed for the visible and near infrared channels of LANDSAT ETM+, according to Parlow (1996 a), and for ASTER according to eq. 5.3 (see Figure 5.4). The broadband albedo is better suited for the calculation of Q_{SU} than the plain shortwave reflectance would be, because it also takes into account several of the surface characteristics of urban surfaces.

Since longwave downward radiation (Q_{LD}) is very uniform and shows only differences in the degree of instrument accuracy between rural and urban sites (Christen, 2005) it was assumed to be the average of all *in situ* measurements at the time of the corresponding satellite overpass. From these data the spatially distributed all net radiation (Q*) was calculated according to eq. 3.7.

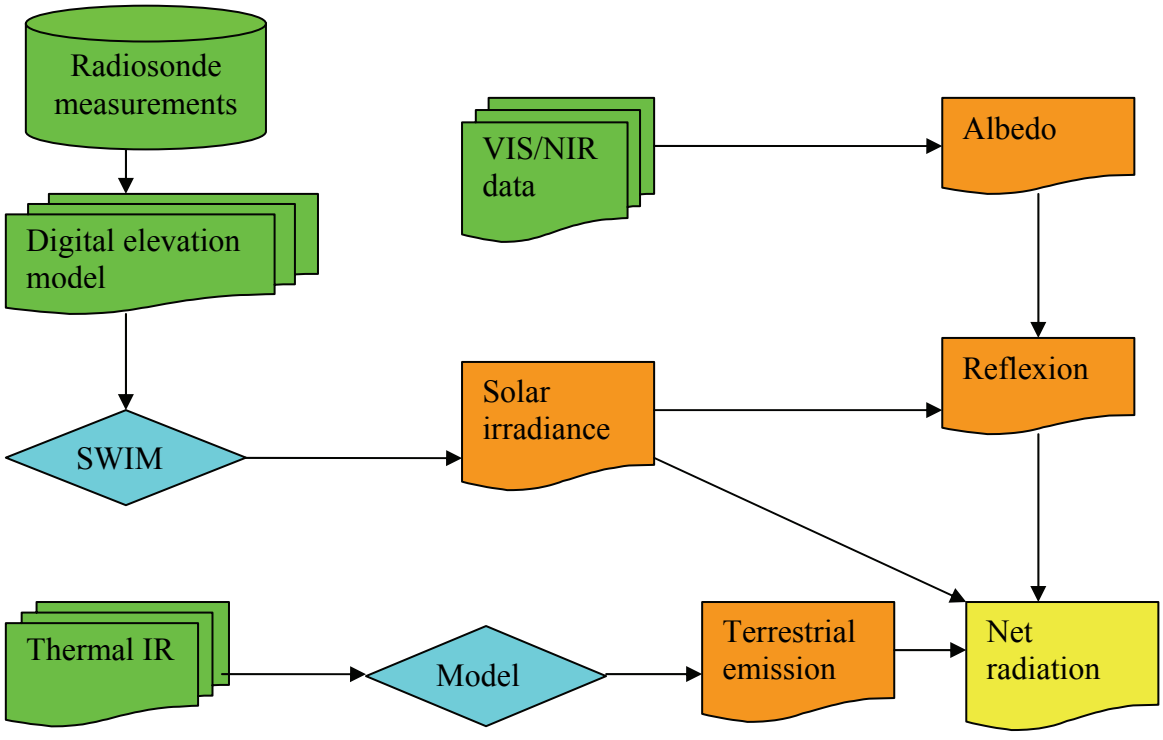

Fig. 5.3: Flowchart of the computation and modelling of the net radiation from satellite data

Most models applied by other researchers to remote sensing data in order to model Q* (French et al., 2005; Ma, 2003) have been validated and used over rural surfaces. Therefore, the current step by step approach with SWIM was developed to enable validation of the Q_{LU} (and the LST) over the urban (and rural) surface in advance, and to calculate each member of the radiation balance (eq.3.7) individually from satellite data (except Q_{LD}).

Figure 5.4 below shows the albedo calculated from ASTER according to eq.5.3. The city clearly shows a lower albedo (around 10%) than the surrounding rural areas (about 16%). The highest albedo can be found at the rural sites (values over 25%), in the industrial areas and at the airport. As a water area, the River Rhine shows the lowest albedo. The distribution of the albedo in Figure 5.4 is therefore fully compliant with the findings of Christen & Vogt (2004).

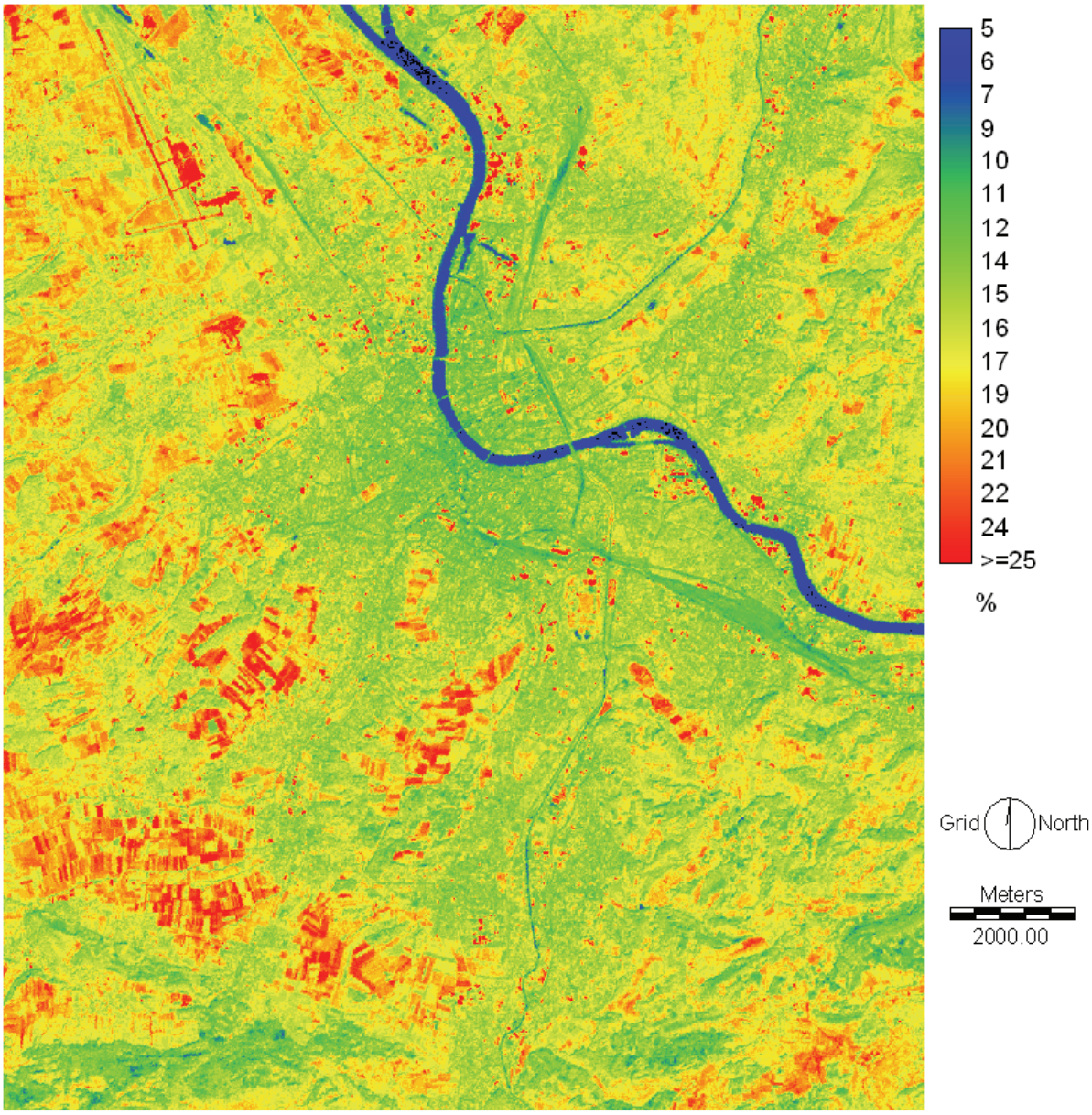

Fig. 5.4: Albedo (in percent) calculated for the ASTER overflight of August 5, 2003, 10:30 UTC

5.4.2 Very high resolution data Q*

The very high resolution datasets were also processed as described in the preceding subchapters. Due to the high resolution of the respective images and the seasonal difference between the Quickbird image and the VarioCam data, the difference of albedo is the most significant value derived from these datasets.

For this purpose, considering the extremely limited availability of high resolution satellite data such as Quickbird or Ikonos, data from various times and satellite systems were used.

The longwave downward radiation Q_{LD} value was taken as an average of the *in situ* values of the three regular *in situ* sites in use when the VarioCam data were acquired in 2004. Due to the limited availability of data, the longwave upward radiation was calculated from the VarioCam data with Stephan-Boltzmann's law, with an emissivity value of 0.98 for the entire area. The shortwave downward radiation was modelled with SWIM on the 1m DCEM, and a horizon limitation was applied to take into account the shadow effects of the buildings. Using the panchromatic Quickbird image, the albedo was calculated based on a regression approach between values measured *in situ*, those supplied in literature (e.g., water areas) and the DN numbers of the panchromatic image. With all the components of the net radiation in place, the Q* value was computed.

5.5 Modelling the ground heat flux density ΔQ_S

Whether a surface is urban or rural, its net radiation value is a basic requirement to determine the area's ground heat flux densities. As the sum of all incoming and outgoing radiation flux densities, net radiation is the key determiner of amount of energy available for heat flux densities. If net radiation is positive, as is generally the case during daytime, energy can be transferred into the turbulent heat flux densities (sensible and latent) and into the ground heat flux density. If net radiation is negative, as it usually is during the night, it has to be compensated for by the heat flux densities. The net radiation equation can be written as shown in eq. 3.7, which allows the heat flux balance to be described by equation 3.9. The anthropogenic heat flux density Q_F is very small in European cities such as Basel, ranging between 5 W m^{-2} in suburban areas and 20 W m^{-2} for the city centre (Christen & Vogt, 2004). For this analysis the anthropogenic heat flux density is therefore not given special consideration.

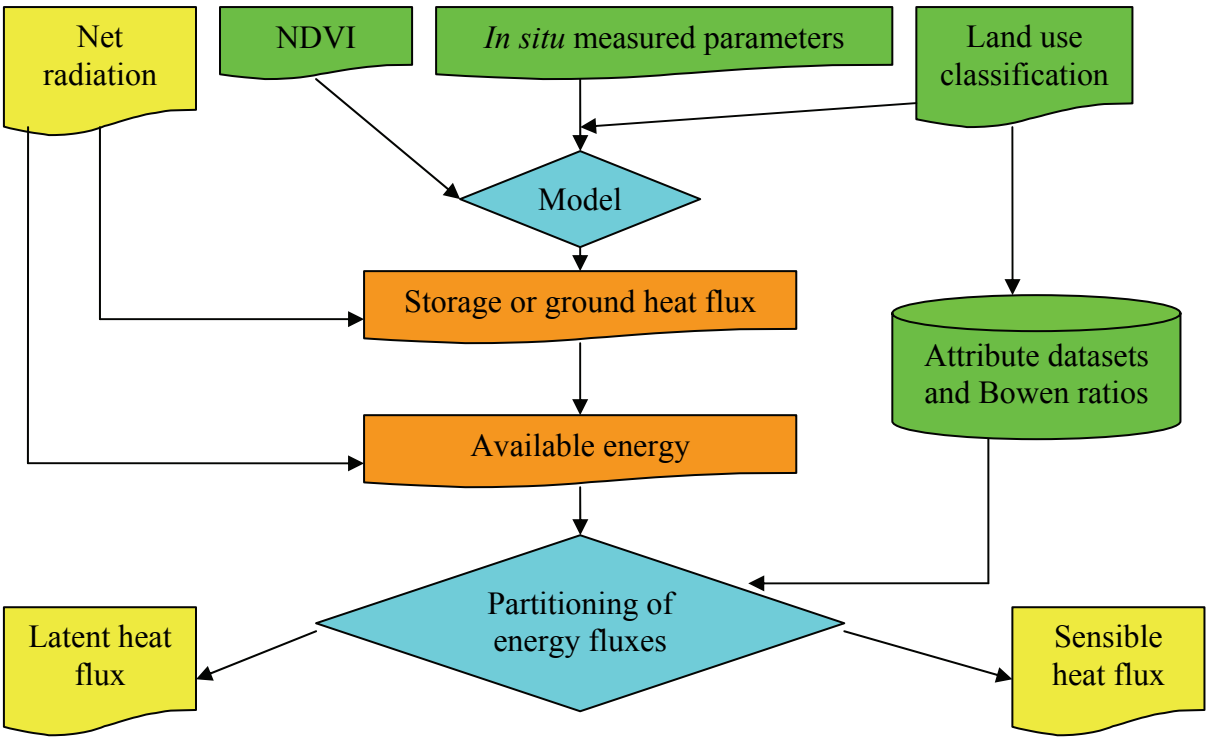

Fig. 5.5: Flowchart of the modelling of the heat flux densities

After determining net radiation, the next step, as shown in Figure 5.5, was to model the ground (or storage) heat flux density. For this step the input parameters for the model are the land use classification, the NDVI, the net radiation as well as several data derived *in situ*.

For the calculation of the ground heat flux density ΔQ_S, three approaches were used and compared with one-hour averaged *in situ* ΔQ_S measurements for each of the different sites. To determine which approach was best suited and most accurate for the modelling of ΔQ_S, as well as to apply the Objective Hysteresis Model (OHM) of Grimmond and Oke (1999), for the first time to remotely sensed data, the results were then compared.

The parameters used in the equations below were derived from all-time-IOP measurements. The validation of the data was conducted using hourly clear-sky days averages from the IOP.

5.5.1 The complete aspect ratio approach

This approach is based on the calculation of the complete aspect ratio (CAR). The complete aspect ratio λ_C describes the enlargement of the surface due to the 3-D structure of the city, which almost doubles the surface for the storage heat flux density. It can be derived from a high resolution (1m) digital city surface model which provides information on building height, roof structure etc. As a first step the sky-view-factor was calculated from the surface model (see Figure 5.6).

Next, the complete aspect ratio (λ_C) was computed. For a more general overview and better comparison with other methods and *in situ* readings, data were then downsampled to 30 m resolution.

As mentioned by Christen and Vogt (2004), there is a correlation between λ_C and $\Delta Q_S/Q^*$ that can be described as a hysteresis, suggesting the following relationship:

$$\Delta Q_S / Q^*_{(\lambda_C)} = \frac{(\Delta Q_S / Q^*_{rural}) - (\Delta Q_S / Q^*_{\max})}{\lambda_C + \lambda_C f - f} + \Delta Q_S / Q^*_{\max} \qquad (5.6)$$

Fig. 5.6: Calculated sky view factor from the DCEM

Where $\Delta Q_S/Q^*_{rural}$ is the ratio measured or modelled over rural surfaces, $\Delta Q_S/Q^*_{max}$ is the theoretical value asymptotically reached with increasing λ_C. It is set to a constant value of -0.45 (oral communication A. Christen). During the day $\Delta Q_S/Q^*_{rural}$ changes and reaches the average value of -0.56 at nighttime (22h to 4h CET) while at daytime (11h to 15h CET) it is only -0.12 (Christen and

Vogt, 2004). An example for the relationship between $\Delta Q_S/Q^*$ and λ_C calculated from the BUBBLE all-times IOP *in situ* measured values is shown in Figure 5.7.

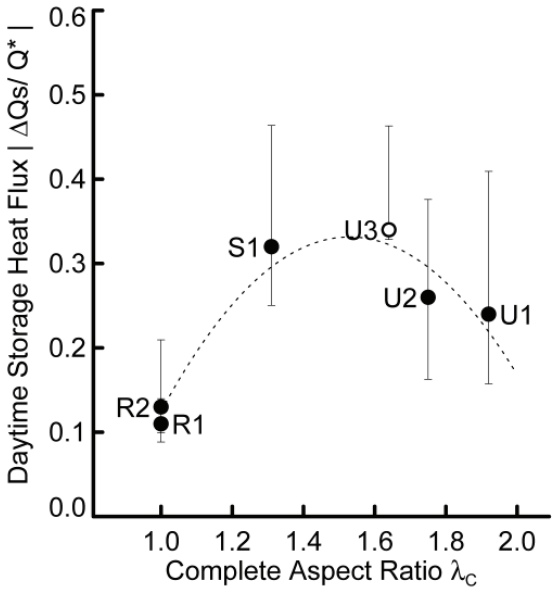

Fig. 5.7: Intensity of the daytime storage heat flux density compared to net radiation ratio ($\Delta Q_S/Q^*$) depending on the complete aspect ratio λ_C of the surface. The data used were taken from the IOP period from June 10 to July 10 2002. Error bars include 50% of all single 1-hour runs.

The factor *f* is used to describe the value curve that is highly dependent on daytime, due to the diurnal hysteresis. It is set to values between 10 (morning) and 0 (evening) to fit the observations. Since the LANDSAT ETM+ overpass was between 10 and 11 a.m. UTC, *f* was set to a value of 5 for the best possible fit according to the *in situ* derived values. It is important to note that values for the parameter *f* were derived from the *in situ* sites as averages during the entire IOP and do not reflect values from July 8, 2002 alone. Small changes between values of *f* from 4.5 to 5.5 result in differences in ΔQ_S in the range of ± 5 Wm^{-2}. The application of the factor to the remotely sensed data to model the ground heat flux density ΔQ_S is independent from *in situ* data: the complete aspect ratio λ_C was calculated without *in situ* data from the DCEM dataset and was only validated using the *in situ* data.

5.5.2 The NDVI approach

This approach is based on the assumption that vegetation reduces the ground heat flux density: with increasing biomass, then, ground heat flux density must decrease. The Normalized Difference Vegetation Index (NDVI) can be treated as an indicator of biomass density. Kustas & Daughtry (1990) documented a linear relationship between the Q_S/Q^* ratio and the NDVI. In the Surface Energy Balance Algorithm for Land (SEBAL) (Bastiaanssen et al., 1997) the NDVI was selected to describe the general effect of vegetation on surface heat flux densities. More detailed descriptions can be found in Kustas & Daughtry (1990) and Bastiaanssen et al. (1997).

Since the equations by Bastiaanssen et al. (1997) are based on rural field measurements, they are not particularly suitable for urban areas. Parlow (2000) proposed the following modified equations for urban and rural environments:

$$\Delta Q_{S\,(urban)} = -(0.3673 - 0.3914 \bullet NDVI) \bullet Q^* \quad (5.7)$$

$$\Delta Q_{S\,(rural)} = (0.3673\text{-}0.3914 \bullet NDVI) \bullet Q_S^* \bullet (-0.8826 \bullet \ln(Q_S^*) + 5.0967) \quad (5.8)$$

Where Q^* is the net radiation, NDVI the Normalized Difference Vegetation Index and Q_S^* the shortwave net radiation ($Q_{SD} - Q_{SU}$).

The NDVI can be calculated from the full set of daytime satellite images for all the LANDSAT ETM+ and ASTER images. For MODIS the 16-day average NDVI can be obtained as described in Chapter 4. The total net radiation (Q*) and shortwave net radiation have been computed as described above and an accuracy assessment conducted before further processing. For the urban sites, eq. 5.7 was used while eq. 5.8 was used for the rural ones.

5.5.3 The objective hysteresis model approach

The Objective Hysteresis Model (OHM) was introduced by Oke & Cleugh (1987) and Grimmond & Oke (1999) for field measurements. In this thesis it was applied for the first time to remotely sensed data over an urban area. Oke & Cleugh (1987) used a hysteresis-type equation to characterize the ground heat flux density as

$$\Delta Q_S = a_1 Q^* + a_2 \frac{\partial Q^*}{\partial t} + a_3 \quad (5.9)$$

where t is time [h] and the parameter a_1 indicates the overall strength of the dependence of the ground heat flux density on net radiation. The parameter a_2 describes the degree and the direction of the phase relations between ΔQ_S and Q^*. The parameter a_3 is an intercept term that indicates the relative timing when ΔQ_S and Q^* turn negative. The hysteresis curve is shown in Fig. 5.8 for the measurement sites as calculated by Christen et al. (2003) for the BUBBLE sites from *in situ* data.

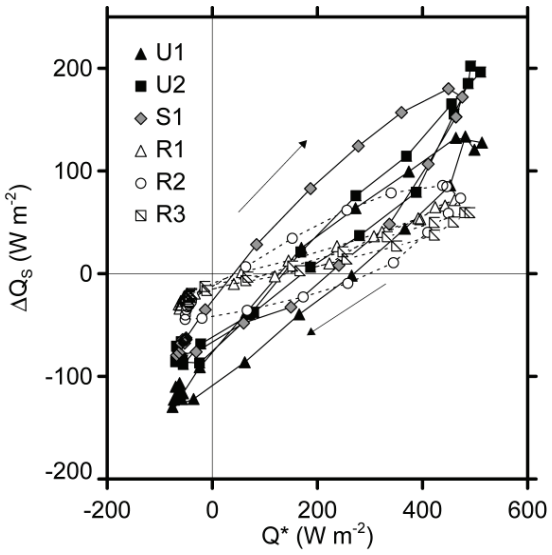

Fig. 5.8: Mean diurnal hysteresis of the ground or storage heat flux density ΔQ_S vs. the net radiation Q* at the rural and urban sites (after Christen et al. (2003)).

The parameters a_1, a_2 and a_3 can be derived from *in situ* measurements for the specific land use class of each site as averages (Christen & Vogt, 2004) during the entire IOP at the specific sites and are not values from July 8, 2002 alone. The parameters were calculated for each site from the *in situ* measurements during the IOP. For the land use class "Forest" the values were taken from Grimmond & Oke (1999) because no BUBBLE sites were located in a forest.

The parameters and a_1, a_2 and a_3 were also used without specific fitting to the remotely sensed datasets. The same is true for the net all wave radiation data (Q*) where only Q_{LD} was derived from *in situ* data.

Tab. 5.2: The OHM parameters used for the different land use classes calculated from the all times IOP *in situ* data.

Parameters/Land use class	a_1	a_2	a_3
Forest (Grimmond & Oke 1999)	-0.11	-0.11	12.3
Industrial and dense built-up areas (U3)	-0.46	-0.16	49
Medium and sparse built-up areas (ø S1 + U1 + U2)	-0.42	-0.27	36
Agricultural (R2)	-0.21	-0.34	25
Grassland (ø R1 + R3)	-0.16	-0.05	16

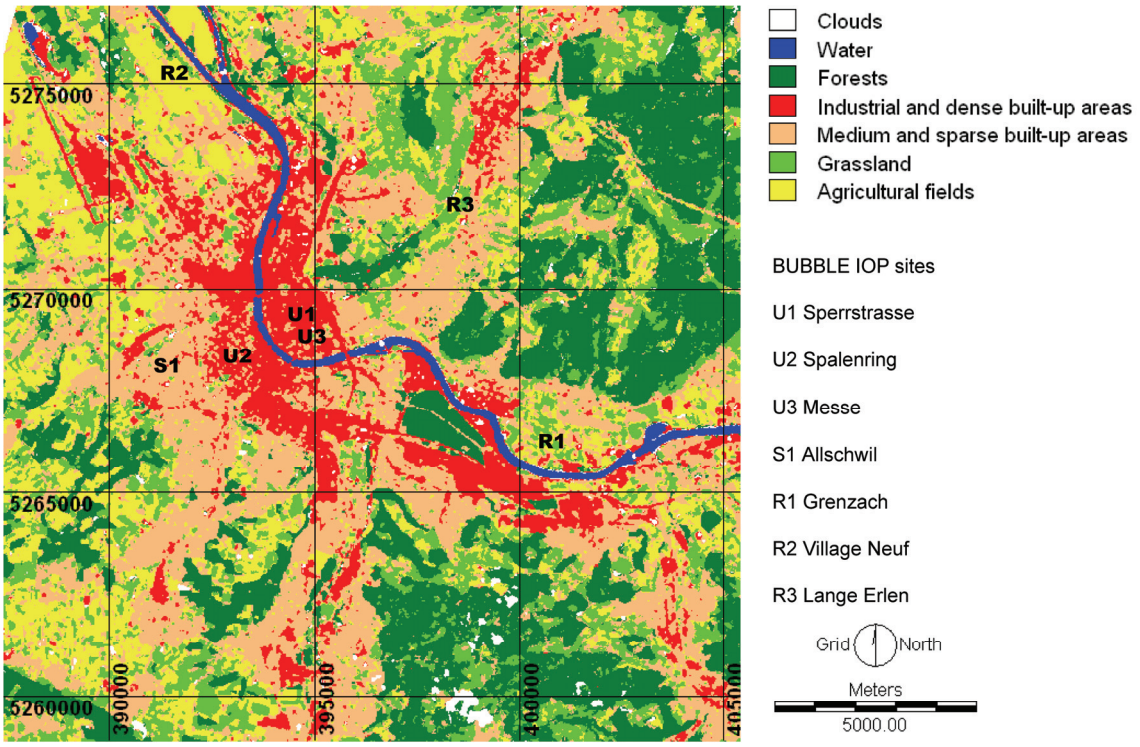

Fig. 5.9: Land use classification (LUC) from a fused LANDSAT ETM+ - ASTER imagery from the 12.06.2001 used with the OHM approach together with the location of the *in situ* sites

The land use classes were calculated from an LANDSAT ETM+ and ASTER fused image from June 12, 2001 (as shown in Figure 5.9) with a maximum likelihood approach. The accuracy of the land use classification was 81.2% with a Kappa coefficient of 0.80. The data from 2001 were used because of their better spatial coverage and because the fused ASTER-LANDSAT ETM+ had a higher spatial resolution (15 m instead of 30 m) for the initial land use classification (LUC).

Each set of parameters can therefore be applied to a specific land use class only (urban, agricultural, forest etc.). For this reason the fourteen land use classes derived from satellite data have been reclassified into the following seven major land use classes for which the relevant parameters were available: a) water; b) densely built-up and industrial areas; c) medium and sparsely built-up areas; d) forest; e) grassland; f) agricultural fields; and g) clouds and "not classified" (see Table 5.2 and Figure 5.9).

5.6 Modelling of the turbulent heat flux densities Q_H and Q_E

The net all wave radiation and ground heat flux density have now been modelled. Only the turbulent flux densities Q_E and Q_H remain unknown in equation 3.8.

For the calculation of the turbulent heat flux densities (Q_H and Q_E) a simple Bowen-Ratio approach was used. The Bowen Ratio is mostly determined from *in situ* micrometeorological measurements. Apart from the Eddy-Covariance approach the Bowen Ratio approach is one of the few possibilities to calculate the latent and sensible heat flux (Oke, 1980).

The Bowen-Ratio (β) is described as:

$$\beta = Q_H / Q_E \qquad (5.10)$$

Typical values for β are between 0.3 and 0.8 for vegetated areas and forest, from 1 to 2 for light built-up areas and higher than 2 for medium to dense built-up urban environments, depending on the density of the buildings and vegetated areas. Liu and Foken (2001) and Ma et al. (2003) use the Bowen-Ratio for the modelling of Q_E and Q_H with *in situ* measurements.

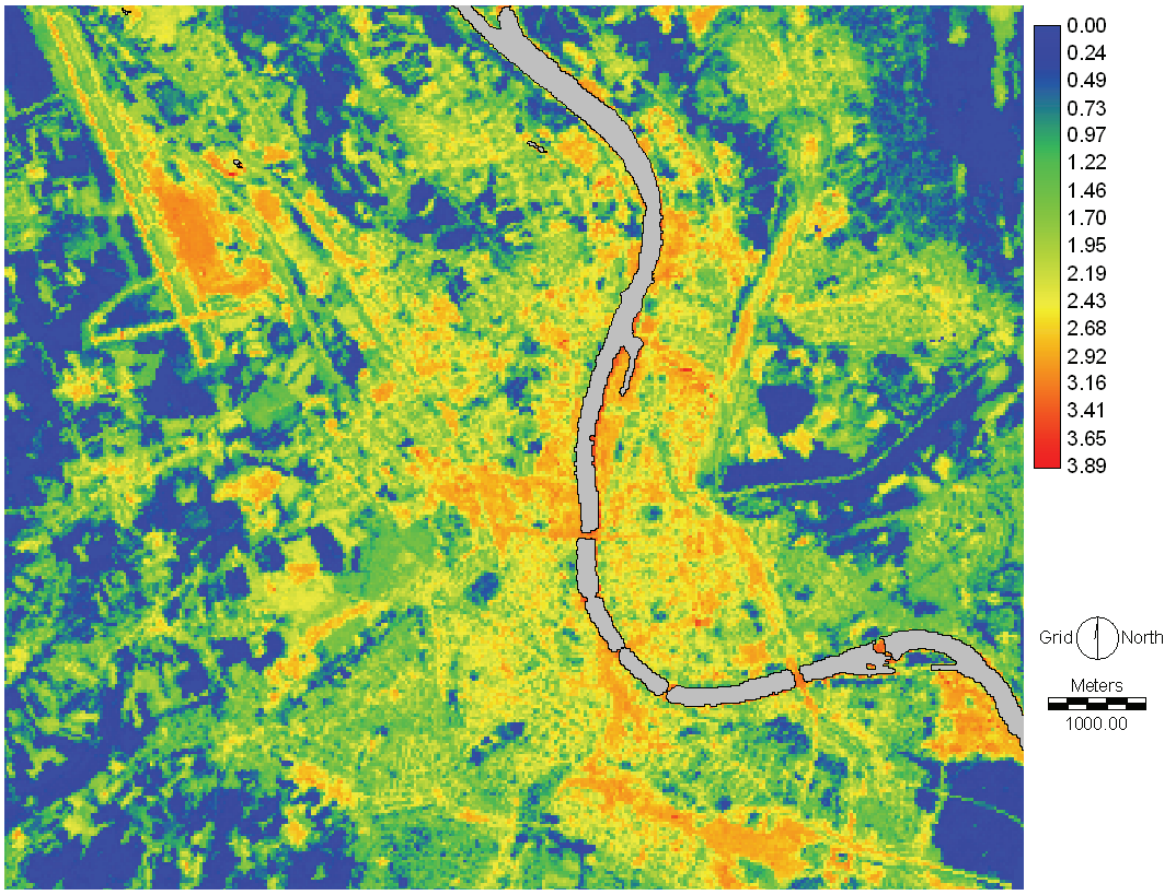

Fig. 5.10: The Bowen-Ratio derived from the LANDSAT ETM+ image

The NDVI shows the available vegetation and therefore the potential evapotranspiration which is equal to the latent heat flux density Q_E. Therefore we need to establish a relationship between the NDVI and Q_E through the Bowen-Ratio similar to Liu & Foken (2001) or Ma et al. (2003).

From the satellite derived NDVI and *in situ* derived Bowen-Ratios at the IOP-sites and also some literature values, the Bowen-Ratio for the spatial domain was calculated with a second-degree polynomial regression between the Bowen Ratio and the NDVI (R^2= 0.95) as shown in Figure 5.11 below.

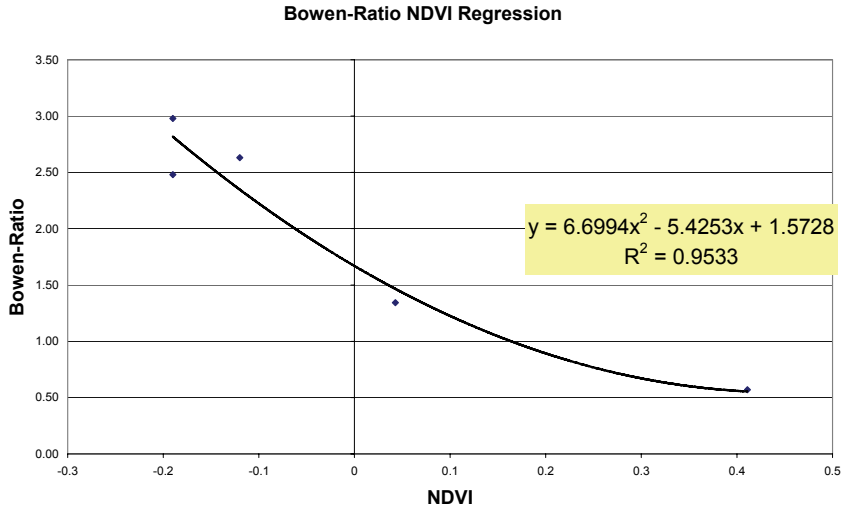

Fig. 5.11: Polynomial regression function between the Bowen- Ratio and the NDVI for the LANDSAT ETM+ scene.

The use of NDVI for the Bowen-Ratio and therefore the latent heat flux density Q_E follows the assumption that the latent heat flux density is dependent on the vegetation fraction; therefore, the available water for evapotranspiration is dependent on the NDVI. If the Bowen-Ratio is known, then, from the remaining energy, Q_E and Q_H can be calculated based on the assumption that the energy flux density balance should be closed.

In Figure 5.10 it can be seen that the forest and fields show the lowest Bowen-Ratios, whereas the dense built up areas (including the airport) have the highest values. Due to the dependency of the Bowen Ratio on the NDVI and the specific properties of water, the Bowen-Ratios for water areas are not correct. Therefore the River Rhine was masked out. The image shows the typical distribution of values according to the *in situ* measured Bowen-Ratios and the densely and sparsely built up areas can clearly be distinguished together with the vegetated areas.

6. Results

6.1 Validation of the thermal datasets

6.1.1 During BUBBLE

The *in situ* measurements at the stations described above were compared to the values derived from the mentioned satellite images. In total 16 AVHRR and 13 MODIS images were analyzed during the 30 days of the IOP, of which only about 11 days were suitable for optical remote sensing due to cloud cover.

Calibration of LANDSAT ETM+, AVHRR and MODIS data shows an accuracy of between 0.5 K and 3 K, which is approximately 2 – 4 % compared to radiation measurements at a temperature of 300 K (Kerenyi & Putsay, 2000; Schott et al., 2001; Wan et al., 2002).

The *in situ* instrumentation has an operational error of 5 – 15 W/m^2 (≈ 1 – 3 %), even with very good calibration in field campaigns (Christen & Vogt, 2005 and oral communications Vogt). This is better than the accuracy during the course of the day of 10 % according to the datasheet of Kipp & Zonen.

Generally at all the available sites, the mean absolute percentage difference (MAPD) between MODIS and *in situ* measurements are higher during daytime in the rural areas (5.9 %) than in the urban ones (4.2 %), but during the night the difference changes to 3.1 % in urban and 2.1 % in rural on average. The differences between the sites within the three AVHRR satellites are platform dependent. The most accurate results were achieved with the AVHRR 14, which has an overall accuracy for *in situ* measurements of 2.2 %, followed by the AVHRR 16 with 3.9 % and the AVHRR 15 with 4.1 %. Generally the nighttime overpasses for MODIS and the three different AVHRR satellites show higher correlations with ground data than the daytime orbits. In Figure 6.1 below there is a scatter plot of the measurement and values from all scenes, all sites and all algorithms used together with the coefficient of determination (R^2).

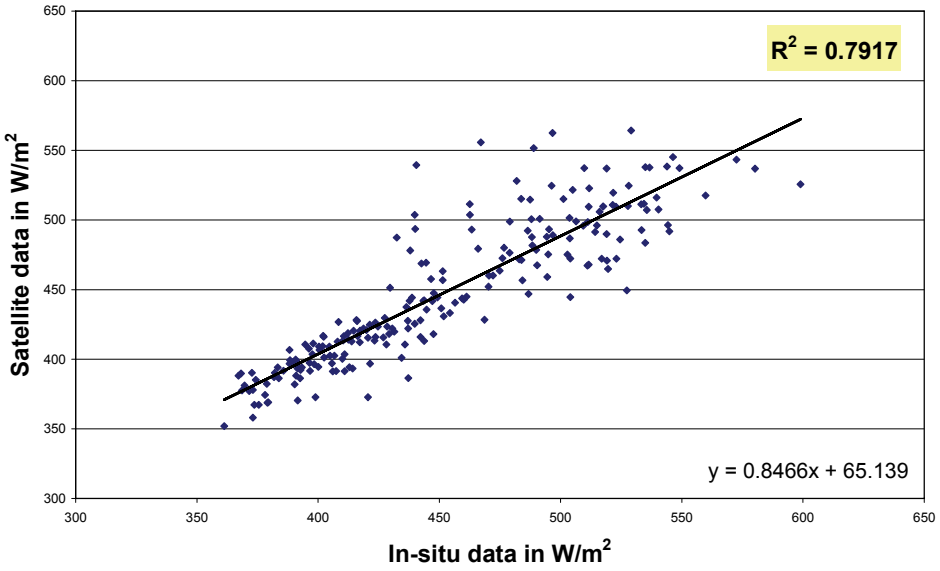

Fig. 6.1: Scatterplot of all (all sites, all algorithms and all satellites) satellite data versus the *in situ* measured values (N=217)

As we see in Figure 6.1 the accuracy between *in situ* and satellite derived Q_{LU} during nighttime is clearly higher then at daytime but nevertheless there is a clear relationship with a good R^2 value which makes the data useful for the further modelling of the net radiation.

To demonstrate the accuracy of the data, a two-day period (7 and 8 July, 2002) was selected: all the data from these two days are shown in Figure 6.2. The temporal datasets of the satellites over the two-day period show a good fit with the *in situ* data of the Sperrstrasse site. Only the AVHRR 16 in the afternoon from July 7, 2002 is clearly completely wrong due to cloud contamination of the pixel.

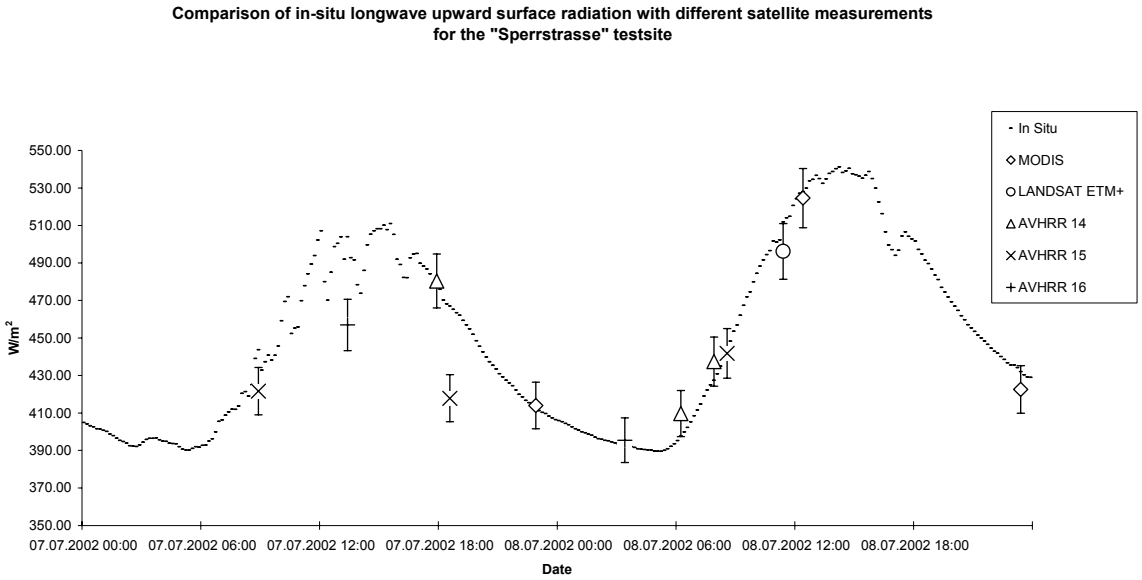

Fig. 6.2: Multisatellite data comparison with *in situ* data of longwave emission over two days at the Sperrstrasse site (U1) with the equation of Price (1984) used for the AVHRR-Data. Error bars are ± 3%

6.1.2 AVHRR SWT-algorithm intercomparisons

Using a comparative and statistical approach with *in situ* ground truth measurements the six SWT algorithms of Becker & Li (1990), Price (1984), Prata & Platt (1991), Sobrino et al. (1993), Sobrino et al. (1994) and Uliveri et al. (1992) were validated.

The results are slightly different for the three AVHRR satellites but the highest accuracy was achieved with Becker & Li (1990) (3.4 % MAPD), Price (1984) (3.6 %) and Sobrino et al. (1994) (3.9 %) whereas Ulivieri et al. (1992) (5.1 %), Prata & Platt (1991) (6.8 %) and Sobrino et al. (1993) (16.5 %) showed much higher differences (see Table 6.1).

Tab. 6.1: Average differences in percent of the AVHRR scenes with the different split-window algorithms to the *in situ* measurements over all the sites and all the scenes

Satellite	Ulivieri 92	BeckerLi 90	Sobrino 94	Price 84	PrataPlatt 91	Sobrino 93	Mean
AVHRR 14	3.7%	2.2%	2.3%	2.6%	6.5%	10.3%	4.6%
AVHRR 15	6.6%	4.0%	5.0%	3.7%	5.5%	6.1%	5.2 %
AVHRR 16	5.3%	4.3%	4.7%	4.7%	9.2%	27.4%	9.3 %
Mean	5.2%	3.5%	4%	3.7%	8.1%	14.6%	

6.1.3 Comparison of sites

Comparing the eight micrometeorological sites with all the satellite data, the best results were achieved at the Sperrstrasse urban site (2.6 %) and the Lange Erlen rural site (2.5 %). The largest differences were found at the Grenzach rural sites (4.8 %) and the Messe urban site (4.3 %). More detailed results can be found in Table 6.2 a) (all data with Becker & Li, 1990) and 6.2 b) where the best equation for each AVHRR data set was used (Becker & Li (1990) for AVHRR 14 and 16 and Price (1984) for AVHRR 15). When it comes to the R^2 values between *in situ* and satellite data, slightly different results are apparent. The R^2 for the AVHRR 14 equals 0.88, for the AVHRR 15 only 0.60 and for the AVHRR 16, 0.90. The Grenzach site shows the weakest correlation of all sites regarding all three AVHRR platforms; if the Grenzach site is excluded from the verification, the results improve to an R^2 of 0.92, 0.68 and 0.92 respectively. Nevertheless, the AVHRR 15 performs far less reliably than its sister satellites. MODIS nighttime results show an R^2 of 0.81 and 0.65 during daytime.

Tab. 6.2: a) Differences at the different sites for different satellite platforms (in percent) for the algorithm of Becker & Li (1990) and b) the coefficients of determination (R2) with the best suiting algorithm for each AVHHR platform

a)

Sites/ Satellite	Spalen-ring U1	Sperr-strasse U2	Messe U3	All-schwil S1	Lange Erlen R2	Village-Neuf R3	Gempen R4	Gren-zach R1	Mean
ETM+	1.9 %	2.1 %	1.6 %	2.6 %	1.3 %	5.8 %	-	-	2.6 %
AVHRR 14	2.2 %	1.1 %	2. 8 %	2.8 %	1.3 %	2.2 %	2.6 %	3.3 %	2.3 %
AVHRR 15	3.0 %	3.9 %	7.0 %	3.0 %	4.7 %	1.9 %	2.3 %	7.2 %	4.1 %
AVHRR 16	4.5 %	2.9 %	4.5 %	4.8 %	1.8 %	5.5 %	2.8 %	4.8 %	4.0 %
MODIS	2.2 %	2.9 %	5.6 %	4.0 %	3.2 %	3.8 %	5.3 %	3.8 %	3.9 %
Mean	2.8 %	2.6 %	4.3 %	3.4 %	2.5 %	3.8 %	3.3 %	4.8 %	

b)

Sites/ Satellite	Spalen-ring U1	Sperr-strasse U2	Messe U3	All-schwil S1	Lange Erlen R2	Village-Neuf R3	Gempen R4	Gren-zach R1	Mean
AVHRR 14	0.79	0.99	0.95	0.99	0.96	0.84	0.90	0.64	0.90
AVHRR 15	0.27	0.64	0.86	0.36	0.72	0.92	0.97	0.04	0.60
AVHRR 16	0.89	0.89	0.98	0.81	0.98	0.95	0.92	0.79	0.88
MODIS day	0.61	0.50	0.29	0.63	0.50	0.85	0.94	0.85	0.65
MODIS night	0.84	0.79	0.35	0.85	0.97	0.85	0.97	0.91	0.81
Mean	0.68	0.86	0.74	0.73	0.83	0.88	0.94	0.65	

Although the main focus of this thesis is on the accuracy assessment of longwave upward surface radiation (in Wm^{-2}) for further implementation into radiation and heat flux density modelling, most research papers give their accuracies for surface temperature in K or °C. Therefore some results are presented in K (see Table 6.3 below).

Tab. 6.3: Accuracy assessment with bias and RMSE for each algorithm in K compared to the *in situ* measurements.

Satellite/ Algorithm	Ulivieri 92	Becker&Li 90	Sobrino 94	Price 84	PrataPlatt 91	Sobrino 93	LANDSAT ETM+	MODIS day	MODIS night
BIAS AVHRR 14	2.5	1.7	1.6	1.9	4.4	6.1			
RMSE AVHRR 14	0.8	0.2	0.6	0.4	1.8	4.7			
BIAS AVHRR 15	5.0	3.1	3.7	3.0	3.7	4.1			
RMSE AVHRR 15	2.0	1.5	1.5	1.5	1.9	2.7			
BIAS AVHRR 16	4.0	3.0	3.3	3.4	6.0	20.9			
RMSE AVHRR 16	2.1	1.6	1.8	1.6	1.8	18.6			
Mean bias	3.8	2.6	2.9	2.8	4.7	10.4	1.9	1.3	0.7
Mean RMSE	1.6	1.1	1.3	1.2	2.2	8.7	1.2	0.8	0.6

The accuracy of the LANDSAT ETM+ data has a bias of 1.9 K and a RMSE of 1.2 K. For the MODIS data, the accuracy for daytime images was 1.3 K and for the night time ones 0.7 K. The results for the AVHRR's were much less accurate than the LANDSAT ETM+ or MODIS data. The results for the different SWT algorithms show again that Becker&Li 90 and Price 84 are the most accurate of the six algorithms.

6.1.4 ASTER and post-BUBBLE

In the same 2003 timeslot as the MODIS data an AVHRR dataset consisting of 26 scenes (from AHVRR 14 to 17) was validated using the data from the sites mentioned above but only for the two best performing algorithms, those of Becker & Li (1990) and Price (1984). All available datasets from all AVHRR's, MODIS TERRA and AQUA were acquired for a time window of one day on either side of the 2003 ASTER overpasses (plus and minus one day). Unfortunately, several of the MODIS scenes around the August ASTER overpass were so clouded at the overpass time that they had to been omitted. These scenes were excluded from the statistics. A total of 13 MODIS scenes were analysed for the 2003 timeslots.

The validation results for 2003 showed AVHRR 16 performing most accurately (1.3%), followed by AVHRR 14 (1.5%) and AVHRR 17 (2.1%), whereas AVHRR 15 (2.3%) fell behind once again. These recent values are more accurate than during BUBBLE, but it is important to bear in mind that these values are based only on three sites (two rural, one urban) and not on eight.

The overall reliability of the data from all seven ASTER scenes (from 2000 to 2005) was very high, with a MAPD of only 2.5% (13 Wm^{-2}) and an R^2 of 0.94. The two scenes from 2003 also yielded very clear results, with an average accuracy of 1.5% or 8 Wm^{-2}.

For the AVHRR, the two best suiting algorithms from BUBBLE (Price 84 and Becker&Li 90) were used for validation purposes; in total 26 scenes were analysed. An overview of the results can be found in Table 6.4 (following) with the better suiting algorithm always used for the respective AVHRR satellite.

Tab. 6.4: Accuracy assessment of the different satellite platforms for the 2003 longwave upward radiation datasets. Mean absolute percentage differences (MAPD) between *in situ* and satellite data together with the corresponding R^2 values.

Satellite	AVHRR 12	AVHRR 14	AVHRR 15	AVHRR 16	AVHRR 17	ASTER	MODIS Terra	MODIS Aqua
MAPD	2.2	1.5	2.3	1.3	2.1	1.5	2.7	1.7
R^2	0.86	0.99	0.98	0.72	0.96	0.99	0.96	0.97

Both the Price 84 and Becker&Li 90 algorithms performed well, with differences of less than 0.2 % between the results of the two. For the purposes of this study, then, they are equal in accuracy, which confirms the findings of the 2002 dataset. Note that the AVHRR 16, which performed worst in 2003, had only two suitable overpasses in the 2003 time-slots; nevertheless, the findings seemed to confirm the 2002 conclusion that AVHRR 15 was the least accurate of all the AVHRR satellites, whereas AVHRR 14 was the best again. The R^2 values for each of the satellites can be found in Table 6.4, which charts the overall accuracy of data from all overpasses. As noted for the BUBBLE data in 2003, the nighttime readings are also more accurate than the daytime ones. The MODIS results improved significantly on those of BUBBLE (differences were 4.4% and 2.3% respectively for Terra Day / Night and 4.2% and 1.6% respectively for Aqua Day / Night).

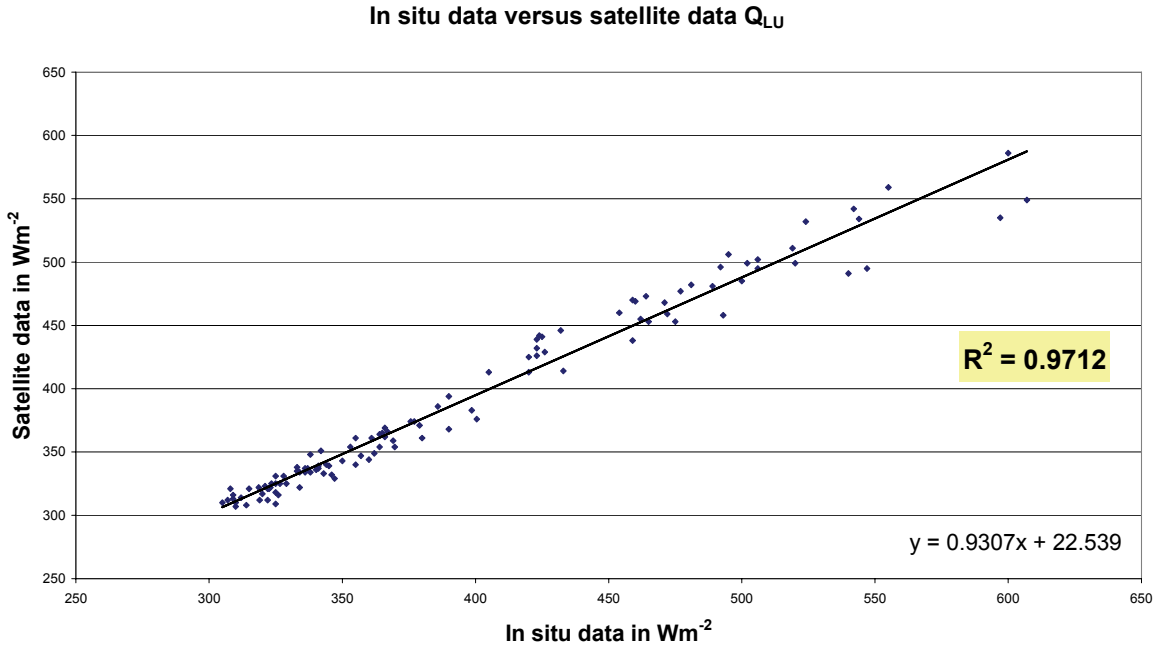

Fig. 6.3: Overall accuracy and graph of all Q_{LU} values from 2003 satellite data versus the *in situ* measurements (N=113)

6.1.5 The VarioCam data

As discussed in Voogt & Oke (1998), when working with very high-resolution spaceborne or airborne remote sensing data one important factor is the problem of urban anisotropy. This problem exists for all urban structures. Due to the changing viewing angle of the images and the changing altitude of the helicopter during the flight, however, it was impossible to implement any countermeasures to minimize its effect. Also, no atmospheric corrections were made to the datasets, meaning that the results have to be viewed with caution and can only be used as experimental data.

The roof temperatures from the VarioCam correspond within an accuracy of 2 K to the values recorded during BUBBLE with the infrared radiation pyrometers (KT-15) placed on the roofs at the same time of day (see also Christen 2005, Doerksen, 2004). For this comparison a 3 x 3 mean filter was applied to the VarioCam image to average the values of the roofs. As described in Table 4.2, this is also within the range of the instruments' accuracy.

To show the spatial distribution, three transect profiles are shown in Figure 6.4 through the Sperrstrasse (U1), where the main tower was stationed, going over a flat gravel roof and over a tilted roof. The data along transects 1, 2 and 3 show the most serious problem with airborne high-resolution thermal imagery in Figure 6.5 a), b) and c). Due to the urban anisotropy it is difficult to obtain accurate wall temperatures or the temperatures of vertical surfaces. The roofs are clearly visible in all three transects, with the sunward- sides much hotter than the shadowed ones, whereas, the temperatures are the lowest in the street canyon. Note also in Figure 6.5 a) the flat roof, which exhibits a temperature almost exactly between the shadowed and sun exposed tilted roofs. Figure 6.5 d) shows a transect of the surface temperatures inside the canyon, taken using thermal infrared thermometers (IRT) during BUBBLE at the same time of day as the helicopter overpass. The wall temperatures were taken with a field of view (FOV) of 15° for each wall segment and 11° (FOV) for the ones placed on the roofs. In Figure 6.5 d), the roof temperatures were used for both sides of the canyon.

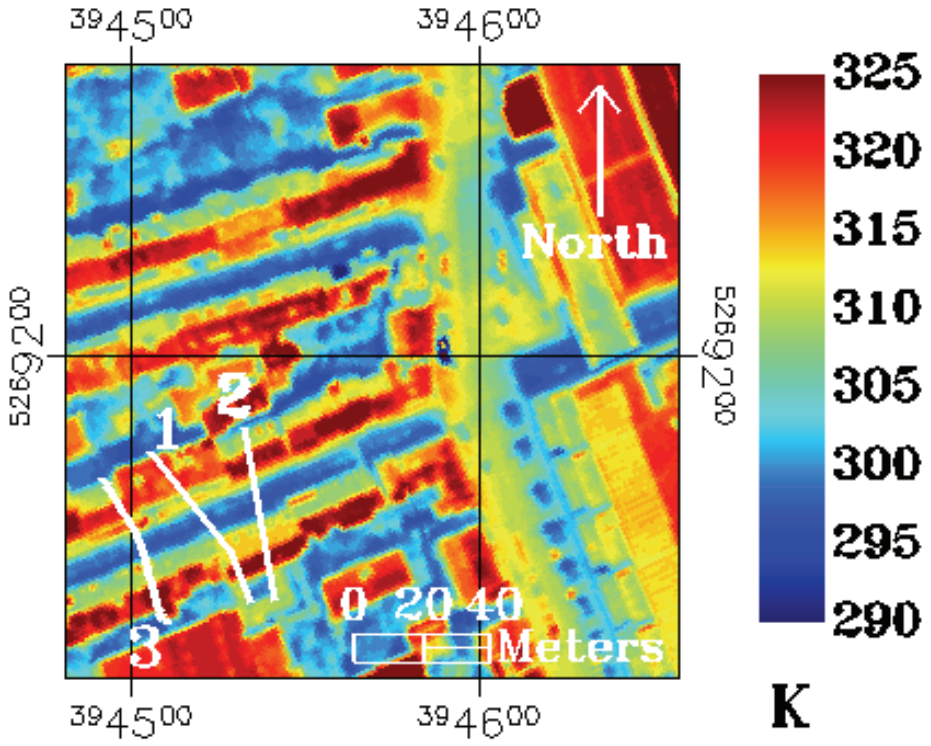

Fig. 6.4: Thermal image of Sperrstrasse site from July 2004 with the three profiles transects shown

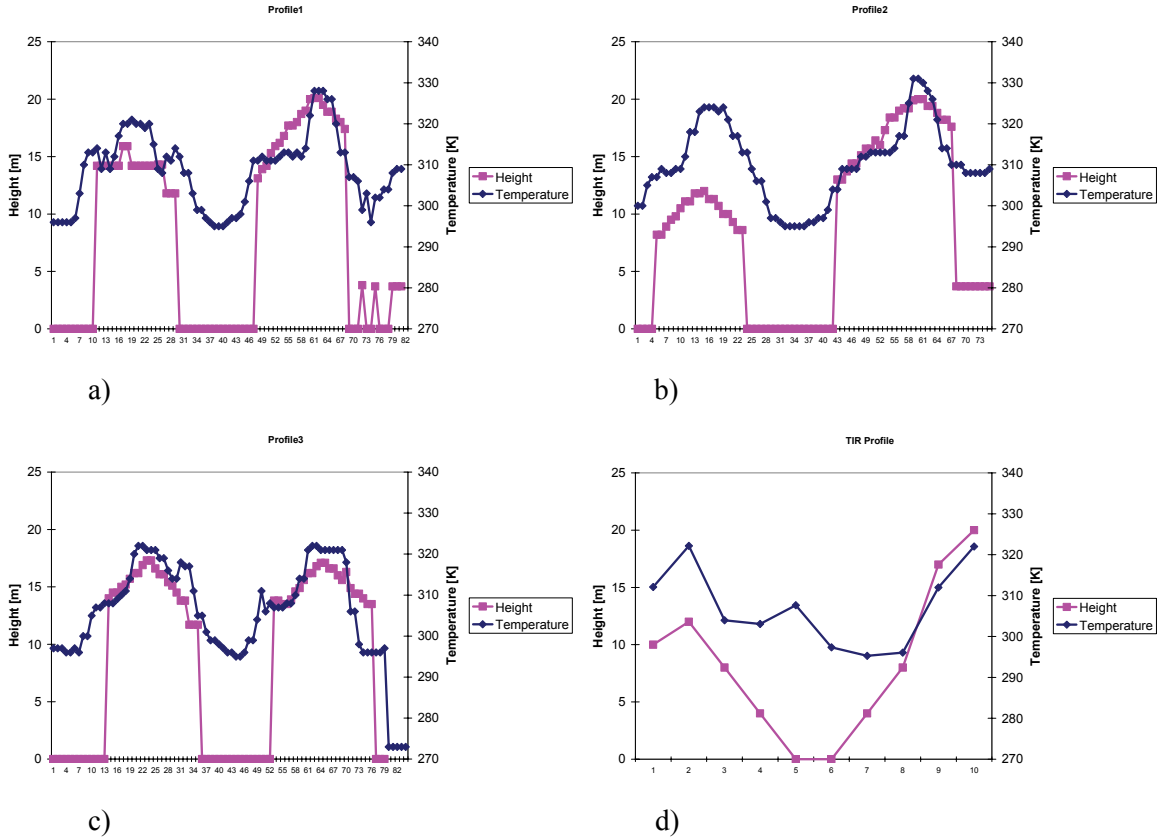

Fig. 6.5: Transect profile trough the Sperrstrasse site using the VarioCam thermal data mosaic with a) Profile 1, b) Profile 2 and c) Profile 3 in Figure 9.2. Chart d) shows a transect which was measured with *in situ* thermal infrared thermometers facing the walls and roofs in the canyon.

6.2 Net all wave radiation Q*

6.2.1 BUBBLE

The modelled net all wave radiation (Q*) values were also compared to the *in situ* measurements and validated as described above to ensure the accuracy of the input data for the OHM model.

A comparison with *in situ* measurements of net radiation produced a mean absolute difference (MAD) of 27 Wm^{-2} with an RMSE of 23 Wm^{-2}. The validation of the net radiation yielded an R^2 of 0.97 as shown in Figure 6.6 below.

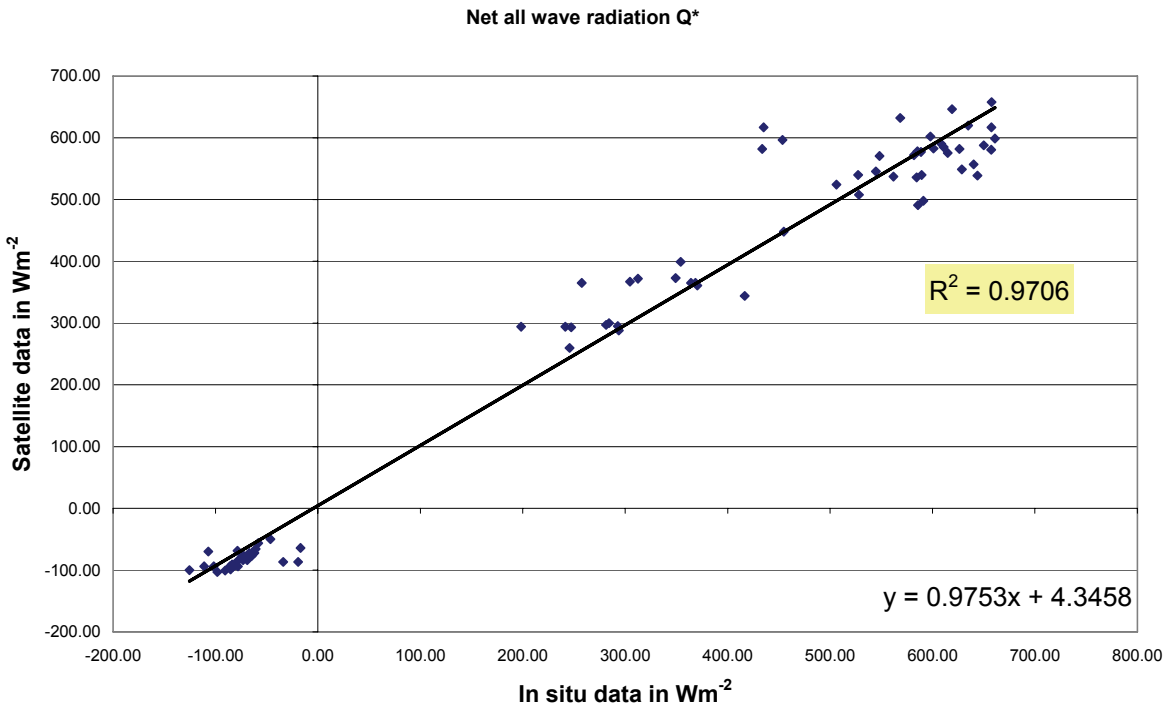

Fig. 6.6: Modelled versus *in situ* measured net radiation for all the sites during the BUBBLE-IOP (N= 80)

Generally the accuracy of the nighttime modelled net radiation was more accurate than that of the daytime datasets. Table 6.5 clearly shows that rural sites were modelled more accurately than urban sites. Due to the special location of U3, which is below the spatial resolution of AVHRR or MODIS, the modelled values show very high differences when compared to the *in situ* measurements.

Tab. 6.5: Mean absolute difference (MAD) and RMSE in Wm^{-2} between the modelled and *in situ* measured net radiation Q* during BUBBLE

Site	U1	U2	U3	S1	R1	R2	R3	R4
MAD	26	26	66	24	22	26	40	18
RMSE	26	38	54	26	23	19	34	17

The spatial distribution of Q* is shown in Figure 6.7, which shows about the same net radiation in the city as over the surrounding rural areas (except the forests). Only the forest and industrial areas show a clear urban-rural difference in Figure 6.7. The spatial distribution of the net all wave radiation Q* in

Figure 6.7 shows that, whereas industrial and high density areas show low net radiation values, forests have the highest ones due to their low albedo and Q_{LU} values. Between the urban and rural areas, as stated by Christen & Vogt (2004), the differences are very small, with no clear urban-rural border definition. Nevertheless, as mentioned in Chapter 3.1.7, the net radiation over urban areas is slightly lower than over rural ones.

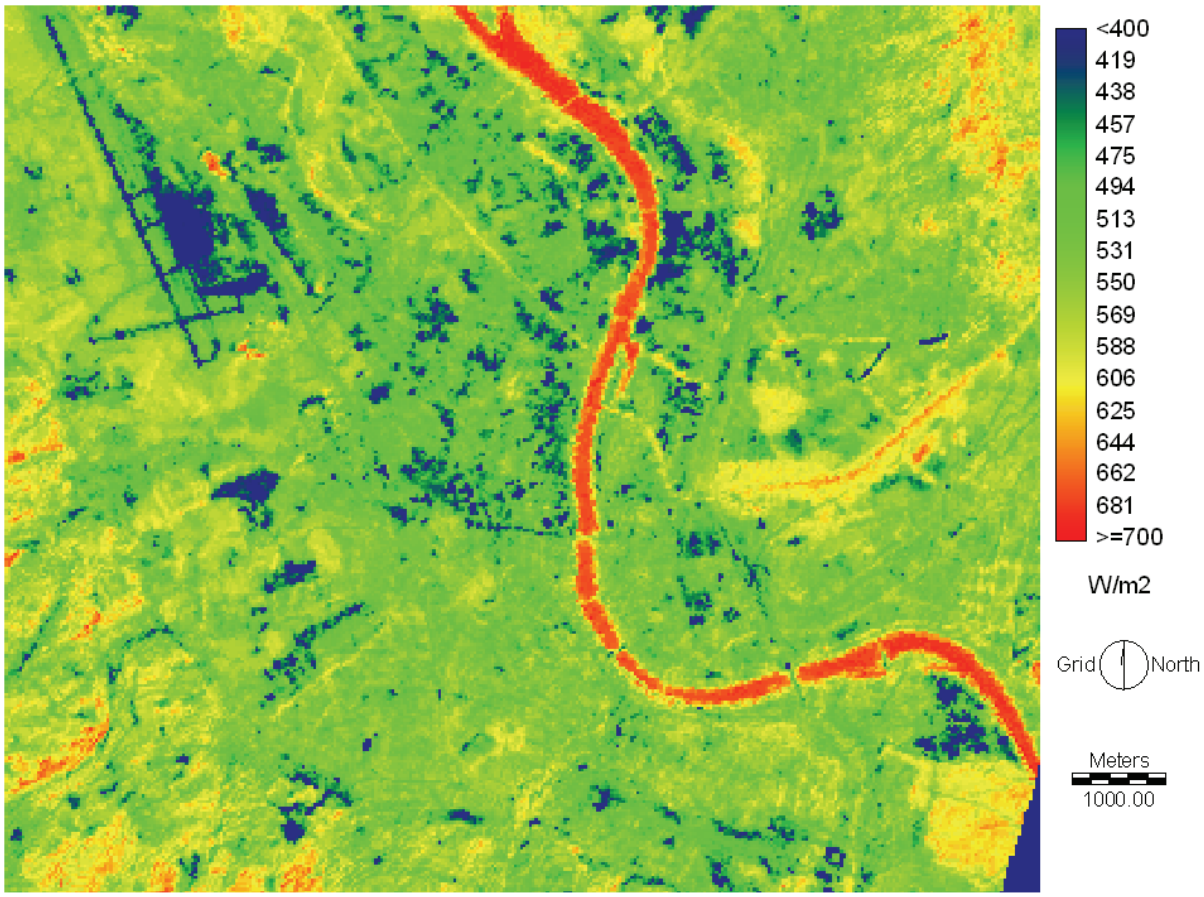

Fig. 6.7: Modelled net radiation (Q*) for the LANDSAT ETM+, July 8, 2002, Day 189, 10:10 UTC

6.2.2 ASTER and post-BUBBLE

For the 2003 datasets, Q* was calculated for eight scenes, producing a MAD of 14 Wm^{-2} and an RMSE of 12 Wm^{-2}, with generally lower MAD's for nighttime overpasses (where the total value of Q* is not more than -100 Wm^{-2}). The coefficient of determination (R^2) was 0.99 (with N=21). There was also no clear difference in accuracy between the urban and rural sites but the results showed also the lowest values over industrial areas and the highest over water and forests.

The results with ASTER for 2003 are therefore more reliable than those modelled by Chrysoulakis (2003) for Athens with ASTER data and SEBAL noting a MAD of 44 Wm^{-2}.

To restate an earlier caveat, however, while the 2003 results are more accurate than those taken during BUBBLE in 2002, because fewer data were available for 2003, these results must be interpreted with care. The net all wave radiation was compared only to the *in situ* measurements from the Lange Erlen (R3), Gempen (R4) and Klingelbergstrasse sites.

6.2.3 High resolution net radiation

According to the measurements made at the *in situ* sites (data from 2004 from the Klingelbergstrasse urban site and from 2002 from the urban sites U1, U2 and U3) the values fall within an expectable range for this time of day on a typical midsummer day (between 400 Wm^{-2} and 650 Wm^{-2}).

Further processing of the very high resolution dataset according to the steps described in the chapters above was not conducted, considering that only one site (Klingelbergstrasse) is covered by the thermal image and the net radiation values could not be reliably validated due to the unavailable *in situ* data.

In Figure 6.8 below, note the lower Q* over the roofs when compared to that over the trees, vegetation and roads, all of which show a much higher net all wave radiation. Not surprisingly, the areas shadowed by the buildings also give a very low net radiation. Likewise, the sunward tilted roofs show higher values than their shaded counterparts away from the sun.

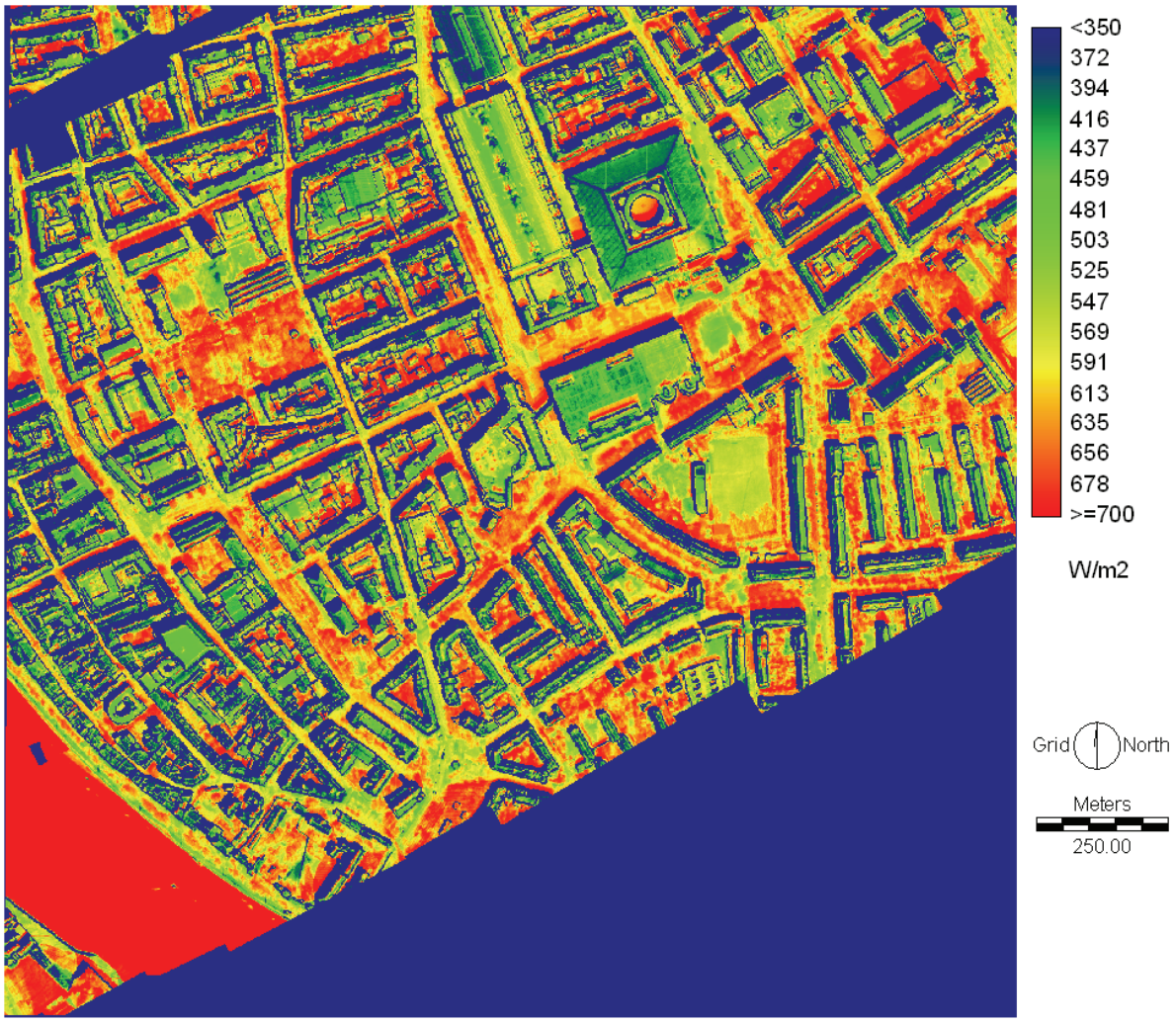

Fig. 6.8: Modelled net radiation (Q*) for a summer day ca. 10:00 (UTC) with 1 m resolution.

6.3 Storage heat flux density ΔQ_S

6.3.1 BUBBLE-IOP

The *in situ* measurements during the BUBBLE-IOP yielded ground heat flux density measurements for all six sites mentioned above (the sites Grenzach and Gempen were unfortunately not covered by the LANDSAT ETM+ image). The raw data was integrated into hourly averages. At some sites the ground heat flux density was measured directly (Allschwil, Grenzach, Village-Neuf); for the others it was calculated as a residual value from eddy-covariance measurements (Christen & Vogt 2004; Webb et al. 1980). The results were computed for July 8, 2002 and June 25 & 26, 2002, when multiple overpasses were available (see Table 6.6).

Tab. 6.6 : Satellite overpasses used for the modelling of ΔQS with the OHM model during BUBBLE

Satellite	Time (UTC)	Date	Additional Information
Landsat ETM+	10:10	08.07.2002	
AVHRR 14	06:47	08.07.2002	
AVHRR 16 day	11:10	08.07.2002	
AVHRR 16 night	2:13	08.07.2002	
MODIS day	11:20	08.07.2002	
MODIS night	22:20	08.07.2002	
AVHRR 15	7:23	25.06.2002	
MODIS day	11:40	25.06.2002	
AVHRR 16	12:45	25.06.2002	
AVHRR 16	12:34	26.06.2002	
MODIS day	10:40	26.06.2002	
MODIS night	21:50	26.06.2002	
Landsat ETM+	10:10	12.06.2001	Used for land use classification
ASTER	10:40	12.06.2001	Used for land use classification

For the daytime overpasses (from 4 UTC to 9 UTC) net radiation was modelled using the respective satellite data and SWIM (Short Wave Irradiance Model), whereas for the night-time overpasses only the longwave atmospheric counter radiation and longwave terrestrial emission had to be considered to calculate the net radiation according to eq. 3.6 or Figure 3.3.

For the complete aspect ratio (CAR) only the urban sites could be used for comparison. The computed results from the satellite data were compared with the respective *in situ* measurements at each measurement site. For the MODIS daytime, LANDSAT ETM+ and the MODIS nighttime images, more than one OHM approach was used because more than one image was available for the OHM calculation (see Table 6.7).

Table 6.7 shows the results of a comparison of the computed ground heat flux densities with measured data, a) b) and c) indicating the approaches used. For the CAR approach, the values for R2 and R3 (a)) are calculated from the average value for the areas with a complete aspect ratio of close to 1 surrounding the built up area (see Figure 6.10. a)) and are not, therefore, included in the statistics. The overall MAD for all of the sites is 17 Wm^{-2} with an RMSE of 17 Wm^{-2} with all the approaches used. If only the OHM is taken into account, the MAD and RMSE values are 16 Wm^{-2} and 13 Wm^{-2} respectively. The individual mean absolute differences (MAD) in Wm^{-2} for each site and each

calculation are shown in Table 6.7. The method used is noted with a) indicating CAR b) NDVI and c) OHM.

Tab. 6.7 : Mean absolute differences (MAD) between *in situ* and the modelled ground heat flux densities in Wm^{-2} at six sites (calculated using a)CAR, b) NDVI and c) OHM)

Sites	U1 Sperr.	U2 Spalen.	U3 Messe	S1 Allschwil	R2 V-Neuf	R3 L Erlen	Total MAD
	Mean absolute differences (MAD) between modelled and measured ground heat flux densities in W/m^2						
a) LANDSAT ETM+ 08.07.02	4	19	103		(44)	(15)	
a) MODIS day 08.07.02	1	32	96		(36)	(13)	
b) LANDSAT ETM+ 08.07.02	3	26	1	18	2	69	20
b) MODIS day 08.07.02	1	25	3	9	3	74	19
c) MODIS night / MODIS day 08.07.02	15	4	11	22	20	5	13
c) MODIS night / LANDSAT ETM+ 08.07.02	1	11	2	4	14	1	5
c) MODIS night / AVHRR 16 day 08.07.02	1	12	5	5	16	1	7
c) MODIS night /AVHRR 14 08.07.02	4	7	0	3	6	1	3
c) MODIS night / AVHRR 16 night	6	5	2	7	1	3	4
c) MODIS day / LANDSAT ETM+ 08.07.02	26	21	78	8	31	2	23
c) MODIS day / AHVRR 14 08.07.02	27	20	71	13	26	2	27
c) MODIS day / AVHRR 16 night 08.07.02	25	18	69	10	21	2	24
c) AVHRR 16 day / AVHRR 14 08.07.02	17	40	24	15	3	11	15
c) AVHRR 16 day / AVHRR 16 night	11	25	24	15	3	11	15
c) LANDSAT ETM+/AVHRR 14 08.07.02	5	17	8	10	5	3	8
c) LANDSAT ETM+/AVHRR 16 night 08.07.02	7	6	7	14	1	2	6
c) AVHRR 14 / AVHRR 16 night 08.07.02	25	54	33	4	9	22	24
c) AVHRR 16 / AVHRR 15 25.06.02	30	15	7	10	27	6	16
c) MODIS day /AVHRR 15 25.06.02	39	10	76	9	16	1	25
c) AVHRR16 / MODIS day 25.06.02	15	28	19	36	44	9	25
c) AVHRR 16 / MODIS day 26.06.02	14	37	7	40	37	12	25
c) MODIS night / AVHRR16 26.06.02	13	24	9	15	18	1	13
c) MODIS night / MODIS day 26.06.02	15	22	9	13	17	1	13
Site MAD	**13**	**21**	**29**	**13**	**15**	**11**	**17**
Site RMSE	**11**	**12**	**34**	**10**	**13**	**21**	**17**

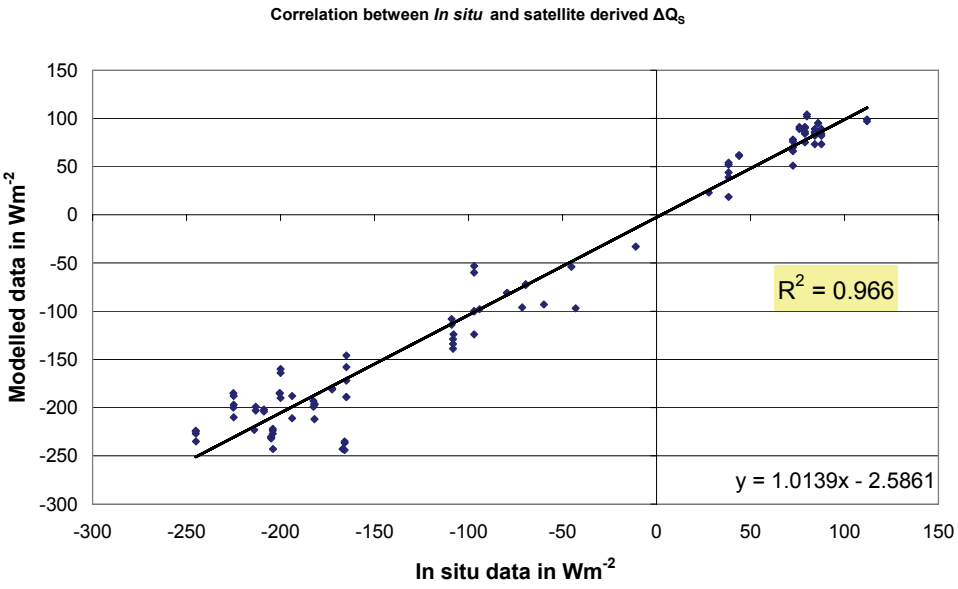

Fig. 6.9: Regression between all OHM modelled and measured ΔQ_S values (N=113)

As shown above for the net radiation figure, Figure 6.9 illustrates how the daytime values are less accurately modelled than the nighttime ones for ΔQ_S also. The coefficient of determination (R^2) for all OHM data is 0.96, which indicates a very high correlation between the modelled and measured datasets.

Whereas U1, R3 and S1 show the most consistent results, U2 and U3 are the most erratic in the table. There is therefore no clear distinction between rural or urban sites, although the sites U2 and U3 are on average far less reliable than the other sites.

Regarding the data from the various overpasses processed with the OHM model, the runs with "MODIS night" on July 8, 2002 show very high correlations as do those of the LANDSAT ETM+, no matter which of the satellite scenes is used as a second image. The contrary goes for the "MODIS day" data, which show the weakest correlations with all scenes, even if they are used as the second scene, as on June 25 and 26, 2002.

As illustrated in Fig. 6.10 a), b) and c), the results of the three different approaches show similar patterns and values for the city and its surroundings (except a)) when they are modelled for approximately the same time of day.

In Figure 6.10 a), the data for the surface surrounding the built up area is treated as a rural field and corresponds well with rural measured values (see the results of a) for rural sites in Table 6.7): even though this surrounding area is not rural it was treated as such due to its complete aspect ratio of 1.

The higher storage heat flux density in the historic downtown area (about -240 Wm^{-2}) and around the harbour basin (industrial) north of the CAR- rectangle is clearly visible in Figures 6.10 b) and c), whereas the parks stand out as "green" areas with much lower ΔQ_S values (approximately -100 Wm^{-2}). Also the airport in the northwest corner of the image is clearly visible, together with the forest areas, which have a ΔQ_S of -80 Wm^{-2} during daytime and 30 Wm^{-2} at night – the lowest ΔQ_S of the entire tested area. The NDVI model registers finer differentiations in the urban areas but in the rural areas the OHM shows a clearer difference between rural and forest areas.

Figure 6.10 d) shows the nighttime ground heat flux density ΔQ_S determined using the OHM model approach, which is positive, i.e. directed into the urban structure at the urban sites or into the Earth's

surface at the rural sites. The difference between urban and rural sites is also clear, but to a much smaller extent than during the day (90 Wm^{-2} to 50 Wm^{-2}).

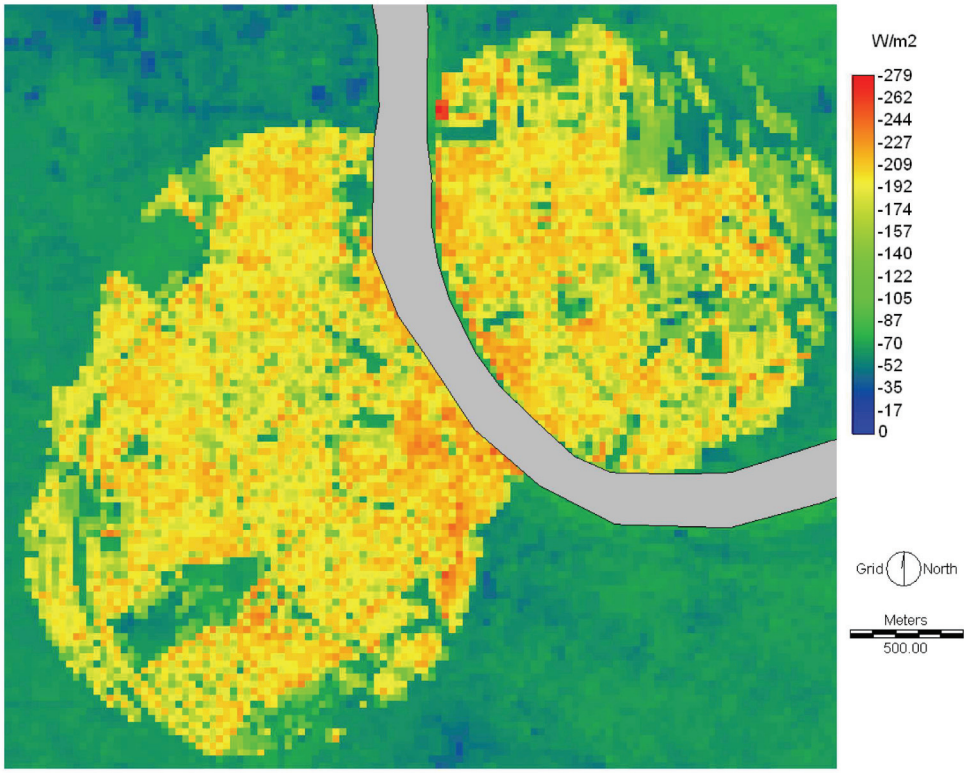

a)

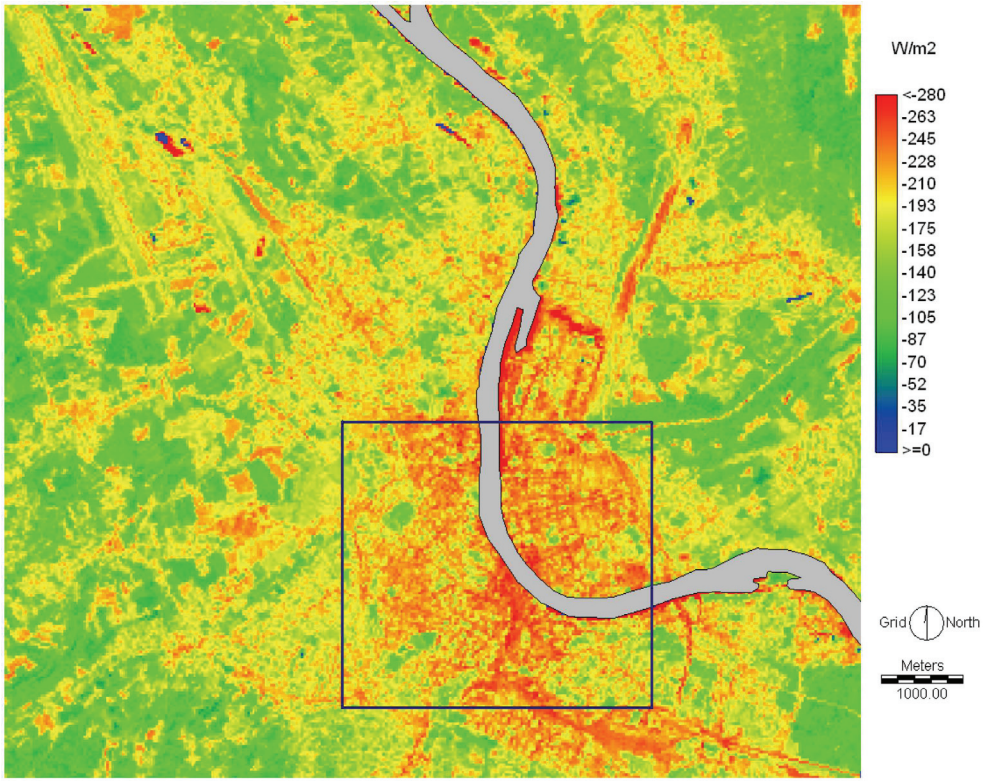

b)

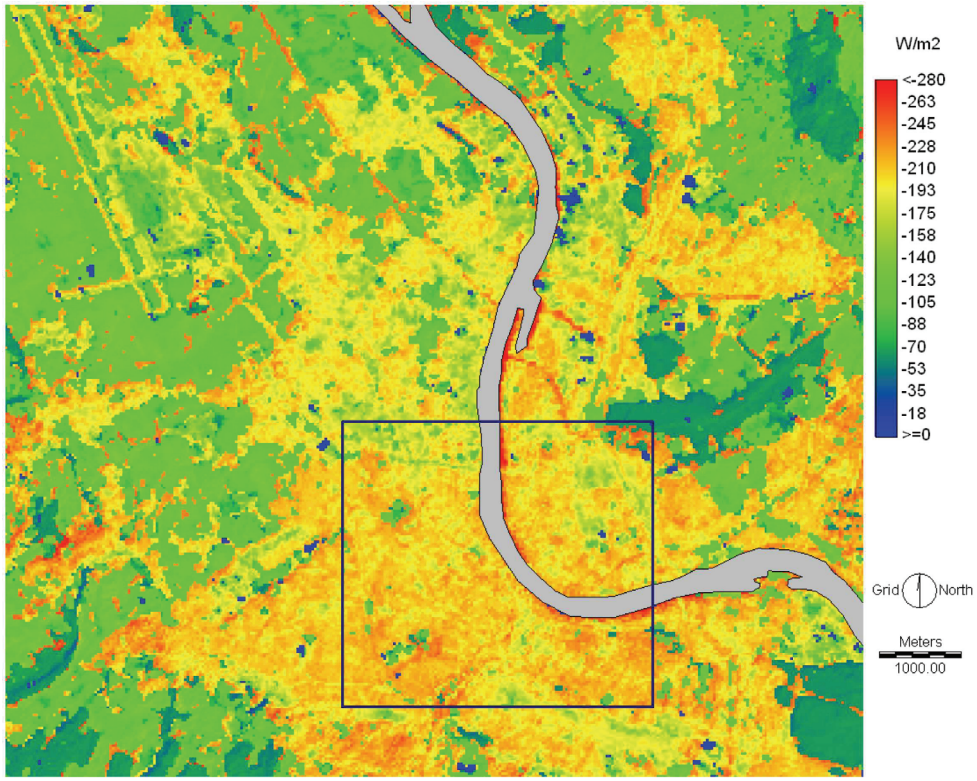

c)

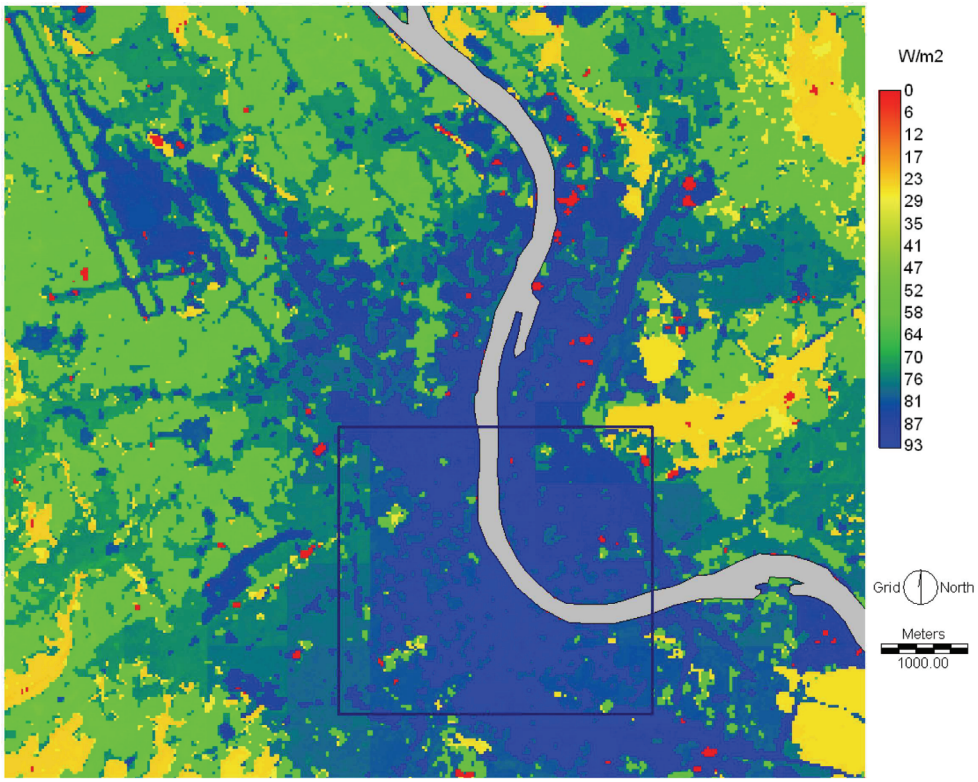

d)

Fig. 6.10: Ground heat flux density ΔQ_S in Wm^{-2} in the city of Basel for July 8, 2002; a) modelled with the CAR approach for 10:30 UTC; b) modelled with the NDVI approach with LANDSAT ETM+; c) modelled with the OHM approach applied on AVHRR 14 and LANDSAT ETM+ data; and d) nighttime ground heat flux density with OHM from MODIS and LANDSAT ETM+ at 22:20 UTC.

6.3.2 ASTER and post-BUBBLE

Modelling of the net all wave radiation Q* for the 2003 August scenes resulted in an average difference of 21 Wm^{-2}, which is a very useful result –even more consistent than results during BUBBLE: The ASTER scene showed a difference of only 12 Wm^{-2}. Therefore, there is a very strong argument for the further modelling of the ground heat flux density using the OHM approach.

Tab. 6.8 : Satellite data used for the modelling of the storage heat flux density ΔQ_S using the OHM model in 2003

Satellite	Time (UTC)	Date	Additional Information
ASTER	10:30	05.08.2003	
MODIS Terra	11:00	05.08.2003	
MODIS Aqua	12:40	05.08.2003	
AVHRR 17	20:40	05.08.2003	
AVHRR 15	7:20	05.08.2003	
Landsat ETM+	10:10	12.06.2001	Used for land use classification
ASTER	10:40	12.06.2001	Used for land use classification

The OHM approach was also used to model the ground heat flux density for the August 5, 2003 datasets (see Table 6.8), which consisted of five satellite overpasses.

For the August 2003 scenes the hourly average values from the BUBBLE *in situ* measurements were used because, although no flux density measurements were available on this date, the average ground heat flux density corresponds well within the same time of year. The ASTER overpass occurred on a very close DOY, with quite similar weather conditions, and the average values of the ground heat flux densities were also used as reference values for the comparison and validation of BUBBLE data in 2002. In addition to the six sites in Table 6.7 the Grenzach site (R1) was added because of the fuller coverage of the ASTER overpass (see Table 6.9).

The spatial distribution of ΔQ_S is shown in Figure 6.11. Note the higher ground heat flux densities in the densely built-up areas and the industrial sites in the eastern part. There is a clear difference between the different densities of the buildings, as well as between the rural areas and the forest (which show the lowest values). The values are not as high as for July 8, 2002 in Figure 6.10 b) or c), but show a very similar distribution.

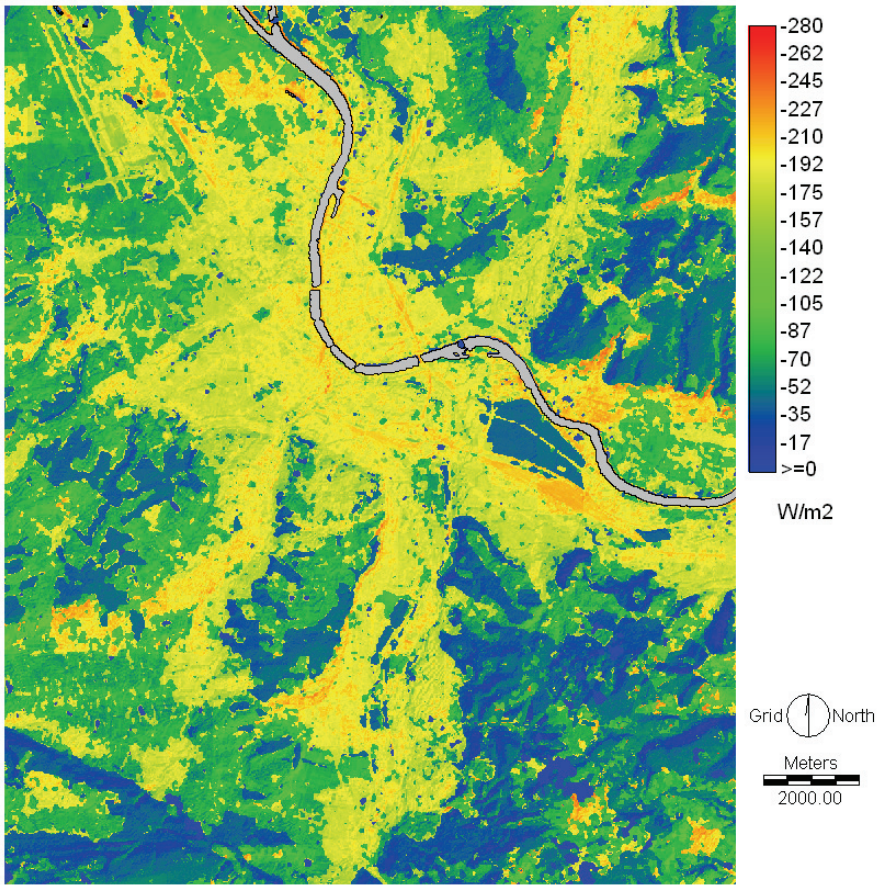

Fig. 6.11: Ground heat flux density (ΔQ_S) in Wm^{-2} for the ASTER overpass on August 5, 2003 modelled using the OHM approach

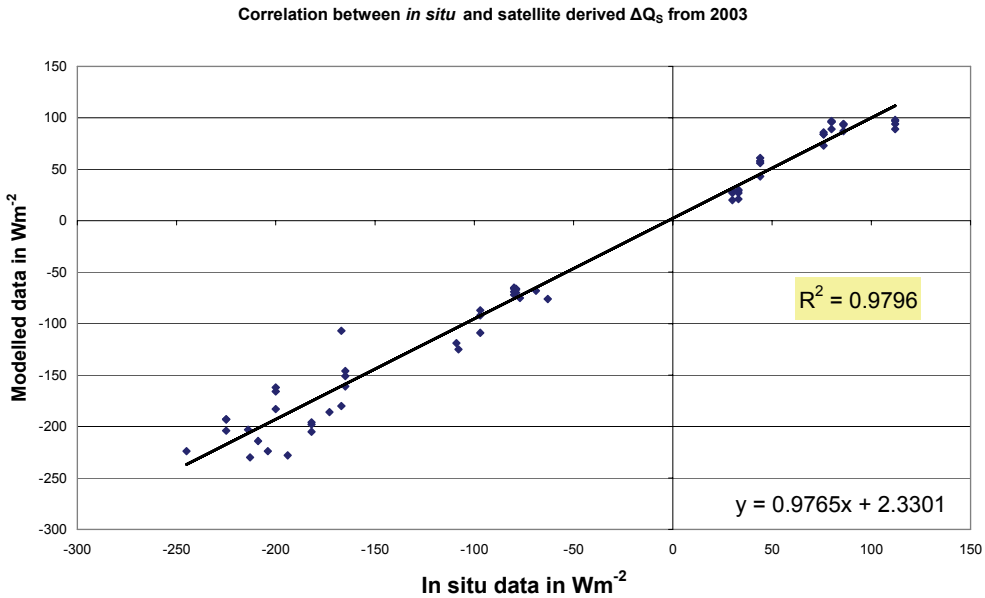

Fig. 6.12: Regression between all OHM modelled and measured ΔQ_S values (N=63) for 2003

The results showed an average difference (MAD) between modelled and *in situ* values of 16 Wm^{-2} and an R^2 of 0.98 (see Figure 6.12), both of which were similar to the 2002 BUBBLE results. This makes it obvious both that the OHM approach can be used on different satellite imagery (including ASTER, MODIS, LANDSAT ETM+ and AVHRR), and that the accuracy of the modelling approach is quite high. The NDVI approach was not used this time due to the differences between the NDVI's of different satellite systems (see Steven et al. 2003). The CAR approach was used with the Q* from the ASTER overpass for comparison with the results from BUBBLE (see Table 6.9).

Table 6.9 shows differences between the averages of the rural and urban sites, as well as a slightly greater reliability among the rural sites. Where U2 performs less accurately than U1 or U3, there is also roughly the same difference between R1 and R3, with R2's results the worst of the rural sites. When Table 6.9 is compared to Table 6.7, one striking difference is the noticeably stronger correlation of the R3 figures.

Tab. 6.9: Mean absolute differences (MAD) between *in situ* and the modelled ground heat flux densities in Wm^{-2} at seven sites (a) with CAR and b) with OHM.

Sites	U1 Sperr.	U2 Spalen.	U3 Messe	S1 Allschwil	R1 Grenzach	R2 Village-Neuf	R3 Lange Erlen	Total MAD
	Mean absolute differences (MAD) between modelled and measured ground heat flux densities in W/m^2							
a) with ASTER	16	34	57		(14)	(32)	(8)	27
b) with AVHRR 17 / AVHRR 15	23	9	1	3	6	1	3	7
b) with MODIS Aqua / ASTER	14	32	14	38	12	5	14	18
b) with MODIS Aqua / MODIS Terra	16	32	19	34	13	10	15	20
b) with ASTER/ AVHRR15	5	34	13	17	13	10	1	13
b) with AVHRR17/ ASTER	18	16	8	8	4	12	1	10
b) with AVHRR17 / MODIS Terra	15	16	7	8	12	14	10	12
b) with MODIS Terra / AVHRR 15	20	21	13	11	2	17	8	13
b) with MODIS Aqua / AVHRR 15	23	21	4	17	9	12	11	14
b) with AVHRR 17 / Modis Aqua	14	17	8	10	3	17	2	10
Site MAD	**16**	**22**	**10**	**16**	**8**	**11**	**7**	**13**
Site RMSE	**6**	**9**	**6**	**12**	**5**	**5**	**6**	**4**

In general, the OHM model enables an accurate modelling of the ground heat flux density for different times of day, although some difficulties arise when the time between the two overpasses and the respective net radiation calculations is less than one hour (e.g. ASTER and MODIS terra, see Table 6.8); therefore, the results between these two overpasses were omitted from Table 6.9.

Although fewer images were used in 2003, the results seem clear, when Table 6.9 (2003) is compared to Table 6.7 (BUBBLE), that the 2003 results are far more reliable than those from BUBBLE.

6.4 The turbulent heat flux densities Q_H and Q_E

6.4.1 BUBBLE

In determining turbulent heat flux densities (Q_H and Q_E), as with the storage heat flux density(ΔQ_S), hourly averages of *in situ* data from the same days were used to validate the results.

As for the values modelled from the satellite data, the results show a mean absolute difference between modelled and *in situ* values of below 16 Wm^{-2} for Q_H, whereas, for the Q_E the MAD is 28 Wm^{-2}. For R2 the differences in Q_E are generally higher than for urban sites. An overview of the results for each of the sites can be found in Table 6.10 below. There are only four sites (U1, U2, S1 and R2) for which both a useable *in situ* database and data modelled from remote sensing data were available. Grenzach (R1) is not covered by the remotely sensed data, Lange Erlen (R3) has no energy balance measurements (only the ground heat flux density), and Messe (U3) had no useful datasets due to too many data gaps. The Messe site was also only operated from June 24 to July 10, 2002.

Tab. 6.10: Mean absolute differences (MAD) for turbulent heat flux densities for the *in situ* sites in Wm^{-2}

Site	U1	U2	S1	R2
MAD Q_H	4	18	26	14
MAD Q_E	25	14	22	49

The coefficient of determination (R^2) is 0.92 for the sensible heat flux density and 0.72 for the latent heat flux density (N=12).

The following figure (Figure 6.13) shows an example for the LANDSAT ETM+ overpass. It must be noted that for night time modelling of Q_E and Q_H this Bowen-Ratio / NDVI approach is impossible yielding completely unusable results. For the River Rhine the modelled values are not representative due to the specific thermal properties of water, which were not included in the Bowen-Ratio / NDVI approach and are completely different from any other land use class. Therefore the River Rhine was masked out in Figure 6.13.

In Figure 6.13 a) the urban areas are clearly distinguishable due to their high negative sensible heat flux densities (below -200 Wm^{-2}), whereas the rural areas are lower than -100 Wm^{-2}, with forests showing even lower negative values. As for Figure 6.13 b) the results change completely: the highest negative values can be found in the rural areas, whereas the urban surface clearly shows very low negative latent heat flux densities. It is also clear, in Figure 6.13 a) and b), that the differences of Q_E values are much higher between rural and urban sites than are those of Q_H. This corresponds well to the findings of Christen & Vogt (2004) and is also supported by Figure 3.3.

As described by Oke et al. (1999), the distribution of the heat flux densities in Mexico City is very different from those of a rural area. Fully 58% of total daytime net radiation goes into the storage heat flux density ΔQ_S and 38 % into the sensible heat flux density Q_H, leaving only about 5% for the latent heat flux density Q_E (also mentioned in Piringer et al., 2002; and Offerle et al., 2006). Although the geographic and climatic conditions of the City of Basel are completely different from those of Mexico City, the modification of the energy balance resulting from urban structures can also be seen clearly in the results of this study. The average percentage of $\Delta Q_S/Q^*$ is about 40% during daytime for the urban sites whereas it is only about 15 % for the rural ones according to Christen & Vogt (2004).

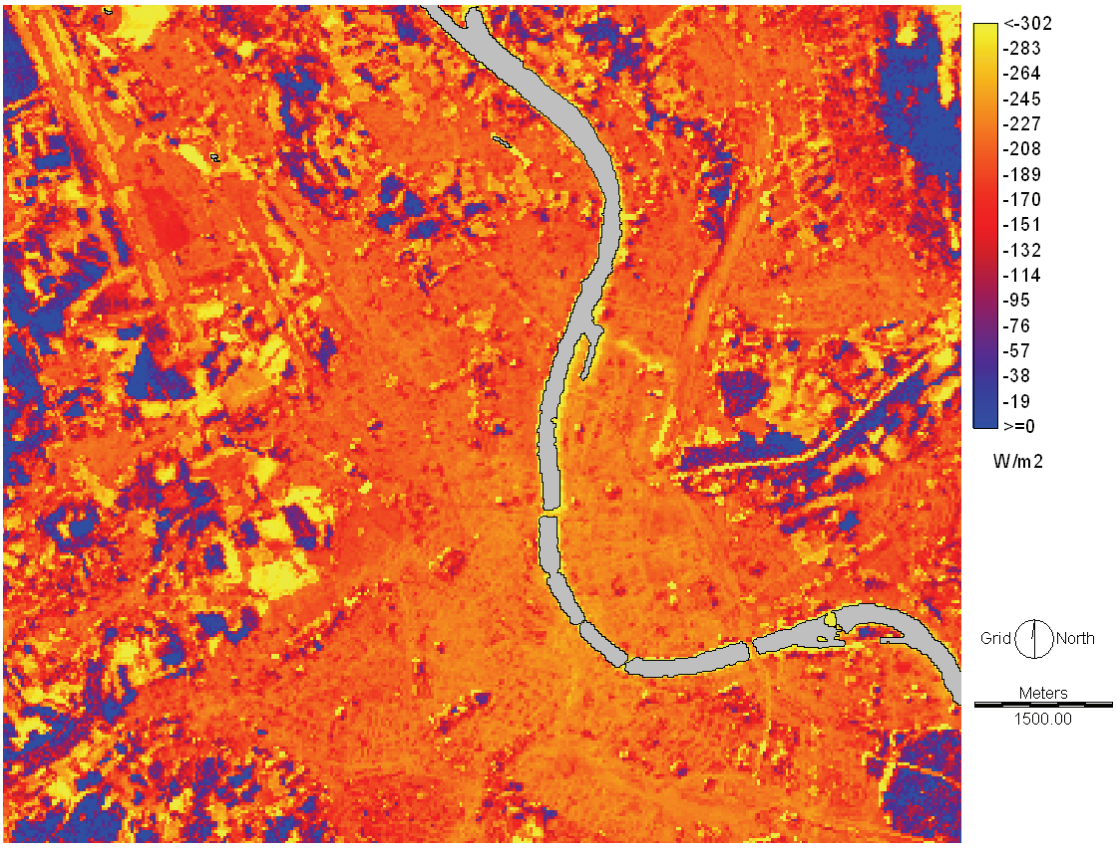

a)

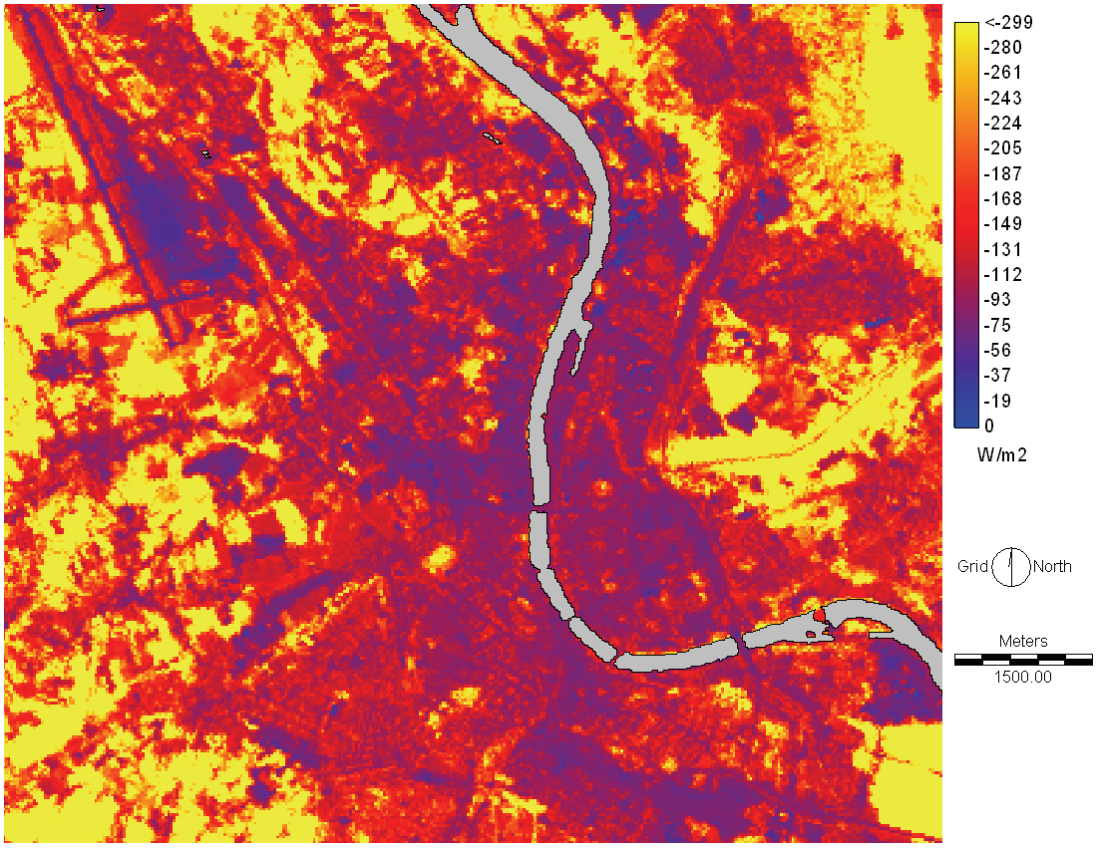

b)

Fig. 6.13: a) The Q_H distribution at the time of the LANDSAT ETM+ overpass (10.10 UTC) and b) the Q_E distribution. All values are in Wm^{-2}.

6.4.2 ASTER and post-BUBBLE

Although sensible (Q_H) and latent (Q_E) flux density data were unavailable for the 2003 overpass, either to test the objective of the thesis or to ensure reproducability of the model, the Bowen-Ratio/ NDVI was applied to the ASTER ΔQ_S scene. Therefore, a new regression was calculated with the ASTER NDVI and the following results were obtained.

At first glance, figures 6.14 a) and b) appear similar to 6.13 a) and b), although they appear somewhat sharper thanks to the 15m resolution of the ASTER albedo. If the values are analyzed, the results are in the range of the expected values. For Q_E, these are approximately -300 Wm^{-2} in the rural area and only approximately -100 Wm^{-2} in the densely built up urban area. The same can be said for Q_H, which was approximately -250 Wm^{-2} in the urban area, dropping to approximately -100 Wm^{-2} in the rural. Because no measurements were available from 2003 and the turbulent heat flux densities are not as stable over a given period of the year as is ΔQ_S no *in situ* data were available for validation.

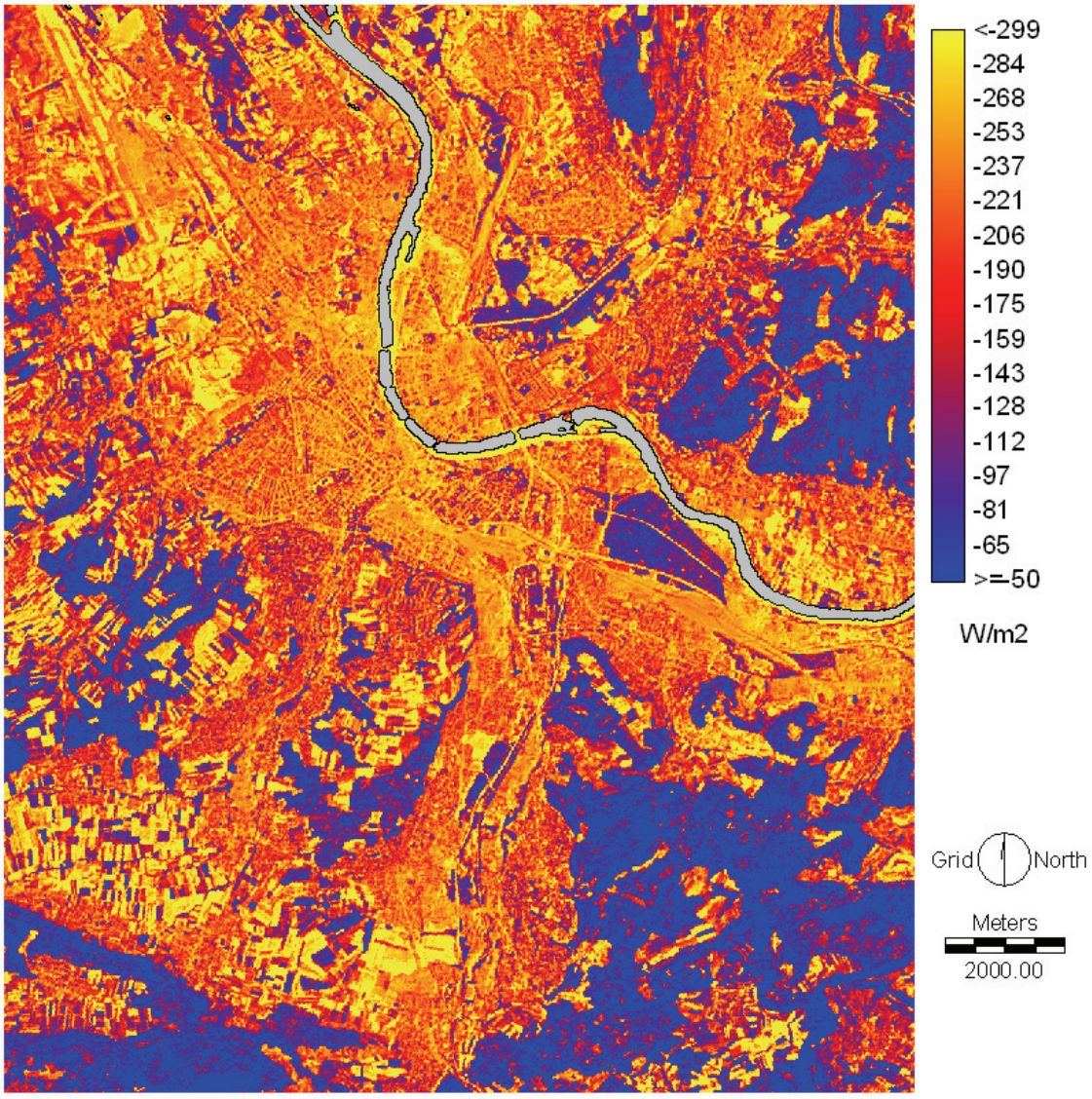

a)

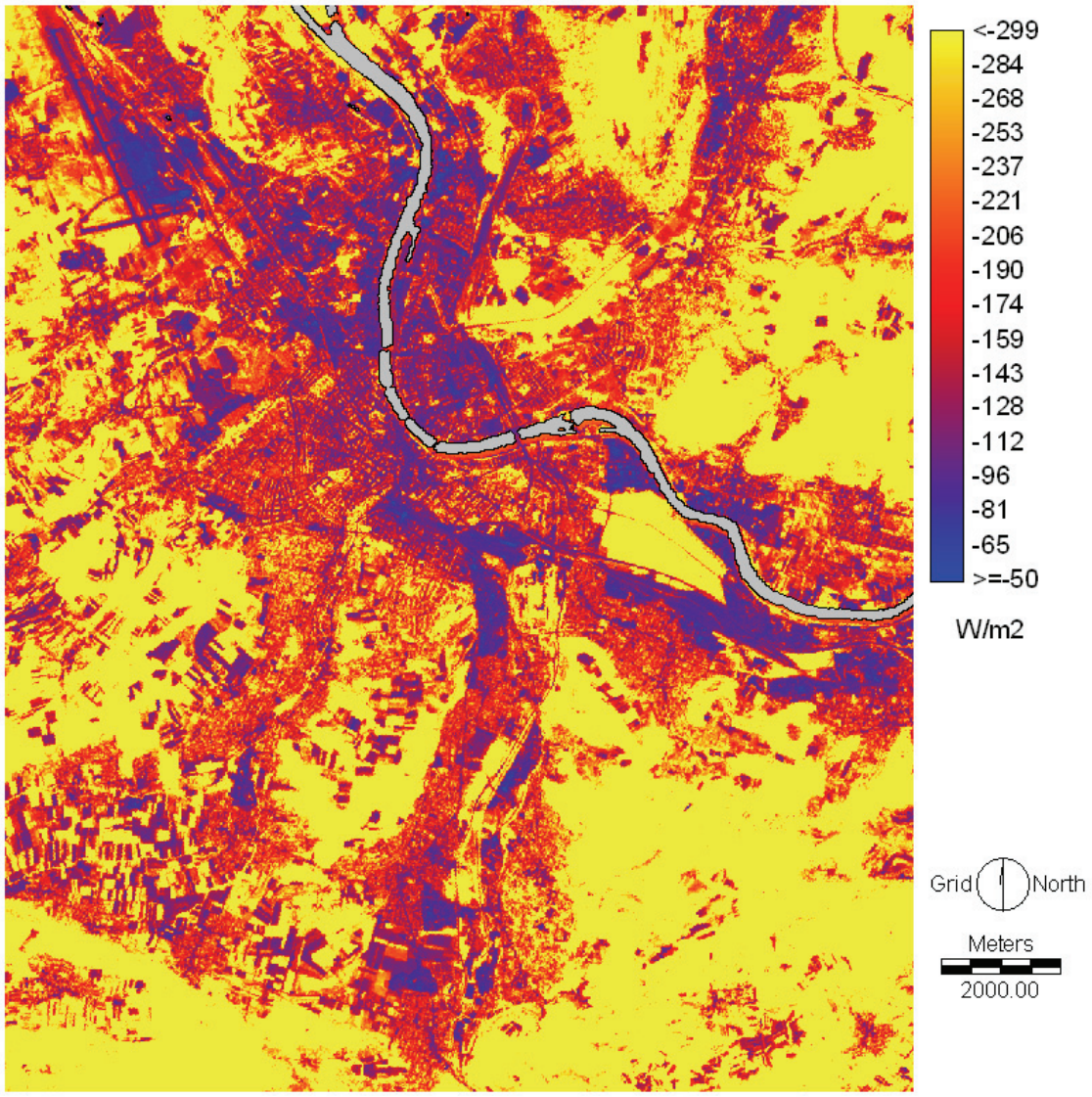

b)

Fig. 6.14: a) The sensible heat flux density (Q_H) in Wm^{-2} and b) the latent heat flux density (Q_E) in Wm^{-2} for the ASTER overpass August 5, 2003 at 10:30 UTC

The distribution of Q_H in Figure 6.14 a) is as expected and described by Christen & Vogt (2004), among others, with only small differences between the rural and urban areas. The same observation applies to Figure 3.3. Bare soil areas in the west and the airport in the northwest show the highest values, whereas, as expected, the forests show very low Q_H values.

For Q_E values, Figure 6.14 b) inverts the Q_H trend: forests and rural areas show the highest values, whereas those of urban areas, especially the airport and industrial areas, show very low values. This figure shows also that although Q_E is quite low over impervious surfaces, it is not equal to zero. The ASTER results from 2003 cover a larger area with more topographic features than those of BUBBLE and therefore enable a more detailed overview of the fluxes in the spatial domain. As the results supplied in Figure 6.14 show, the influence of topography on the turbulent heat flux densities is not measurable via the methods used here (see also Figure 5.2 for topography).

7. Discussion

7.1 Validation of the thermal IR data

7.1.1 Satellite Datasets

The results show a high correlation of different satellite LST to ground measurements even in an area as heterogeneous as the City of Basel. When compared to data from Kipp & Zonen datasheets, the results fall mostly within the manufacturers' listed 10 % accuracy of the pyrgeometers.

We also see in Fig. 6.2, that the diurnal course (measured with pyrgeometers) can be approximated and described quite well using various satellite based measurements and sensors. They show a typical diurnal course of longwave surface emittance over urban and rural surfaces. Most of the satellite data lie within the margin of 3% (accuracy of the calibrated pyrgeometers according to oral communications with Vogt), except for two scenes of the Sperrstrasse site. One is an AVHRR 16 overpass the morning of 7 July, 2002 when clouds obviously contaminate the pixel and also a later measurement with the AVHRR 15, approximately 10% below the *in situ* measured value, possibly because of cirrus clouds.

One would expect that rural sites, which are more homogeneous than urban ones (although there is no such thing as a pure pixel even in rural areas), would show higher correlations, but this is not the case. The differences are not related to whether sites are urban or rural. The coefficient of determination R^2 allows a more exact explanation. The R^2 figures differ not only from rural to urban sites but are also satellite dependent. Statistical analysis of rural sites results in an R^2 value of 0.84, and, for urban sites of 0.73. Results derived from AVHRR data correlate better with urban sites whereas MODIS data correlate better with rural sites.

The night scenes show much more consistent results than those recorded during daytime regarding mean absolute deviation (MAD): both MODIS showed MAD's of 5.4 % from measurement for daytime and 2.6 % for nighttime; AVHRR showed 4.3 % for daytime and 2.7 % for nighttime. All satellite data recorded from 5 a.m. to 8 p.m. UTC were counted as daytime overpasses, when shortwave downward radiation is greater than zero. The closer correlation is based on the fact that the surface radiation balance changes during the night (net radiation becomes negative after sunset) and therefore the thermal radiation flux densities or the LST can be calculated more precisely from satellite data. MODIS data show the best nighttime correlation with *in situ* data but daytime results are not as accurate as the AVHRR 14 data when the differences in percent are considered. There are several possible explanations for this result: Cloud contamination of the pixels could be one; on the other hand, the MODIS (Terra) was launched in December 1999 and the algorithms are still being improved, whereas the algorithms for the AVHRR 14 have been tested and improved many times over a longer period.

As for the different split-window algorithms, all three AVHRR satellites yielded greater accuracy with Becker & Li (1990) and Price (1984) with, respectively, 3.5 % and 3.7 % average differences, followed by Sobrino et al. (1994) (4%) and Ulivieri et al. (1992) (5.2%). Becker & Li (1990) showed particularly strong correlation over all the AVHRR scenes when compared to *in situ* measurements. Sobrino et al. (1994) also showed a good correlation, with only 0.5 % higher difference on average than Becker & Li (1990); nevertheless, Becker & Li (1990) or Price (1984) are the strongest recommendation and were also used with the datasets from 2003. It must be noted that the three AVHRR sensors differed in accuracy with AVHRR 14 yielding the most consistent results. The AVHRR 15 showed the highest differences for all the satellites, which can be attributed to the

observed degradation of its data quality (since April 2001) and problems with its scan motor (Oesch, 2005). Its thermal data were still useful, but as the results show it was outperformed by its sister satellites. These findings of the different AVHRR's seem to be confirmed by the smaller dataset of 2003. As for the AVHRR 14, the calibration coefficients had been improved many times during its duty-cycle since its launch in 1994 to compensate for the sensor degradation (Rao & Chen, 1999; Tahnk & Coakley, 2001). Although the mentioned factors applied only to channels 1 and 2, they influenced the longwave channels because the emissivity was derived from them. This was one reason for the strong performance of AVHRR 14. AVHRR 16 was one of the newest satellites of the AVHRR-program and was launched in 2000.

Therefore its good results are explicable by considering its relatively short time in space, where calibration constants and algorithms could still be improved but sensor degradation was practically nonexistent over such a short period of service and the satellite was equipped with state of the art measurement equipment. It is also significant that most research has been conducted using AVHRR 14 data in recent years and there is very little published research based on the AVHRR 15 or 16 thermal channels, all of which makes comparisons difficult. To access more accurate results and to make a recommendation for one or more of the AVHRR satellites a long-term monitoring would be necessary. This task would be complicated by the problems which have affected the the AVHRR's in recent years (scan motor failures on AVHRR 14 and 16, together with phases of unusable imagery due to bar coding and deteriorating image quality (see NOAA Office of Satellite Operations http://www.oso.noaa.gov/ for details) even with the latest AVHRR 17 and 18 in orbit. Unfortunately, according to various authors (Gleason et al., 2002; Gutman, 1999; Jin & Treadon, 2003; Price, 1991), the AVHRR satellites (especially those launched prior to AVHRR-14) are affected by a temporal drift in their orbit which causes the equator crossing time to shift over the years. Since the AVHRR 16, a special technical effort has been made to stabilize the orbits of the forthcoming AVHRR satellites. According to Jin & Treadon (2003) the orbits of AVHRR 15 and 16 have changed very little since their launch (less than 30min) whereas at the AVHRR 14 it shows a 3 hour difference in its equator passing time, which has shifted from 2 p.m. to 5 p.m. While this shift affects long-term monitoring of LST due to the changed overpass times, it was not an issue for this study because the complete daily radiation and temperature measurements were used during the IOP. The varying overpass times are even desirable for best multi-temporal daily coverage. On the other hand, overpass times around dawn and sunset are the most difficult, because the algorithms are not designed for this time of day and cloud masking is also more difficult to compensate for than at high sun angles. This is especially the case for AVHRR 15.

Generally for all the AVHRR platforms differences between satellite and *in situ* data are to be expected, because every algorithm was originally developed for a specific AVHRR sensor (Price (1984) and Ulivieri et al. (1992) for the AVHRR 7, Becker & Li (1990) for the AVHRR 9 and Prata & Platt (1991), Sobrino et al. (1993) and (1994) for the AVHRR 11) and surface condition, which was also generally rural, whereas this study concentrated on non-homogeneous urban surfaces. Therefore, even if the absolute thermal calibration was correct and corrected fully for sensor degradation, the function and sensitivity of the sensors would be different between the AVHRR platforms (see also NOAA KLM Users Guide).

As for the LST temperature differences (in K) for LANDSAT 4 and 5 datasets Goetz (1997) reported an RMSE of 2.7 K after calibration when compared to *in situ* data from infrared thermometers (IRT). Although the number of samples in this study is less than in Goetz (1997), it shows clearly the impact of the improvement of the LANDSAT ETM+ thermal sensor on the accuracy of its measurements. This is also confirmed by Li et al. (2004), who showed a RMSE of 1.0 K for LANDSAT ETM+ and

1.8 K for LANDSAT 5. These results correspond well with the findings from Li et al. (2004), Petitcolin & Vermote (2002) and Wan et al. (2002), which showed results in the same range for MODIS and LANDSAT ETM+ data. The discrepancy for the AVHRR's between surface temperature in K and the longwave upward radiation was observable because the split window algorithms were developed for specific AVHRR satellites and Czajkowski et al. (1998) found an error of up to 2.3 K if the algorithm was applied to other AVHRR platforms. Therefore the differences here were in roughly the same range but the validation was conducted over a non-homogeneous urban surface and multiple sites. Another source of error with the calibration was the dependency between the different algorithms regarding emissivity. Kerenyi & Putsay (2000) showed that such differences are highly dependent on surface emissivity. They calculated a bias of greater than 4 K with all the compared algorithms except that of Price (1984), which was below 2 K. Vazquez at al. (1997) and Han et al. (2004) show how changes as slight as 1 % in emissivity can change the LST up to 2 K, depending on the split window algorithm used.. Other results from Vazquez et al. (1997) show similar correlation of *in situ* and remotely sensed data with an RMSE of 1.9 K for Ulivieri et al. (1992), 2.3 K for Price (1984), 3.0 K for Prata & Platt (1991), and 3.8 K for Becker & Li (1990). Another analysis made by Han et al. (2004) over boreal surfaces showed accuracies of 2.2 K for Becker & Li (1990), 2.6 K for Price (1984) and 4.1 K for Prata & Platt (1991) but they derived the *in situ* values from the air temperature, which is also a source of error not to be overlooked. The general accuracy for most AVHRR split-window algorithms is approximately 3 K according to Ouaidrari et al. (2002) for land surfaces. Accuracies of less than 1 K can only be achieved for mostly homogeneous test sites with more advanced sensors such as MODIS (Li et al., 2004; Petitcolin & Vermote, 2002; Wan et al., 2002). Results on LST by Petitcolin & Vermote (2002) and Wan et al. (2002) show that MODIS data have an accuracy of about 1 K when compared to ground based measurements in homogeneous rural regions with known emissivity. This is about 1.5% if we take an average temperature around 300K. Validation of the MODIS LST product by Coll et al. (2005) show even better accuracy for the MODIS datasets over a homogeneous rice field. Jacob et al. (2004) showed for MODIS and ASTER an accuracy of 0.9 K between the two datasets when the ASTER images are contracted to the resolution of the MODIS datasets.

Even using the most reliable and the latest methods to derive emissivity from satellite data, a source of error still remains. As denoted by Dash et al (2002) different methods exist for the emissivity estimation and the different methods were applied to the respective satellite datasets in this thesis ensuring a high accuracy between *in situ* and satellite derived data. Nevertheless even with the most accurate algorithms and MODTRAN the error induced by atmospheric effects is up to 0.7 K for every sensor and the uncertainty in emissivity accounts for another error of up to 0.4 K. This makes it according Jimenez-Munoz & Sobrino (2006) extremely difficult to achieve accuracy below 0.8 K even in homogeneous rural environments single band satellites like LANDSAT ETM+.

As for the 2003 data, there are only few publications concerning the accuracy of the ASTER thermal datasets which makes a comparison of the results hereby more difficult. Both MODIS satellites performed well in 2003, but after the validation it seemed that MODIS AQUA outperforms TERRA slightly in accuracy (see Table 6.3). Nevertheless this result has to be looked at with caution due to the limited database of this finding with N=21 for MODIS AQUA and N=18 for MODIS TERRA.

These additional results from 2003 show, that the overall performance of the MODIS sensors is not necessarily superior to the AVHRR's during daytime. The higher differences during BUBBLE can be blamed more on cloud contamination than on the algorithm although the dataset from 2003 is based only on three *in situ* measurement sites.

7.1.2 VarioCam thermal data

Acquiring high resolution thermal data proved to be very difficult in itself. As mentioned above, the merging and mosaicking of the VarioCam datasets is a source of error; nevertheless, the thermal image provides a picture of the city in a spatial resolution unseen before now. As shown in Figures 6.4 and 6.5 the difficulties with surface temperatures in cities result from the structures of the urban canyons, which make it impossible to acquire the "complete" surface temperature (Voogt & Oke; 1997 and 1998). The possibility of transecting the image with the help of the DCEM makes this flaw more obvious: due to the almost straight near-nadir viewing camera angle, the VarioCam recorded no data for the walls.

One interesting point relates to Figure 6.5 d), the north part floor measurement (point no. 5), is higher than that of the lower south facing wall or the south part floor temperature. This was always higher than it neighbours during the BUBBLE-IOP while the weather was fair at the time of recording (10:45 to 11:10 UTC). The explanation can be given with the help of a set of thermal images (Figure 7.1) taken with an AGEMA thermovision 900 SW-TE (Pfändler, 2003).

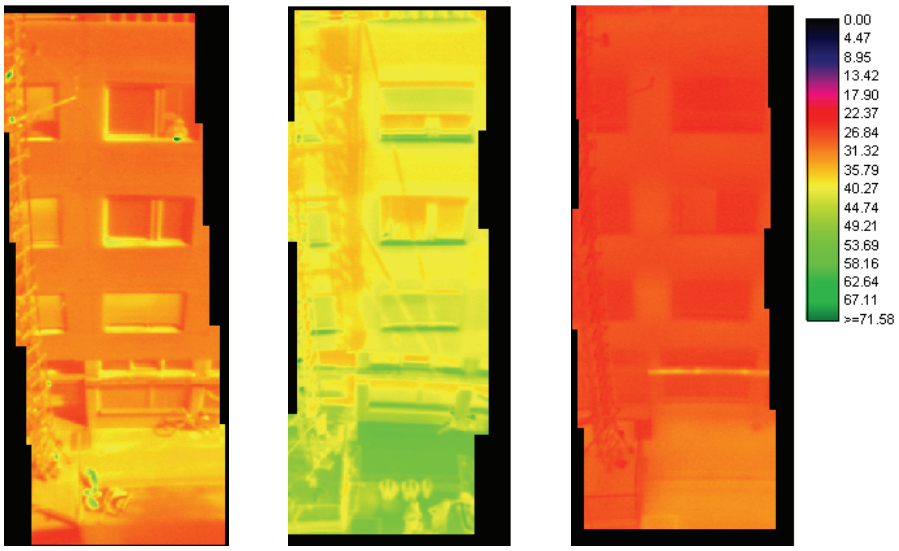

Fig. 7.1 : Thermal infrared images of the south facing street canyon wall (in degrees Celsius) taken at 07.30, 11.30 and 21.30 hours (UTC) (July 8, 2002) at Sperrstrasse (courtesy S. Pfaendler)

Although the images were not taken at exactly the same time (although all are from the BUBBLE - IOP) it can be seen in Figure 7.1 a) that the lower part of the wall and the north part of the road show a much higher temperature than the south half of the road. Pfändler (2003) also notes that the 1st floor wall and the pavement become the hottest and are also the first to reach their maximum temperature. This is in full accordance with Figure 6.5 d), but Figures 6.5 a), b) and c) show no indication of this important point. During daytime, because of combination of the incoming solar radiation and the cooling effect of the rooftop wind field on the temperatures on the upper floors, the road temperature rises much more than that of the walls (Figure 7.1 b)). During the night, the walls cool down much faster than the road (Figure 7.1 c)) virtually no net difference remains between the floors (noted by Pfändler (2003)).

These images illustrate the problems facing researchers who depend not only on airborne (and spaceborne) thermal but also on any type of optical imaging in an urban environment. Even the most sophisticated instruments allow some errors in the *in situ* measurements; in addition, even high resolution thermal data still cannot solve the urban anisotropy without complex recording patterns and optimized measurement angles.

7.2 Net radiation

7.2.1 BUBBLE-IOP

The average net radiation figures showed a high correlation with the values measured *in situ.* Over the rural sites, agreement with *in situ* measurement is much higher than over the urban sites. The most problematic of the sites was the Messe location (U3), the satellite data for which, compared with *in situ* readings, shows extremely high differences leading to consistent overestimation of the net radiation during daytime. Similar, though less pronounced findings are also valid for the Lange Erlen site (R3). The remaining rural and urban sites show approximately the same mean absolute differences, except for U2, which has a higher RMSE. Equation 3.7 and Figure 3.2 provide useful tools for the explication of these results. The short-wave part of the radiation balance has the highest impact on the net radiation, especially the Q_{SU}, which is dependent on the broadband albedo α during daytime.

The *in situ*/modelled data differences for rural sites R1, R2 and R4 lie within the expected accuracy, as described by Kustas et al. (2004), who note an RMSE of 29 Wm^{-2} for a rural site. Ma (2003) mentions a mean absolute difference of 5% between modelled and measured Q*, which corresponds to absolute values between 15 Wm^{-2} (for Q*=300Wm^{-2}) and 35Wm^{-2} (Q*= 750Wm^{-2}). The Two-Source Energy Balance Model (TSEB) of French et al. (2005) also yield data with a mean difference of 31 Wm^{-2} for the Q*. These results show that, regardless of the kind of model used, it is difficult to model Q* even over a rural surface.

The higher mean absolute differences of the urban sites can be explained with reference to the albedo of the urban area. As mentioned by Kondo et al. (2001) the urban surface has a great influence on the area's albedo. However, this influence cannot be registered correctly by the satellite sensor, due to its low spatial resolution, which makes the albedo less accurate. Especially for U3, the albedo problem also occurs due to the mixed pixel problem; therefore, U3 shows the greatest differences of all the sites. A comparable result was achieved by Lemonsu et al. (2004) for the City of Marseille in a temporal approach using the Town Energy Balance (TEB) scheme to model the net radiation: this showed a bias of 20 Wm^{-2} during daytime, with an RMSE of 37 Wm^{-2}. As for R3, which is situated between barren soil and grassland, the albedo is also the key, because it changed while the crops and grass grew during the IOP.

This development shows another implication for the albedo. The albedo changes not only during the day according to solar angle and inclination, but also according to the time of the year – and, as illustrated above, due not only to seasonal changes in the solar angle, but to changes in foliage and ground cover as well. Although here the albedo was acquired from actual satellite data it still cannot easily capture the dynamic nature of the albedo. If albedo from AVHRR or MODIS had been used the results would have been less consistent still, due to the much lower spatial resolutions of these platforms. Therefore, a high resolution dataset from ASTER or LANDSAT ETM+ is needed for albedo assessment.

For nighttime images, where no additional shortwave radiation was needed and Q* consisted of longwave radiation only, the accuracy of the results was highest by a considerable margin (see also Figure 6.6). This supports the dependence of Q* from the albedo α.

7.2.2 ASTER data

The results for Q* (for daytime overpasses) showed a MAD of 22 Wm^{-2} with an RMSE of 13 Wm^{-2} in 2003, which were slightly higher than for all the 2003 scenes. These figures seem very reliable when compared to the BUBBLE results. Nevertheless there are some factors responsible for this: First, although ASTER is quite new, the albedo algorithm of Liang et al (2003) was more accurate than the regression based approach used for the LANDSAT ETM+. The data from the visible and near infrared channels included in eq. 5.3 are partially in 15 m resolution, meaning that the spatial accuracy of the albedo was somewhat higher than that of the LANDSAT ETM+.

Other factors were:

- The database used for validation. Only three sites were available for validation instead of the original eight, which led to a smaller amount of available data.
- The use of only one urban site (Klingelbergstrasse), which decreased the number of errors expected.
- The rarity of publications focussing on ASTER and net radiation, making a comparison of the data difficult. Chrysoulakis (2003) modelled ASTER data for Athens and achieved an accuracy of ±44 Wm^{-2} for daytime imagery.

7.2.3 Net radiation from very high resolution data

The net radiation shown in Figure 6.8 is different from that in Figure 6.7, showing higher net radiation in the vegetated urban areas and lower ones in the densely built up environments. This seems to contradict the observation by Christen (2005) that net radiation in urban and rural environments during BUBBLE seemed almost equal.

The explanation relates partly to the spatial resolution of the datasets themselves. In a 15m or even 30m per pixel image, there is no distinction between a roof, a street or a tree, whereas in 1m per pixel resolution these details can be distinguished clearly. In addition, as the spatial resolution increases, the urban canyons themselves become more influential (in a 15m resolution very little of an urban canyon can be distinguished). As stated by Harman et al. (2004) or Kondo et al. (2001) the structure of an urban canyon itself modifies the radiation flux densities depending on sky-view factor and / or other specific building properties. Considering the extreme difficulty of modelling even in small scale "optimized" areas, and given the type of remotely sensed data available, it is currently impossible to incorporate such factors reliably into a modelling algorithm (Voogt & Oke 1997).

There is also another explanation for the results. The Quickbird imagery, which was recorded February 2, 2002, is the source for the albedo, the key factor in the radiation balance equation. The trees and vegetation are largely leafless in February and show a much lower albedo (between 8% and 12%) than would be the case in summer (20% and more) when the other images were acquired. Therefore, the incoming shortwave radiation (Q_{SD}) is reflected less by the vegetation than by the impervious surfaces, which generally have a year-round albedo between 12% and 20%, with higher figures still for sun exposed sides and bright surfaces (approximately 40%). In addition, while the trees clearly have a lower long wave upward radiation $Q_{LU,}$ their long wave downward radiation value (Q_{LD}) is similar to that of impervious surfaces. Because the vegetated areas receive a higher shortwave input and emit a lower long wave output, these areas show a generally much higher net radiation (Q*) than impervious surfaces. The difficulty in modelling net radiation with high resolution data is therefore linked to the available albedo for the overflight time. In the case described above, although the longwave radiation was read in summer, the albedo of the vegetation from a winter overpass makes the results more suitable for a winter day than a summer one when vegetation would be in full bloom.

7.3 Storage heat flux density

7.3.1 CAR

The results of the CAR approach are limited by the fact that the available data only covers the built-up areas of the City of Basel. The results for the urban Sperrstrasse (U1) and Spalenring (U2) sites are similar to the values obtained from the other models (differences between 1 Wm^{-2} and 32 Wm^{-2}), but the Messe (U3) site shows far higher differences (100 Wm^{-2} on average).

Several explanations are possible for such an extreme difference. First, the Messe site was located on the roof of a car park: When the calculation of the complete aspect ratio from the sky view factor was applied, the resolution was diminished to 30 m instead of the original 1 m. Therefore the roof shows an aspect ratio of approximately 1, which qualifies it as an open space, where the aspect ratio is exactly 1. Since the aspect ratio for areas with vegetation is taken as equal to that of an open space, the result shows a ground heat flux density typical for vegetated areas such as the Lange Erlen or Grenzach sites. This explains the high degree of difference, while showing that on open sites without vegetation the CAR model is not particularly useful. The averaged values of the surroundings may approach the rural measured values (see Table 6.3), but in high density areas, which have a high complete aspect ratio, the results are more comparable.

Another problem with the CAR approach is the fact that, although the net radiation can be modelled and measured with acceptable accuracy, the closure of the energy balance ($\Delta Q_S + Q_E + Q_H = Q^*$) is simply not given for each hour (see also Christen 2005). Therefore, the net radiation during nighttime can be lower than only the storage heat flux density ΔQ_S itself. The application of the CAR model to nighttime or morning data is therefore difficult and makes valid calculations possible only between 10h and 16h CET. The CAR approach from 2003 with ASTER shows similar results again, with U3 showing the greatest differences. While this shows the applicability of the CAR model to other datasets for about the same time of day, the CAR model nevertheless needs to be applied to 3-D datasets from other cities for more rigorous evaluations.

7.3.2 NDVI

For the NDVI approach, as shown in Table 6.7, the spatial resolution of the thermal data is not particularly important. The differences between the modelled LANDSAT ETM+ and MODIS derived ground heat flux densities are minimal but the differences arising from the Lange Erlen site (R3) are far too high when compared to the other sites. Even the Spalenring (U2) site shows acceptable agreement, with an average difference of 25 Wm^{-2}. The reason is difficult to determine, since the calculation with a MODIS derived Q* image showed almost the same results when the 16-day MODIS average NDVI was used.

One explanation could be that the NDVI over R3 was different during the overpass time than the average ground heat flux density would suggest, especially when it overestimates the *in situ* measured values. The NDVI also changes during the season, while the soil moisture sometimes also influences the NDVI values. In general, the NDVI approach is still the simplest of the three compared approaches to use, and requires the least data for acceptable to good results. Unfortunately, it is limited to daytime computation only, due to its dependency on the NDVI or other vegetation indices, which can be calculated for daytime images only. For the 2003 ASTER dataset, the NDVI approach was not used because eq. 5.7 and 5.8 were only validated for LANDSAT ETM+ derived NDVI and gave incorrect results in a test run when they were applied to ASTER data from 2003. This also shows the limitations of the NDVI approach.

7.3.3 OHM

The most promising of the three approaches compared is the OHM-approach, with an R^2 of 0.95, an overall RMSE of 13 Wm^{-2}, and a mean absolute difference (MAD) of 17 Wm^{-2} (even when the Messe site is included) indicating its accuracy. The rural sites perform better than the urban ones but not strikingly. Nevertheless, as also mentioned by Weber (2006), the *in situ* measurement with heat flux plates is still more accurate than with eddy covariance over urban sites. The OHM modelled values mostly overestimate the *in situ* datasets during daytime and underestimate them during nighttime. Higher accuracy with the nighttime imagery is important because the values of the storage heat flux density after dark are much lower than during daytime.

Using the OHM approach with MODIS daytime imagery, most problems with the storage heat flux density at the Messe site arise and the difference is above 70 Wm^{-2}. Since the site is situated on a car park, the big differences with the MODIS OHM approach could be connected with its far coarser spatial resolution of 1km, where smaller extreme local values cannot be detected so accurately. Because the values for U1 and R2 are also much higher than average, this explication is not sufficient. Instead, it is likely that the source of error is the Q* for the MODIS overpass, which is backed up when one looks at the results of Q* for the MODIS daytime scene. This example shows how important an exact modelling of the net all wave radiation Q* is for a successful OHM model application to model the storage heat flux density. For the Lange Erlen site, even with the MODIS daytime overpass it is remarkable that the differences are the lowest of all sites, but there the Q* values are also acceptably accurate.

Greater accuracy during nighttime seems reasonable and minimizes the relative differences. If there is only a short time between two satellite overpasses (especially in the late morning hours (9h to 11h CET) and less than an hour difference) the OHM model strongly underestimates the urban flux densities, whereas for the rural ones the differences are in the usual range. This can be explained with a quick change of ΔQ_S in this time at the urban sites to which the model has some difficulties to adapt, whereas, at the rural sites, the changes are much smaller and therefore the OHM model can keep up with the change.

The application of the OHM to the 2003 datasets was very successful. The results were even more consistent than they were for BUBBLE, showing a tighter range of differences between modelled and measured values. The rural sites still showed greater accuracy than the urban ones, which confirms the findings of 2002. These results have to be analysed with care, however: due to the unavailability of data from 2003 the *in situ* average values from BUBBLE were used for validation purposes. The averaged storage heat flux density from 2002 still yields a value very near what is predictable as a typical summertime average; therefore, the results remain a very accurate approximation of the expectable real values.

7.3.4 Overall

The composite results of all approaches showed a MAD of approximately 17 Wm^{-2} (except the Messe site, U3), with only slight difference between the approaches. Differences between urban or rural sites were present in 2003 but to a lesser extent than during the BUBBLE campaign. When the OHM is used for nighttime overpasses, generally the model results mainly in overestimated ΔQ_S, whereas for the daytime, the model seems to underestimate the site values.

The results are in good agreement, because the measurement of the ground heat flux density is still a difficult task: depending on the method used (heat flux plate or calculation with eddy covariance from Sonic-anemometer measurements), even the measurements have an operational error of more than

15%, (Weber (2006) or Twine et al (2000)). Kustas et al. (1995) with their two layer turbulent, and therefore more complicated model, showed a difference of 35 Wm^{-2} for the ground heat flux density. Kustas et al. (2004), with their two-source model approach, still showed average differences between 21 Wm^{-2} and 32 Wm^{-2}, with modelled LANDSAT TM and LANDSAT ETM+ data for the ground heat flux densities over farmland in Iowa. All these results demonstrate how difficult it is to assess turbulent heat fluxes with high accuracy.

7.4 Turbulent heat flux densities

Regarding the remote sensing imagery, there is a clear relationship between the Bowen ratio and the NDVI. The NDVI / Bowen-Ratio approach used here shows very promising and consistent results for daytime turbulent heat flux densities (its dependency on the NDVI makes it unusable for nighttime imagery). Daytime Bowen Ratio values also differ strongly from nighttime ones (Christen and Vogt, 2004). Therefore, this Bowen Ratio/NDVI approach is limited to use with daytime images and can only be used if the storage heat flux ΔQ_S has been modelled in advance. Also, while the closing of the energy balance is assumed, this is not completely true (Christen & Vogt, 2004; Oke, 1990) and could therefore be a source of error, together with the omitted anthropogenic heat flux Q_F.

The NDVI is also dependent on soil moisture and therefore on precipitation. The amount of precipitation in the test area was approximately 55 l/m^2 in the week before June 25, 2002 and approximately 13 l/m^2 in the week before July 8, 2002 – of which roughly 8 l/m^2 fell July 6, 2002. This means that the surface was never completely dry before the satellite overpass and therefore enough water was available for evapotranspiration or Q_E respectively.

The mean difference for the modelled Q_H is 25 Wm^{-2} and, for Q_E, 46 Wm^{-2}, with RMSE's of 19 Wm^{-2} and 39 Wm^{-2} respectively. For Q_E the differences are more pronounced at the rural sites; for Q_H, urban sites show slightly higher differences. The accuracy achieved using this approach is quite good when compared to results from Kustas et al. (2004) (with an RMSE of 26 Wm^{-2} for Q_H and 38 Wm^{-2} for Q_E) or French et al. (2005) both of which report similar difference ranges over homogeneous surfaces, whereas we deal here with different land use and surface heterogeneity. Anderson et al. (1997) reported an RMSE of above 50 Wm^{-2} with TSTIM (Two Source Time Integrated Model), as well as a mean difference of 45 Wm^{-2} for Q_H and Q_E. Jiang & Islam (2003) also compared results from two different models, one of which was also based on a modified NDVI input parameter, and also achieved, for Q_E, an RMSE of approximately 60 Wm^{-2}, along with a bias of approximately 40 Wm^{-2}.

As an example of a local scale non-remote sensing model, the results of Mestayer et al. (2005) for the UBL/CLU-ESCOMPTE, using the TEB (Town Energy Balance) Model, also show an RMSE greater than 40 Wm^{-2} for Q_E and greater than 60 Wm^{-2} for Q_H and ΔQ_S, while the biases are below 20 Wm^{-2}.

The results of Q_E and Q_H in 2003 differ slightly from those calculated using the BUBBLE datasets. Even without the possibility of validating the results, however, they appear reasonable. Due to the fact that the NDVI / Bowen Ratio correlation was calculated with the specific ASTER NDVI, the results differ little from those of 2002. The distribution of the flux densities could be different because of the weather conditions in Europe in the summer of 2003. From July 21 to July31, 2003, precipitation (total amount of 55 mm/m^2) was recorded for six dates, meaning that the soil and vegetation had some water to evaporate over the following days; therefore, although the summer of 2003 was very dry, especially in August, the data for late July are similar to those collected in 2002. If Figure 6.14 is compared to Figure 6.13 and Figure 3.3 it is clear that the values therein are fully plausible and within a reasonable range.

Generally the higher spatial resolution of the albedo from ASTER appears to improve the accuracy of the net radiation value. At the same time, the higher resolution of the NDVI enables a clearer image of the spatial distribution of the heat flux densities, although the thermal-IR bands have a lower resolution than the LANDSAT ETM+ (90 m instead of 60 m).

This model also struggles with the problem of modelling Q_E, which shows a higher bias than Q_H, especially over rural areas. The evapotranspiration and storage of water in plants is a complex process,

depending on water availability, water stress, recency of rainfall, etc. These factors cannot be observed in detail when working with average measured Q_E; the limitation is even greater with a momentary satellite image. Nevertheless, the modelled values provide the basis for a reasonable estimation of the values and distribution in the spatial domain, while working well for an urban surface, which were the primary goals of this model and work.

Although the approach used herein is quite simple and is based on the Bowen Ratio, it still requires a very exact *in situ* measurement network for measuring and calculating the necessary heat flux densities, either with an eddy-covariance approach or combined with a heat flux plate. The Bowen Ratio/NDVI approach is a very simple model. For different research areas, however, the relationship has to be calculated anew: this also applies to the time of year, which, as noted above, has various effects on the NDVI. On the other hand, the crucial validation of the source data with *in situ* data – starting with longwave upward radiation (see Rigo et al., 2006), followed by net radiation and the computation and modelling of ground heat flux densities (see Rigo & Parlow) – enables the modelling of the energy balance components in a spatial distribution based on reliable basic datasets.

The spatial visualization of these observations is very important to access the "energetical structure" of a city. Due to limited data availability, however, application is only possible in the medium to high resolution domain. Another important factor is the uniqueness of every urban area's structure, which means that comparisons with data from other cities are limited in value, and can be made only with caution. The urban structure itself (especially the urban street canyon) is one of the important objects of urban climatological research (Soux et al. 2004; Voogt & Oke, 1997), and plays an important role in the modification of a city's energy balance. With medium to high resolution (1km – 15m) remote sensing datasets, these factors cannot be clearly observed, due to the extreme heterogeneity of the urban surface and the insufficient resolution of the satellite datasets. Therefore, although these factors play an important role (as illustrated above in the discussion of high resolution data) they were omitted from this approach.

High resolution data, on the other hand, is more difficult to work with, because the small scale processes it records take place in the urban canyons, thereby modifying the properties of those canyons. This highlights the need to incorporate such processes into a model for the calculation of radiation and energy balances at higher spatial resolutions. The problem with the walls and therefore with the three-dimensionality of an urban street canyon remains, even if models such as that of Soux et al. (2004) can solve it for an idealized surface.

8. Conclusions

8.1 Thermal datasets

Even considering the possible sources of error discussed above, the results presented herein are very usable and sufficiently accurate for further processing of the data. They show a high correlation, with an accuracy range of below 5% with *in situ* measurements, and demonstrate that satellite data are suitable for computing long wave surface radiation flux densities in the spatial dimension – even for urban areas –with little dependence on the spatial resolution of the sensors. The coarser spatial but higher temporal resolution of MODIS and AVHRR sensors made it possible to simulate a diurnal variation of the surface long wave emission, whereas the higher spatial resolutions of LANDSAT ETM+ and ASTER helped to distinguish urban surface features. In conjunction with *in situ* derived data, which can also be used for validation and accuracy assessment., LANDSAT ETM+, as well as AVHRR, MODIS and ASTER data were therefore well suited for further processing and modelling of the spatially distributed net radiation and heat flux densities.

Many publications (Czajkowski et al., 1998; Han et al., (2004); Kerenyi & Putsay, 2000; Ouaidrari et al., 2002; Vazquez et al., 1997) show that the algorithms of Price (1984) and Becker & Li (1990) are generally the most applicable (as was also found in this thesis), making them recommendable for further use and application. Nevertheless, the results also illustrate that validation and comparison of the different split-window algorithms is strongly dependent on the location of the sites, data processing method, land surface type, climate characteristics and the source of *in situ* data. On the other hand, without exact atmospheric profiles or *in situ* emissivity measurements, the main sources of error are atmospheric correction, the BRDF and the emissivity, all of which combine to produce an uncertainty of approximately ±1K. Therefore, the evaluations and validations are only valid for specific conditions and research areas, and are not directly transferable to other research sites.

8.2 Net radiation

The net radiation was modelled in the spatial domain with reasonable accuracy for an urban area when compared to results from other authors. The step by step approach used with SWIM can be applied to other research areas, but only if the necessary input parameters are available. The findings from the BUBBLE *in situ* measurements were confirmed, showing that the city actually has a lower net radiation than its surroundings (Christen & Vogt, 2004; Oke 1990).

The very high resolution image, although strictly experimental due to its nature (e.g., no atmospheric correction or overall emissivity measurement), showed, nevertheless, the extent to which, depending on the season, a vegetated area in an urban environment could change the net radiation and therefore the energy balance in a city. These findings would not have been possible with a data resolution limited to 30 m pixel resolution (“high resolution”), which supports the thesis that, in addition to the longwave outgoing radiation and evapotranspiration, the broadband albedo plays a role in the development of urban climates as shown by Kondo et al. (2001). Even with access to very high resolution data, however, modelling the albedo of an urban environment remains problematic.

8.3 Ground heat flux density

All of the three approaches (Complete Aspect Ratio (CAR), NDVI and Objective Hysteresis Model (OHM)) yielded results that corresponded with the measured values. Considering that, even with *in situ* instrumentation, measuring the ground heat flux density with great accuracy is difficult in rural sites, and even more so in urban ones, the results reported here can be considered quite accurate.

The CAR-approach is limited to urban canyons, but can easily be derived from high resolution digital elevation data, since only the complete aspect ratio must be calculated. Of the three approaches presented, the CAR approach is the least useful, even with an adjusted hysteresis curve, and is far inferior to the OHM approach, which also uses a hysteresis curve for its modelling. The most significant sources of error using the CAR approach are the dependency on *f,* and, as shown by Christen & Vogt (2004), the difficulties in using it to model nighttime storage heat flux density.

The NDVI approach requires additional information from remotely sensed imagery (Q*). For the given overpass time – between 10h and 15h local time (UTC +2 with daylight saving time in Central Europe) – the NDVI approach is very suitable, yields good results and is easy to use. However, for greatest flexibility, it should be used with at least 60m resolution data. NDVI from AVHRR or MODIS (16 Day average) are less accurate due to their lower spatial and temporal resolutions.

The OHM approach does not yield fully accurate modelling of the storage or ground heat flux densities, but does give an approximation of the spatial distribution of the ground heat flux density within a range of ±20 Wm^{-2}, which is quite accurate and makes further partitioning of the heat flux densities possible.

Using the OHM with data from 2003 shows that the model can also be applied with sufficient accuracy to scenes from a different year recorded at approximately the same time of the year, and not only while an *in situ* network is available. The advantage of using this approach with remotely sensed data in other cities or urban areas is therefore obvious, even if there is no energy balance network available for verification, although, of course, a best-case scenario would include such a network.

The OHM approach is the most promising, although at least two net radiation scenes (to enable calculation of ($\delta Q^* / \delta t$)) and a land use classification are necessary to enable modelling of the ground heat flux densities. The parameters a_1, a_2 and a_3 can be derived either from *in situ* measurements, as in this study, or from already published values (see Grimmond & Oke 1999). Using the OHM approach, depending on satellite overpass times and availability of the relevant parameters from *in situ* data measurements, it is also possible to compute the nighttime ground heat flux densities. Generally, the more accurate modelling of the rural sites can be attributed to their more homogeneous surfaces, as well as to the more accurate measurements attainable with heat flux plates when compared to the urban sites (Weber, 2006). Although the urban sites also yield reasonable results, it remains a difficult task to take into account all of the specific parameters of urban surfaces (e.g. urban anisotropy (Voogt & Oke, 1997).

Along with its high accuracy, these points give the OHM model a considerable advantage for further modelling of storage heat flux densities in both urban and rural environments. Nevertheless, as the results show, the complex surface parameters of urban surfaces cannot all be taken into account with this model.

8.4 Turbulent heat flux densities

As comparison with the results of different studies, which also struggle with the difficulties of assessing the heat flux densities, shows, the turbulent heat flux densities were modelled with reasonable accuracy. Although there was no comparable research conducted until now (as described most models model the daily course at a specific site) the spatial distribution of these values confirms the findings of the BUBBLE *in situ* datasets as well as the general theory, as described by Oke (1982, 1990), of climate modification by urban areas. This all underscores the necessity of a spatial approach using remotely sensed data, while illustrating that the common assumption that high surface temperature correlates directly with high air temperature is actually completely false. As has been shown, between rural and urban surfaces, the difference in Q_H is much smaller than it is in Q_E (except for forest areas), while the spatial distribution of the turbulent fluxes was confirmed by *in situ* data. The results also show that satellite data are accurate enough to be used for flux modelling not only of strictly homogeneous rural test sites, but also of heterogeneous urban surfaces.

8.5 General conclusions

The results of this study show the successful application of satellite derived high and medium resolution data in combination with *in situ* data, for the modelling of radiation and heat flux densities in the spatial domain for an urban area. Without the BUBBLE study's extensive *in situ* network, which was essential both for data validation and for the acquisition of certain input parameters, this work would not have been possible.

The results are accurate enough to show the distribution of all the daytime radiation and energy flux densities in the spatial domain. It was also shown for the first time that the OHM model could be used accurately on satellite data for both urban and rural areas.

Even considering the different sources of error with satellite data processing and with *in situ* data, the results can be accepted as reasonably accurate; nevertheless there is always room for improvement, even if the datasets were validated with *in situ* data after each step.

The thesis also shows how, even in the absence of certain input parameters, the model can be applied to other datasets for the same research area from a different year (2003) and still yield fully acceptable results.

9. Outlook

The spatial resolution of the model here is approximately 30m, which is sufficient to distinguish between densely and lightly built-up industrial and residential areas of the city, as well as to determine the city's radiation and heat flux density distribution, with enough accuracy to be useful for city planners and city authorities. Above all, these results illustrate the usefulness of a satellite with higher temporal and spatial resolution in the thermal infrared wavelengths, and should encourage city planners to consider the thermal properties of cities to improve urban environments. This will enable even more consistent and accurate high resolution modelling of radiation and heat flux densities in the spatial domain of urban climatology. It also clarifies what is possible using satellite remote sensing data in urban climatology, although there is an obvious need for higher resolution thermal infrared data, along with, as mentioned by Piringer et al. (2002), further use of remote sensing data for the modelling of heat flux densities. As the preliminary results in this thesis show, high resolution datasets will also pose problems (e.g. urban anisotropy, temporal data coverage) for further study. As shown, ASTER data are substitute very well for LANDSAT ETM+ data and are recommended for further use.

The model described in this work is an approach that should be tested on other cities where *in situ* data are available. Once validated in different regions, it can be used for the modelling of radiation and heat flux densities on a wide range of cities where no or few *in situ* data are available. In a growing number of urbanized areas around the world, especially in developing countries, almost no *in situ* data exist, but remote sensing data, is constantly being recorded. If successful, this model will offer an opportunity to use that data. As shown, however, very high resolution data from spaceborne and airborne sensors present their own difficulties: further research and far more complicated implementations of existing technology will be necessary to measure and interpret the effects of urban surfaces on meteorological parameters and the radiation and energy fluxes balances.

Remotely sensed data are extremely valuable to the understanding and analysis of urban climates, especially in larger cities. With such data already available, the next challenge is to use it to design cities that offer more comfortable living spaces, particularly in developing countries with rapidly-expanding urban areas.

Bibliography

Aida M. (1982). Urban albedo as a function of the urban structure- A model experiment. *Boundary-Layer Meteorology*, **23**, 405-413

Anderson M.C., Norman, J.M., Diak, G. R., Kustas, W.P., Mecikalski, J.R. (1997). A Two-source time- integrated model for estimating surface fluxes using thermal infrared remote sensing. *Remote Sensing of Environment,* **60**, 195-216

Arnfield, A. J. (2003). Two decades of urban climate research: a review of turbulence, exchanges of energy and water and the urban heat island. *International Journal of Climatology,* **23**, 1- 26

Baastiansen, W.G.M, Meneti, M., Feddes, R.A., Holtslag, A.A.M. (1997). A remote sensing surface energy balance algorithm for land (SEBAL). Part 1: Formulation. *SC-DLO, Wageningen NL*

Becker, F. & Li, Z.-L. (1990). Toward a local split window method over land surfaces. *International Journal of Remote Sensing*, **11**, 369-393

Boegh, E., Scheide, K., Soegaard, H. (2000). Estimating transpiration rates in a Danish agricultural area using Landsat thermal mapper data. *Physics and Chemistry of Earth,* **25 (7-8)**, 685- 689

Capparini, F., Castelli, F., Enthekabi, D. (2003). Mapping of land-atmosphere heat fluxes and surface parameters with remote sensing data. *Boundary Layer Meteorology*, **107**, 605-633

Chen, J.M., Rich, P.M., Gower, S.T., Norman, J.M., Plummer, S. (1997). Leaf area index of boreal forests: Theory, techniques and measurements, *Journal of Geophysical Research*, **102**, 429-443

Christen, A., Bernhofer, C., Parlow, E., Rotach, M.W., Vogt, R. (2003). Partitioning of turbulent fluxes over different urban surfaces. *Proceedings of the 5th International Conference on Urban Climatology (ICUC 5), Lodz, Poland*, 285-288

Christen, A. & Vogt, R. (2004). Energy and radiation balance of a Central European City. *International Journal of Climatology,* **24**, 1395-1421

Christen, A. & Vogt, R. (2005). Quality control and corrections of the radiation measurements at the BUBBLE surface sites. *Stratus Technical Report / Arbeitsbericht 003, 18pp, Institute of Meteorology, Climatology and Remote Sensing*, *University of Basel*

Christen A. (2005). Atmospheric turbulence and surface energy exchange in urban environments. *Ph.D. Thesis, Institute of Meteorology, Climatology and Remote Sensing, University of Basel, Switzerland,* Stratus, **No. 11**

Chrysoulakis, N. (2003). Estimation of the all-wave urban surface radiation balance by use of ASTER multispectral imagery and *in situ* spatial data., *Journal of Geophysical Research*, **108 (D18)**, 4582

Coll, C., Caselles, V., Galve, J.M., Valor, E., Niclos, R., Sanchez, J.M., Rivas, R. (2005). Ground measurement for the validation of land surface temperatures derived from AATSR and MODIS data, *Remote Sensing of Environment*, **97**, 288-300

Czajkowski, K.P., Godward, S.N. and Ouaidrari, H. (1998). Impact of AVHRR filter functions on surface temperature estimation from the Split Window approach. *International Journal of Remote Sensing*, **19**, 2007-2012

Dash, P., Göttsche, F.-M., Olesen, F.-S., Fischer, H. (2002). Land surface temperature and emissivity estimation from passive sensor data: theory and practice –current trends. *International Journal of Remote Sensing,* **23** , 2563-2594

Doerksen, G.N. (2004). Parametrization of net radiation in urban and suburban environments. *M.Sc.-thesis, University of British Columbia, Vancouver, Canada*

Dousset, B. & Gourmelon, F. (2003). Satellite multi-sensor analysis of urban surface temperatures and landcover. *ISPRS Journal of Photogrammetry & Remote Sensing*, **58**, 43-54

Eymard, L. & Tacomet, O. (1995). The methods for inferring surface fluxes from satellite data and their use for atmosphere model validation. *International Journal of Remote Sensing*, **16**, 1907-1930

French N.A., Jacob, F., Anderson, M.C., Kustas, W.P., Timmermans, W., Gieske, A., Su, Z., Su, H., McCabe, M.F., Li. F., Prueger, J., Brunsell, N., (2005). Surface energy fluxes with the Advanced Spaceborne Thermal Emission and Reflection Radiometer (ASTER) at the Iowa 2002 SMACEX site (USA), *Remote Sensing of Environment*, **99**, 55 - 65

Gallo, K. P., McNab, A.L., Karl, T.R., Brown, J.F., Hood, J.J., Tarpley, J.D. (1993). The Use of NOAA AVHRR data for assessment of the urban heat island effect. *Journal of Applied Meteorology*, **32**, 899-908

Gallo, K.P. & Owen, T.W. (1999). Satellite-based adjustments for the urban heat island temperature bias. *Journal of Applied Meteorology*, **38**, 806-813.

Gallo, K.P., Ji, L., Reed, B., Eidenshink, J., Dwyer, J. (2005). Multi-platfrom comparisons of MODIS and AVHRR normalized difference vegetation data. *Remote Sensing of Environment,* **99**, 221-231

Gao, W., Coulter, R.L., Lesht, B.M., Qiu, J., Wesely, M.L. (1998). Estimating clear-sky regional surface fluxes in the southern Great Plains atmospheric radiation measurement site with ground measurements and satellite observations. *Journal of Applied Meteorology,* **37**, 5-22

Gieske, A. S.; Wubett, M. T; Timmermans, W. J; Parodi, G. N.; Wolski, P. & Arneth, A. (2003). Temperature-emissivity separation with ASTER and LANDSAT 7; validation on the fringe of the Okavango Delta, Botswana. *Proceedings of the SPIE conference, 10th International remote sensing meeting, 8-12. September 2003, Barcelona, Spain: 10*

Gillespie, A. R., Rokugawa, S., Matsunaga, T., Cothern, J. S., Hook, S., Kahle, A. B. (1998). A Temperature and emissivity separation algorithm for Advanced Spaceborne Thermal Emission and Reflection Radiometer (ASTER) images. *IEEE Transactions on Geoscience and Remote Sensing*, **36**, 1113–1126.

Gleason, A.C.R., Prince, S.D., Goetz, S.J., Small, J. (2002). Effects of orbital drift on land surface temperature measured by AVHRR thermal sensors. *Remote Sensing of Environment*, **79**, 147-165

Goetz, S.J. (1997). Multi-sensor analysis of NDVI, surface temperature and biophysical variables at a mixed grassland site. *International Journal of Remote Sensing,* **18**, 71-94

Goodrum, G., Kidwell, K.B. and Winston, W. (1998). NOAA KLM user's guide; Tech. rep., *National Environmental Satellite Data and Information Services (NESDIS)*

Grimmond, C.S.B. & Oke, T.R. (1991). An objective urban heat-storage model and its comparison with other schemes. *Atmospheric Environment, Part B: Urban Atmosphere,* **25**, 311-326

Grimmond, C.B.S. & Oke, T. (1999). Heat storage in urban areas: Local-scale observations and evaluation of a simple model. *Journal of Applied Meteorology*, **38**, 922 - 940

Grimmond, C.B.S. & Oke, T.R. (2002). Turbulent heat fluxes in urban areas: Observations and a Local-Scale Urban Meteorological Pararmetrization Scheme (LUMPS). *Journal of Applied Meteorology,* **41,** 792-810.

Gutman, G.G. (1999). On the monitoring of land surface temperature with the NOAA/AVHRR: removing the effect of satellite orbit drift. *International Journal of Remote Sensing,* **20**, 3407-3413.

Han, K.-S., Viau, A.A., Anctil, F. (2004). Analysis of GOES and NOAA derived land surface temperatures estimated over a boreal forest. *International Journal of Remote Sensing*, **25 (21)**, 4761-4780

Harman, I.N., Best, M.J., Belcher, S.E. (2004). Radiative exchange in an urban canyon. *Boundary-Layer Meteorology,* **110,** 301-316

Huete, A.R. (1988). A Soil-Adjusted Vegetation Index (SAVI), *Remote Sensing of Environment*, **25**, 295-309

Jacob, F., Petitcolin, F., Schmugge, T., Vermote, E., French, A., Ogawa, A. (2004). Comparison of land surface emissivity and radiometric temperature derived from MODIS and ASTER sensors. *Remote Sensing of Environment*, **90**, 137-152

Jiang, L. & Islam, S. (2003). An intercomparison of regional latent heat flux estimation using remote sensing data. *International Journal of Remote Sensing,* **24**, 2221-2236

Jimenez-Munoz, J.C. & Sobrino, J. A. (2006). Errror on the land surface temperature retrieved from thermal infrared single channel remote sensing data. *International Journal of Remote Sensing*, **27**, 999-1014

Jin, M. & Treadon, R.E. (2003). Correcting the orbit drift effect on AVHRR land surface skin temperature measurements. *International Journal of Remote Sensing,* **24**, 4543-4558.

Kato, S. & Yamaguchi Y. (2005). Analysis of urban heat-island effect using ASTER and ETM+ data: Separation of anthropogenic heat discharge and natural heat radiation from sensible heat flux. *Remote Sensing of Environment*, **99,** 44-54

Kerenyi, J. & Putsay, M. (2000). Investigations of land surface temperature algorithms using NOAA-AVHRR images. *Advanced Space Research*, **26 (7)**, 1077-1080

Key, J. (2002). The Cloud and Surface Parameter Retrieval (CASPR) System for Polar AVHRR User's Guide. *Cooperative Institute for Meteorological Satellite Studies*, University of Wisconsin

Kim, H.H. (1992). Urban heat island. *International Journal of Remote Sensing*, **13**, 2319-2336

Kondo, A., Ueno, M., Kaga, A. (2001). The influence of urban canopy configuration on urban albedo, *Boundary-Layer Meteorology,* **100**, 225-242

Kustas, W.P & Daughtry C.S.T (1990). Estimation of the soil heat flux/net radiation ratio from spectral data. *Agricultural and Forest Meteorology*, **49**, 205 – 223

Kustas, W.P., Norman, J.M., Anderson, M.C., French, A.N. (2003). Estimating subpixel surface temperatures and energy fluxes from the vegetation index-radiometric temperature relationship. *Remote Sensing of Environment*, **85**, 429-440

Kustas, W.P., Li, F., Jackson, T.J., Prueger, J.H., MacPherson J.I., Wolde, M. (2004). Effects of remote sensing pixel resolution on modelled energy flux variability of croplands in Iowa. *Remote Sensing of Environment*, **92**, 535-547

Landsberg, H.E. (1981). The Urban Climate. *International Geophysical Series,* **28**, New York

Legg, C. (1995). Remote sensing and geographic information systems. *Wiley, Chichester*

Lemonsu, A., Grimmond, C.S.B., Masson, V. (2004). Modelling the surface energy balance of the core of an old Mediterranean City: Marseille, *Journal of Applied Meteorology*, **43**, 312-327

Li, F., Jackson, T.J., Kustas, W.P., Schmugge, T.J., French, A.N., Cosh, M.H., Bindlish, R. (2004). Deriving land surface temperature from LANDSAT 5 and 7 during SMEX02/SMACEX. *Remote Sensing of Environment*, **92**, 521-534

Liang, S. (2001). Narrowband to broadband conversions of land surface albedo I: Algorithms. *Remote Sensing of Environment*, **76**, 213-238

Liang, S. (2004). Quantitative remote sensing of land surfaces. *Wiley, New Jersey*

Liang, S., Shuey, C.J., Russ, A.L., Fang, H., Chen, M., Walthall, C.L., Daughtry, C.S.T., Hunt, R. (2003). Narrowband to broadband conversions of land surface albedo: II Validation. *Remote Sensing of Environment*, **84**, 25-41

Lillesand T.M. & Kiefer R.W. (1994). Remote sensing and image interpretation, *Wiley & Sons, New York*

Liu, H., & Foken, T., (2001). A modified Bowen-Ratio method to determine sensible and latent heat fluxes, *Meteorologische Zeitschrift*, **10**, 71-80

Lo, C.P, & Faber, B.J. (1997). Integration of Landsat Thematic Mapper and census data for quality of life assessment. *Remote Sensing of Environment,* **62**, 143-157

Ma, Y. (2003). Remote sensing parametrization of regional net radiation over heterogneous land surface of Tibetan Plateau and arid area. *International Journal of Remote Sensing,* **24,** 3137-2148

Ma, Y., Su. Z., Koike, T., Yao. T., Ishikawa, H., Ueno, K., Menenti M., (2003). On measuring and remote sensing surface energy partitioning on the Tibetan Plateau –from GAME/Tibet to CAMP/Tibet. *Physics and Chemistry of the Earth*, **28**, 63-74

Mather, P.M. (1999). Computer processing of remotely sensed images. *John Wiley & Sons, Chichester*

Mestayer, P.G., Durand, P., Augustin, P, Bastin, S., Bonnefond, J.-M., Bénech, B., Campistron, B., Copalle, A., Delbarre, H., Dousset, B., Drobinski, P., Druilhet, A., Fréjafon, E., Grimmond, C.S.B., Groleau, D., Irvine, M., Kergormard, C., Kermadi, S., Laguarde, J.-P., Lemonsu, A., Lohou, F., Long, N., Masson, V., Moppert, C, Noilhan, J., Offerle, B., Oke, T.R., Pigeon, G., Puygrenier, V., Roberts, S., Rosant, J.-M., Said, F., Salmond, J., Talbaut, M., Voggt, J. (2005). The urban boundary-layer field campaign in Marseille (UBL/CLU-ESCOMPTE): Set-up and first results. *Boundary-Layer Meteorology*, **114**, 315-365

Moore, C.J., (1986). Frequency response corrections for eddy correlation systems. *Boundary-Layer Meteorology*, **37**, 17-35

Munier, K. & Burger, H. (2001). Analysis of land use data and surface temperature derived from satellite data for the area of Berlin. In: Jürgens, C. (Ed.): *Remote Sensing of Urban Areas/ Fernerkundung in urbanen Räumen* (pp. 206-221) Regensburg: Regensburger Geographische Schriften, Heft **35**

Musa, M. (1998). Modellierung des Bodenwärmestromes über urbanen und ruralen Flächen im REKLIP-Untersuchungsgebiet mit Hilfe von LANDSAT-TM Daten. *Diploma thesis Institute of Meteorology, Climatology and Remote Sensing, University of Basel*, *Switzerland*

Nichol, J. E. (1998). Visualization of urban surface temperatures derived from satellite images. *International Journal of Remote Sensing*, **19**, 1639-1649

Nichol, J.E. & Wong, M.S. (2005). Modelling urban environmental quality in a tropical city. *Landscape and Urban Planning,* **73 (1)**, 49-58.

Nicodemus, F.E., Richmond, J.C., Hsia, J.J. (1977). Geometrical considerations and nomenclature for reflectance. *NBS Monograph 160, US Department of Commerce, National Bureau of Standards,* 52p

Norman, J.M., Kustas, W.P., Humes, K.S.(1995). Source approach for estimating soil and vegetation energy fluxes in observation of directional radiometric temperature. *Agriculture and Forest Meteorology*, **77**, 263-293

Oesch, D. (2005). Retrieval of lake surface water temperature from NOAA-AVHRR. *Ph.D. thesis, University of Berne, Switzerland*

Offerle, B., Grimond, C.S.B., Fortuniak, K., Klysik, K., Oke T.R. (2006). Temporal variations in heat fluxes over a central European city centre. *Theoretical and Applied Climatology*, **84 (1-3)**, 103-115

Ogawa, K.; Schmugge, T. J.; Jacob, F. & French, A. N. (2002). Estimation of broadband land surface emissivity from multispectral thermal infrared remote sensing. *Agronomie: Agriculture Environment*, **22(6)**: 695-696

Oke, T.R. (1982). The energetic basis of the urban heat island. *Quarterly Journal of the Royal Meteorological Society*, **108**, 1-24

Oke, T.R., (1990). Boundary Layer Climates (2nd edition). Taylor & Francis, London

Oke, T.R. & Cleugh, H.A. (1987). Urban heat storage derived as energy budget residuals. *Boundary Layer Meteorology*, **39**, 233 – 245

Oke, T.R., R.A. Spronken-Smith, E. Jauregui, C.S.B. Grimmond (1999). The energy balance of central Mexico City during the dry season. *Atmospheric Environment*, **33**, 3919 – 3930

Oncley, S.P., Foken, T., Vogt, R., Bernhofer, C., Kohsiek, W., Liu, H., Pitacco, A., Grantz, D., Riberio, L., Weidinger, T. (2002). The energy balance experiment EBEX-2000. *15th Symp. on Boundary Layer and Turbulence, Wageningen, NL, 15-19 July 2002*, Am. Meteorol. Soc., 1-4

Ouaidrari, O., Goward S., Czajkowski K., Sobrino J. and Vermote E. (2002). Land surface temperature estimation from AVHRR thermal infrared measurements. An assessment for the AVHRR Land Pathfnder II data set. *Remote Sensing of Environment*, **81**, 114-128

Parlow, E. (1996a). Net radiation in the REKLIP-area - A spatial approach using satellite data. (7.9.1995). In: Parlow E. (Ed.): *Progress in Environmental Research and Applications*, Balkema Rotterdam,

Parlow, E. (1996b). Correction of terrain controlled illumination effects in satellite data. In: Parlow E. (Ed.): Progress in Environmental Research and Applications, p. 139 – 145. Balkema Rotterdam.

Parlow, E. (1998). Analyse von Stadtklima mit Methoden der Fernerkundung. *Geographische Rundschau,* **9**, 89-93

Parlow, E. (2000). Remotely sensed heat fluxes of urban areas. In: *de Dear R.J., Kalma J.D., Oke T.R. and Auliciems A. (Eds.): Biometeorology and urban climatology at the turn of the millennium - Selected papers from the conference ICB-ICUC'99. WMO/TD No.* 1026, p. 523 - 528.

Parlow, E. (2003). The urban heat budget derived from satellite data. *Geographica Helvetica*, **2**, 99 – 111

Payan, V. & Royer, A. (2004). Analysis of Temperature Emissivity Separation (TES) algorithm applicability and sensitivity. *International Journal of Remote Sensing*, **25,** 15-37

Petitcolin, F. & Vermote, E. (2002). Land surface reflectance, emissivity and temperature from MODIS middle and thermal infrared data. *Remote Sensing of Environment*, **83**, 112-134

Pfändler, S. (2003). Strahlungsmessungen in einem Strassencanyon während BUBBLE. *Diploma Thesis, Institute for Meteorology, Climatology and Remote Sensing, University of Basel, Switzerland*

Philipona, R., Fröhlich, C., Betz, C. (1995). Characterization of pyrgeometers and the accuracy of atmospheric long-wave radiation measurements. *Applied Optics*, **34,** 1598-1605

Piringer, M., Grimmond C.B.S., Joffre, S. M., Mestayer, P., Middleton, D. R., Rotach, M. W., Baklanov, A., De Ridder, K., Ferreira, J., Guilloteau, E., Karpinen, A., Martilli, A., Masson, V., Tombrou M., (2002). Investigating the surface energy balance in urban areas- recent advances and future needs. *Water, Air, and Soil Pollution: Focus*, **2**, 1-16

Prata, A. & Platt, C. (1991). Land surface temperature measurements from the AVHRR. *Proceedings of the 5th AVHRR Data Users Conference, June 25-28, Tromsö, Norway, EUM P09*, 433-438.

Price, J.-C. (1980). The potential of remotely sensed thermal infrared data to infer surface soil moisture and evapotranspiration. *Water Resources Research*, **16 (4)**, 787-795

Price, J.-C. (1983). Estimating surface temperatures from satellite thermal infrared data –a simple formulation for the atmospheric effect. *Remote Sensing of Environment*, **13**, 353 - 361.

Price, J.-C. (1984). Land surface temperature measurements from the split window channels of the NOAA-7 AVHRR. *Journal of Geophysical Research*, **89**, 7231-7237.

Price, J.-C. (1991). Timing of NOAA afternoon passes. *International Journal of Remote Sensing,* **12**, 193-198.

Quattrochi D.A., & Ridd M.K. (1998). Analysis of vegetation within a semi-arid urban environment usig high spatial resolution airborne thermal infrared remote sensing data. *Atmospheric Environment*, **32 (1)**, 19-33

Rahman, H. & Dedieu, G. (1994). SMAC: a simplified method for the atmospheric correction of satellite measurements in the solar spectrum. *International Journal of Remote Sensing*, **15**, 123-143

Rao, C. & Chen, J. (1999). Revised post-launch calibration of the visible and near infrared channels of the Advanced Very High Resolution Radiometer (AVHRR) on the NOAA-14 spacecraft. *International Journal of Remote Sensing,* **20**, 3485-3491

Richards, J. A. & Jia, X. (1999). Remote sensing digital image analysis: an introduction. *Springer, Berlin*

Rigo, G. (2001). Multitemporale Analyse der Strahlungstemperartur der städtischen Wärmeinsel von Basel; *Diploma Thesis, Institute for Meteorology, Climatology and Remote Sensing, University of Basel, Switzerland*

Rigo. G. & Parlow, E. (200?) Modelling the ground heat flux in an urban area with remote sensing methods. *Theoretical and Applied Climatology (accepted)*

Rigo, G., Parlow, E. Oesch, D. (2006). Validation of observed thermal emission with *in situ* measurements over an urban surface. *Remote Sensing of Environment,***104**, 201-210

Rotach, M. W., Vogt, R., Bernhofer, C., Batchvarova, E., Christen, A., Clappier, A., Feddersen, B., Gryning, S-E., Martucci, G., Mayer, H., Mitev, V., Oke, T. R., Parlow, E., Richer, H., Roth, M., Roulet, Y-A., Ruffieux, D., Salmond, J. A., Schatzmann, M. and Voogt, J. A. (2005), BUBBLE- an urban boundary layer meteorology project. *Theoretical Applied Climatology ,***81**, 231- 261

Santanello, J.A. Jr., & Friedl, M.A. (2003). Diurnal covariation in soil heat flux and net radiation, *Journal of Applied Meteorology*, **42**, 851-862

Schotanus, P., Nieuwstadt F.T.M:, De Bruin H.A.R., (1983). Temperature measurement with a sonic anemometer and its application to heat and moisture fluxes. *Boundary-Layer Meteorology,* **26**, 81-93

Schott, J.R. & Volchok, W.J (1985). Thematic Mapper thermal infrared calibration. *Photogrammetric Engineering and Remote Sensing,* **52(9),** 1351-1357.

Schott, J.R., Barsi, J.A., Nordgren, B.L., Raqueno, N.G. and de Alwis, D. (2001). Calibration of LANDSAT Thermal Data and Application to Water Resource Studies. *Remote Sensing of Environment*, **78**, 108-117

Schwiebus A., & Berger, F.H. (2005). Sensivity studies and their application to infer surface energy fluxes: prospects within the passive remote sensing. *Physics and Chemistry of the Earth,* **30**, 187-193

Small, C. (2001), Estimation of urban vegetation abundance by spectral mixture analysis. *International Journal of Remote Sensing,* **22**, 1305-1334

Snyder, W.C., Wan. Z., Zhang, Y., Feng Y.-Z. (1998). Classification-based emissivity for land surface temperature measurement from space. *International Journal of Remote Sensing,* **19,** 2753-2774

Sobrino, J.A., Li, Z.-L., Stoll, M.P. (1993). Impact of the atmospheric transmittance and total water vapor content in the algorithms for estimating satellite sea surface temperatures. *IEEE Transactions on Geoscience and Remote Sensing*, **31**, 946-952.

Sobrino, J.A., Li, Z.-L., Stoll, M.P. (1994). Improvements in the split-window technique for land surface temperature determination. *IEEE Transactions on Geoscience and Remote Sensing*, **32**, 243-253.

Soux, A., Voogt, J.A., Oke T.R. (2004). A model to calculate what a remote sensor "sees" of an urban surface. *Boundary-Layer Meteorology*, **111**, 401-424

Stefanov, W.L. & Netzband, M. (2005). Assessment of ASTER land cover and MODIS NDVI data at multiple scales for ecological characterization of an arid urban center. *Remote Sensing of Environment,* **99**, 31-43

Steven, M.D., Malthus, T.J., Baret, F., Xu, H., Chopping, M.J. (2003). Intercalibration of vegetation indices from different sensor systems. *Remote Sensing of Environment,* **88**, 412-422

Stow, D.A. & Chen, D.M. (2002). Sensitivity of multitemporal NOAA AVHRR data of an urbanizing region to land- use / land-cover changes and misregistration. *Remote Sensing of Environment*, **80**, 297-307

Streutker, D.R. (2003). Satellite-measured growth of the urban heat island of Houston, Texas. *Remote Sensing of Environment*, **85**, 282-289

Tahnk, W.R. & Coakley, J.A. Jr. (2001). Updated calibration coefficients for NOAA-14 AVHRR channels 1 and 2. *International Journal of Remote Sensing*, **22**, 3053-3057

Tanner, B.D., Swiatek E., Greene J.P. (1993). Density fluctuations and use of the Krypton hygrometer in surface flux measurements. In: *Management of Irrigation and Drainage Systems*. *21-23 July, Park City, UT*, 945-952

Tucker, J.J. (1979). Red and photographic infrared linear combinations for monitoring vegetation. *Remote Sensing of Environment,* **8**, 127 -150.

Twine, T.E., Kustas, W.P., Norman J.M.., Cook, D.R., Houser, P.R., Meyers, T.P., Prueger, J.H., Starks, P.J., Wesely, M.L. (2000). Correcting eddy-covariance flux underestimates over a grassland, *Remote Sensing of Environment*, **103**, 279-300

Ulivieri, C., Castronuovo, C., Francioni, M., Cardillo, R. (1992). A split window algorithm for estimating land surface temperatures derived from satellites. *Comm. on Space Programs and Research (COSPAR), Washington, D. C.*

Valor, E. & Caselles, V. (1996). Mapping land surface emissivity from NDVI: Application to European, African, and South American areas. *Remote Sensing of Environment*, **57**, 167-184.

Van de Griend, A. & Owe, M. (1993). On the relationship between thermal emissivity and the normalized difference vegetation index for natural surfaces. *International Journal of Remote Sensing*, **14**, 1119-1131.

Vazquez, D.P., Reyes, F.J.O., Arboledas, L.A. (1997). A comparative study of algorithms for estimating land surface temperature from AVHRR data. *Remote Sensing of Environment*, **62**, 215-222.

Voogt, J.A. & Oke T.R. (1997). Complete surface temperatures. *Journal of Applied Meteorology*, **36**, 1117–1132.

Voogt, J.A. & Oke T.R. (1998). Effects of urban surface geometry on remotely-sensed surface temperature. *International Journal of Remote Sensing*, **19**, 895- 920

Voogt, J.A. & Oke, T. R. (2003). Thermal remote sensing of urban climates. *Remote Sensing of Environment,* **86**, 370-384

Wan, Z. & Li, Z.-L. (1997). A physics-based algorithm for retrieving land-surface emissivity and temperature from EOS/MODIS data. *IEEE Transactions on Geoscience and Remote Sensing*, **35 (4)**, 980-996

Wan, Z. (1999). MODIS Land-Surface Temperature Algorithm Theoretical Basis Document (LST ATBD). *Institute for Computational Earth System Science*, *University of California, Santa Barbara, USA*

Wan, Z., Zhang, Y., Zhang, Q. and Li, Z-L. (2002). Validation of the land-surface temperature products retrieved from Terra Moderate Resolution Imaging Spectroradiometer (MODIS) data, *Remote Sensing of Environment,* **83**, 163-180

Weber, S. (2006). Comparison of *in situ* measured ground heat fluxes within a heterogeneous urban ballast layer, *Theoretical and Applied Climatology*, **83 (1-4)**, 169-179

Webb, E., Pearman G., Leuning G., (1980). Correction of flux measurements for density effects due to heat and vapour transfer. *Quarterly Journal of the Royal Meteorological Society,* **106**, 85-100

Weng, Q., Lu, D., Schubring, J. (2004). Estimation of land surface temperature-vegetation abundance relationship for urban heat island studies. *Remote Sensing of Environment*, **89**, 467-483

Wilson, K., Goldstein, A., Falge, E., Aubinet, M., Baldocchi, D., Berbigier, P., Bernhofer, C., Ceulemans, R., Doman, H., Field,. C., Grelle, A., Ibrom, A., Law, B.E., Kowalsk, A., Meyers, T., Moncrieff, J., Monson, R., Oechel, W., Tenhumen, J., Valentini, R., Verma, S., (2002). Energy balance closure at FLUXNET sites. *Agriculture and Forest Meteorology*, **113**, 223-243.

Wilson, J.S., Clay, M., Martin, E., Stuckey, D., Vedder-Risch K. (2003). Evaluating environmental influences of zoning in urban ecosystems with remote sensing. *Remote Sensing of Environment,* **86**, 303-321

Wu, A., Li, Z. and Cihlar, J. (1995). Effects of land cover type and greenness on advanced very high resolution radiometer bidirectional reflectances: analysis and removal. *Journal of Geophysical Research*, **100**, 9179-9192.

Zha, Y., Gao, J., Ni, S. (2003). Use of normalized difference built-up index in automatically mapping urban areas from TM imagery. *International Journal of Remote Sensing*, **24 (3)**, 583-594

Zhan, X., Kustas, W.P., Humes, K.S. (1996). An intercomparison on models of sensible heat flux over partial canopy surfaces with remotely sensed surface temperature. *Remote Sensing of Environment*, **58**, 242-256

Zhou, L; Dickinson, R. E.; Ogawa, K. Tian, Y.; Jin, M; Schmugge, T & Tsvetsinskaya, E.(2003). Relations between albedo and emissivities from MODIS and ASTER data over North African Desert. *Geophysical Research Letters*, **30 (20)**, 2026-2030

A. Appendix

a) In situ sites

Sperrstrasse (U1)

The main urban site, with an 33m tower in an urban canyon (Sperrstrasse), which is characterized by a typical European urban surface with residential row houses 4-5 storeys high, enclosing large inner courtyards. The roof shape is approximately 50% flat and 50% pitched.

The tower was set up in October 2001 and measurements were carried out from November 1, 2002 to July 15, 2002.

Fig. A.1: The street canyon from above the Sperrstrasse site (U1). The orientation of the canyon is along 67° ENE = 247° WSW. This photo shows the view from the overpass of the large "Messe Basel"-building east of the site. Photographed towards WSW, 8.7.2002.

Spalenring (U2) / Klingelbergstrasse (after June 2003)

The second urban site, with a tower mounted on the roof of the building, is located in an area with building structures similar to those of U1. The site is located beside a tree-lined avenue (Spalenring) with high traffic intensity. The roof mixture of is 70% pitched and 30% flat. The measurements are available from 1992 until August 20, 2002, while the site also housed the Institute of Meteorology, Climatology and Remote Sensing of the University of Basel.

After September 1, 2002 the tower was moved to the Institute's new location in Klingelbergstrasse, where it is currently maintained as the urban reference site. The new site is also located beneath an avenue with high traffic intensity but without trees along the pavement.

Fig. A.2: The ultrasonic anemometer profile of the Spalenring site (U2) consisted of six METEK USA-1 that were operated from tower top (38m) down into the street canyon to the west of the tower. There are alley trees inside the canyon (24.9.2001) (official BUBBLE photo).

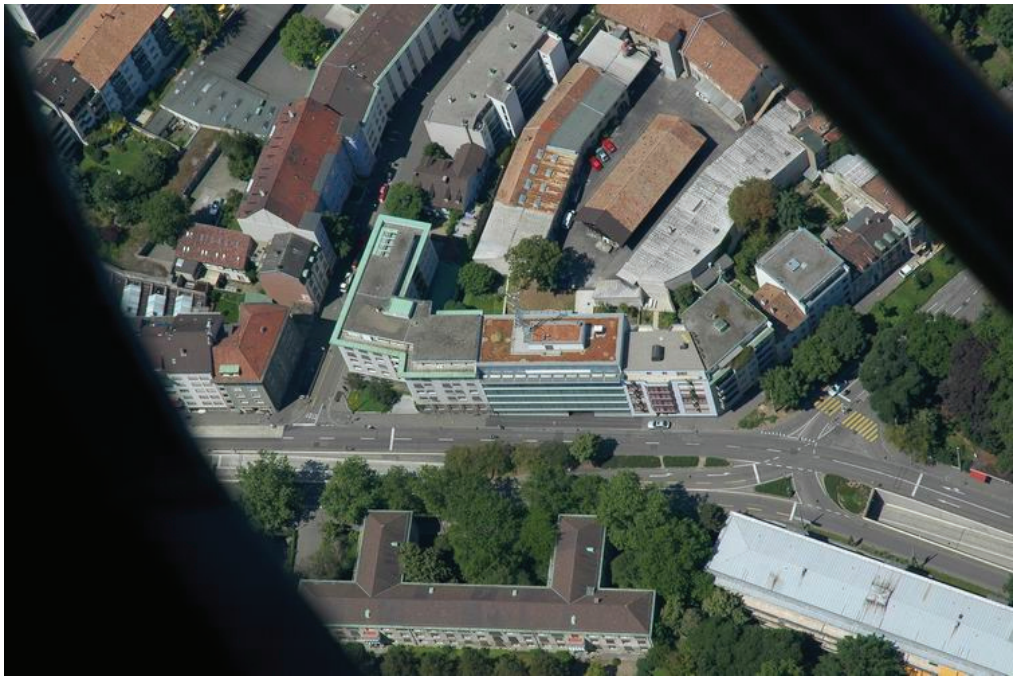

Fig. A.3: The Klingelbergstrasse site with the measurement tower located on the roof of the new institute. July 16, 2004 (Photo by R. Vogt).

Messe (U3)

This is the third urban site, with a more experimental character, situated on the roof of a parking garage measuring 170m x 80m. The area is characterized by large building blocks. The roof is also used for parking but was closed during the period of measurements. This site provides very local information from this 100% impervious surface. This site was operated only from June 24, 2002 to July 10, 2002.

Fig. A.4: Aerial view of the concrete roof from West at the Messe site (U3) (Photo by Roland Vogt, 16.7.2004)

Allschwil (S1)

This is a suburban site. Located in a vegetated backyard, it gives information from a less densely built up area. The area consists of 2-3 storey single and semi-detached houses constructed at the beginning of the last century. The backyards are vegetated with trees and shrubs. The site was operated from June 4, 2002 to July 12, 2002.

Fig. A.5: Photo of the Allschwil site (S1) (24.06.2002).

Grenzach (R1)

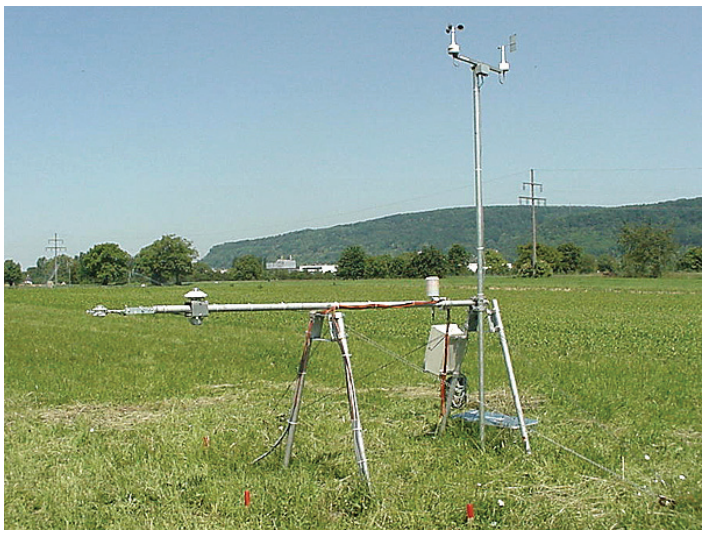

The first rural site is situated on the German side of the River Rhine, about 5km east of the city. The main land use is agricultural with non-irrigated grassland and crops, with building complexes 200m to the East and the River Rhine 300m to the south. The site was operated from April 24, 2002 to July 12, 2002.

Fig. A.6: The surface station at the Grenzach site (R1) supports radiation instrumentation, standard meteo and soil heat flux / soil temperatures. 31.05.2002

Village Neuf (R2)

The second rural site in France situated in an agricultural field located about 4km north of the city. The station was placed over flat and homogeneous non-irrigated agricultural land (bare soil). The site was set up and operated from May, 6 2002 to July 12, 2002.

Fig. A.7: The Village-Neuf sites (R2) surroundings in Western direction (14.05.2002).

Lange Erlen (R3)

This is the rural reference site with the longest record available. Situated in Switzerland in the valley of the River Wiese, to the northeast of the city, the tower is mainly surrounded by non-irrigated grassland and further away by built-up areas. The tower was set up in 1991 as a rural reference site and is still used in this capacity.

Fig. A.8: The Lange-Erlen (R3) site is operated since 1991.

Gempen (R4)

Not on the map in Fig. 2.2 but nevertheless one of the Institute's long-term reference sites , this is situated on a low hill in an agricultural environment outside the city, at an altitude of approximately 700m a.s.l.. The site was also set up in 1991 and is still maintained and used as a rural reference site.

Fig.A.9: The Gempen site (R4)

b) Satellite Images

Tab. A.1 : List of all used satellite images

Satellite	Date	Overpass Time (UTC)	LST	Q*	ΔQ_S	Turbulent fluxes	Remarks
Data during the BUBBLE IOP							
NOAA- AVHRR 14	25.06.2002	6:08	X				
NOAA- AVHRR 14	27.06.2002	5:43	X				
NOAA- AVHRR 14	07.07.2002	16.49	X				
NOAA- AVHRR 14	08.07.2002	5.07	X				
NOAA- AVHRR 14	08.07.2002	6:47	X	X	X		
NOAA- AVHRR 15	25.06.2002	7:23	X	X	X		
NOAA- AVHRR 15	07.07.2002	7.44	X				
NOAA- AVHRR 15	07.07.2002	17.28	X				
NOAA- AVHRR 15	08.07.2002	7:21	X	X			
NOAA- AVHRR 16	25.06.2002	12:45	X	X	X		
NOAA- AVHRR 16	26.06.2002	1:10	X				
NOAA- AVHRR 16	26.06.2002	12:34	X	X	X		
NOAA- AVHRR 16	27.06.2002	2:33	X	X			
NOAA- AVHRR 16	07.07.2002	12:13	X				Partly clouded
NOAA- AVHRR 16	08.07.2002	2:13	X	X	X		
NOAA- AVHRR 16	08.07.2002	11:10	X	X	X	X	
MODIS (TERRA)	17.06.2002	10:50	X	X			
MODIS (TERRA)	17.06.2002	22:00	X				
MODIS (TERRA)	18.06.2002	11:40	X	X			
MODIS (TERRA)	23.06.2002	10:40	X				
MODIS (TERRA)	25.06.2002	11:40	X	X	X		
MODIS (TERRA)	25.06.2002	22:10	X				
MODIS (TERRA)	26.06.2002	10:40	X	X	X		
MODIS (TERRA)	26.06.2002	21:50	X	X	X		
MODIS (TERRA)	30.06.2002	21:30	X				
MODIS (TERRA)	05.07.2002	10:40	X	X			
MODIS (TERRA)	07.07.2002	21:40	X				
MODIS (TERRA)	08.07.2002	11:10	X	X	X	X	
MODIS (TERRA)	08.07.2002	22:10	X	X	X	X	
LANDSAT ETM+	08.07.2002	10:10	X	X	X	X	
DATA outside of the BUBBLE-IOP							
NOAA- AVHRR 12	13.10.2003	4:11	X				
NOAA- AVHRR 12	15.10.2003	5:02	X				
NOAA- AVHRR 12	16.10.2003	4:37	X				
NOAA- AVHRR 12	16.10.2003	16:20	X				
NOAA- AVHRR 14	04.08.2003	18:21	X				
NOAA- AVHRR 14	05.08.2003	18:08	X				
NOAA- AVHRR 14	06.08.2003	17:55	X				
NOAA- AVHRR 14	13.10.2003	18:40	X				

NOAA- AVHRR 14	14.10.2003	6:44	X				Partly clouded
NOAA- AVHRR 14	15:10.2003	18:14	X				
NOAA- AVHRR 14	16.10.2003	18:01	X				
NOAA- AVHRR 15	04.08.2003	17:29	X				
NOAA- AVHRR 15	05.08.2003	7:21	X	X	X		
NOAA- AVHRR 15	05.08.2003	17:06	X				
NOAA- AVHRR 15	06.08.2003	16:43	X				Partly clouded
NOAA- AVHRR 15	13.10.2003	16:43	X				
NOAA- AVHRR 15	15.10.2003	6:11	X				
NOAA- AVHRR 15	15.10.2003	17:37	X				
NOAA- AVHRR 15	16.10.2003	17:12	X				
NOAA- AVHRR 16	15.10.2003	1:20	X				
NOAA- AVHRR 16	16.10.2003	2:50	X				
NOAA- AVHRR 17	04.08.2003	21:02	X	X			
NOAA- AVHRR 17	05.08.2003	20:40	X	X	X		
NOAA- AVHRR 17	06.08.2003	20:17	X	X			
NOAA- AVHRR 17	15.10.2003	20.35	X				
NOAA- AVHRR 17	16.10.2003	20:13	X				Partly clouded
MODIS (TERRA)	05.08.2003	11:00	X	X	X		
MODIS (TERRA)	05.08.2003	22:20	X				
MODIS (TERRA)	15.10.2003	11:10	X				
MODIS (TERRA)	15.10.2003	22:20	X				
MODIS (TERRA)	16.10.2003	21:25	X				
MODIS (TERRA)	17.10.2003	11:00	X				
MODIS (AQUA)	05.08.2003	12:40	X	X	X		
MODIS (AQUA)	05.08.2003	1:30	X				
MODIS (AQUA)	15.10.2003	12:50	X				
MODIS (AQUA)	15.10.2003	1:40	X				
MODIS (AQUA)	16.10.2003	2:20	X				
MODIS (AQUA)	17.10.2003	12:40	X				
MODIS (AQUA)	17.10.2003	2:20	X				
LANDSAT ETM+	12.06.2001	10:10					Used for LUC
ASTER	02.06.2000	10:55	X				
ASTER	12.06.2001	10:42	X				Used for LUC
ASTER	05.08.2003	10:33	X	X	X	X	
ASTER	15.10.2003	10:39	X				
ASTER	19.05.2004	10:34	X				
ASTER	29.05.2005	10:39	X				
QUICKBIRD	04.02.2002	10:31		X			No thermal-IR channel

c) Definitions of the statistics used

$$\frac{1}{n}\sum_{i=1}^{n}\left|P_i - O_i\right|$$ Mean absolute difference (MAD)

$$\frac{100}{n}\sum_{i=1}^{n}\frac{\left|P_i - O_i\right|}{\overline{O}}$$ Mean absolute percent difference (MAPD)

$$\left[\frac{1}{n}\sum_{i=1}^{n}\left(P_i - O_i\right)^2\right]^{1/2}$$ Root mean square error (RMSE)

where O is the observed or measured variable and P the predicted or modelled variable and n the number of measurements.